

**UNIVERSITÀ DEGLI STUDI DI NAPOLI
“FEDERICO II”**



**Scuola Politecnica e delle Scienze di Base
Area Didattica di Scienze Matematiche Fisiche e Naturali**

Dipartimento di Fisica “Ettore Pancini”

Laurea Magistrale in Fisica

**Coherence and control fidelity benchmarking of a multi-qubit
superconducting quantum processor**

Relatori:

Prof. Francesco Tafuri
Dott. Davide Massarotti
Dott.ssa Halima Giovanna Ahmad

Candidato:

Alessandro Sarno
Matr. N°94000742

Anno Accademico 2023/2024

Contents

Introduction	2
1 Superconducting Qubits	4
1.1 Introductory notes on qubits	4
1.2 Superconductivity and Josephson effect	5
1.3 From CPB to Transmon	7
1.4 Control and Readout in Transmons	10
1.4.1 Flux tunability	10
1.4.2 Quantum non-demolition readout	11
1.4.3 Qubit drive	12
1.5 Couplings between superconducting qubit	13
2 Coherence and Fidelity benchmarking	15
2.1 Impact of noise in qubits	15
2.1.1 Longitudinal relaxation	15
2.1.2 Pure dephasing	16
2.1.3 Transverse relaxation	17
2.2 Universal Quantum Computing	18
2.2.1 Single-qubit gates	18
2.2.2 Two-qubit gates	20
2.3 Fidelity and Randomized Benchmarking	24
3 Experimental setup and protocols	28
3.1 Quantum Processing Unit (QPU)	28
3.2 The dilution refrigerator	31
3.3 Cryogenic electronics	32
3.4 Room temperature electronics and acquisition software framework	35
3.5 Single-qubit and resonator characterization	38
3.6 Control pulses optimization and hardware implementation	39
3.7 Detecting syndromes for control optimization	43
3.8 Coherence times	47
3.9 Randomized Benchmarking	48
4 Final results and discussion	50
4.1 Single-qubit characterization of qubit B4: a case study	50
4.2 Qubits parameters	61
4.3 Coherence times	64
4.4 Single-qubit Gate Fidelity	65
4.5 Towards two-qubits characterization	68
Conclusions	70
Appendix A: Derivation of Fidelity-Coherence dependence	72
Appendix B: Derivation of fitting function in Randomized Benchmarking protocol	74

Introduction

Quantum Utility is the ultimate goal of modern quantum research: it consists in successfully building high-fidelity and large-scale quantum processors capable of running quantum algorithms that outperform classical computers in terms of computational power [1][2][3]. Quantum algorithms can be applied in many fields, including cryptography [4], quantum many-body and large molecules systems simulations [5][6]. One of the most advanced quantum computers is based on solid state systems and, in particular, on superconducting *qubits* which are able to encode and process the quantum information [7]. The building blocks of these devices are the tunnel Josephson junctions [8], which allow to artificially implement an atom-like system. Companies like Google [10], IBM [11], Rigetti [12] are currently laying the foundation for the near future quantum computing and communication in superconducting quantum platforms, tackling two fundamental roadmaps: increasing the number of qubits in quantum processors, while enhancing the coherence times and fidelity of superconducting qubits. Although fundamental milestones have been reached, e.g. Quantum Advantage and Utility in platforms from 50 to 1000 of superconducting qubits [10][11], today's platforms are still strongly affected by noise, resulting in deleterious effects on the information processing. We are still not in the Fault-tolerant Quantum Computing era, but in the so called NISQ (Noise Intermediate-Scale Quantum) era [13]. The more the Quantum Processing Unit (QPU) grows in size, the larger is the number of parameters that can influence qubit operative fidelity including, but not limited to:

- (i) the qubit-qubit connectivity, which plays a fundamental role in scalable quantum devices [14];
- (ii) the larger number of lines on the QPU, required to implement WRITE and READ operations, which may cause crosstalk, and unavoidably introduce interactions with the external environment, thus limiting the coherence;
- (iii) the largest number of degrees of freedom required to design simultaneous optimal and low-error readout and control signals.

This thesis work has been carried out in the context of the Quantum Computing Napoli (QCN) laboratory research activities, at the University of Napoli "Federico II". The main goal is to provide an open-source and scalable quantum computing node, where researchers can build and test their own quantum algorithms with reasonable advantage. The QCN infrastructure includes at the time of writing a 25-qubits processor. However, this system will be soon upgraded with a QPU including >40 qubits, thus increasing the computational capabilities of this unique superconducting quantum computing node. In this work we focus specifically on coherence properties and single-qubit gate fidelity evaluation in the 25-qubits QPU, in view of running quantum algorithms. Moreover, we provide a systematic study of the device's circuital parameters. The comparative approach presented here allows to understand the fundamental relation between circuit engineering and superconducting quantum technologies physics. The work is composed of four chapters.

In the first chapter we report the theoretical principles of the superconducting quantum platform. First, we briefly describe the superconductivity phenomena and the Josephson effect which are the basis of superconducting qubit devices. Then we focus on a particular qubit design exploited in this work, namely the *Transmon qubit*. This has been designed to offer special features such as: the possibility to tune in-situ the energy levels of isolated superconducting qubits through and external flux, to implement two-qubit gates operations by setting on resonance two or more qubits thanks to flux tunability, and to interface properly with the qubit for an efficient control and non-demolition readout of its quantum state [7][9].

In the second chapter we focus on the coherence properties of the superconducting qubit. We classify the several noise sources that may occur in these systems, specifically in terms of how they couple with the qubit system, and the deleterious effect they cause, primarily state relaxation and dephasing. Then we introduce the concept of Universal Quantum Computing, namely a set of single- and two-qubit quantum logic operations hardware agnostic, which allow for performing quantum algorithms.

Finally, the scientific community has introduced mathematical and physical methods to quantify the quality of the qubit performances by means of the state, readout and gate fidelity [15]. Here, we introduce the concept of *fidelity*, focusing on the gate fidelity and its evaluation through the Randomized Benchmarking method [16].

In the third chapter we describe the experimental setup exploited in this thesis work. We report the quantum processing unit design, i.e. the 25-qubit processor we have characterized. Then we report the hardware and software framework used to carry out the measurements, starting from the dilution refrigerator and the cryogenic electronics, and then the room temperature electronics with the acquisition software. In the last part we describe all the protocols necessary to characterize the qubit and to optimize the control hardware parameters. Finally, we describe the measurement protocols used to measure the coherence times and gate fidelity of qubits.

In the final chapter we collect, and discuss, the experimental results showing a detailed description of the protocols used to characterize and optimize the control pulses for one qubit, and then reporting all the measured parameters for each qubit we analyzed. We focus on coherence properties of the QPU, and then on the single qubit fidelity we reached after the optimization procedures. A detailed comparison of the coherence and fidelity performances of the QPU is finally reported. In the last paragraph, we give preliminary results on two-qubit characterization, in view of future implementation of quantum algorithms.

1 Superconducting Qubits

Since the first demonstration of emerging quantum phenomena in superconducting qubits [17], coherence times have been improved up to the millisecond [18], and it has been demonstrated high control and readout fidelity in quantum processing units with up to thousands of qubits [19]. Therefore, superconducting qubits have gained an increasing interest for practical Quantum Computing applications.

In Sec. 1.1, we will report on how the information is encoded in superconducting qubits, and the main concepts behind the building blocks of superconducting qubits, the Josephson junctions in Sec. 1.2. After that, we will focus on a specific circuit design exploited in this work, the transmon qubit, and its implementation in quantum processors from Sec. 1.3 to Sec. 1.5.

1.1 Introductory notes on qubits

Among the many platforms proposed to implement qubits, superconducting qubits are macroscopic in size and lithographically defined. They feature energy-level spectra governed by circuit element parameters, and thus remarkably configurable.

While in classical computing the information is encoded in two logical states 0 and 1, in quantum computing the information is encoded in terms of $\{|0\rangle, |1\rangle\}$, namely two energy states of a quantum two-level system, or "qubit".

In Bloch Sphere representation, the qubit state is figured as a Bloch vector: $|\psi\rangle = \alpha|0\rangle + \beta|1\rangle$, where α and β are coefficients such that $|\alpha|^2 + |\beta|^2 = 1$ [7]. According to a common convention, the north pole is the ground state $|0\rangle$, and the south pole is the excited state $|1\rangle$.

The z -axis, which connects the poles, is called longitudinal axis, since it represents the qubit quantization axis for the states $|0\rangle$ and $|1\rangle$ in the qubit eigenbasis. In turn, the $x - y$ plane is the transverse plane with transverse axes x and y . Alternatively, the unit Bloch vector (Fig. 1) can be represented in terms of the polar angle $0 \leq \theta \leq \pi$ and the azimuthal angle $0 \leq \varphi \leq 2\pi$:

$$|\psi\rangle = \alpha|0\rangle + \beta|1\rangle = \cos\frac{\theta}{2}|0\rangle + e^{i\varphi}\sin\frac{\theta}{2}|1\rangle. \quad (1)$$

If state $|1\rangle$ has a higher energy than state $|0\rangle$ in a stationary frame, the Bloch vector would precess around the z -axis at the qubit frequency $(E_1 - E_0)/\hbar$. For this reason it is common choice to represent the Bloch sphere in a reference frame, i.e. the rotating frame, where the x and y -axes also rotate around the z -axis at the qubit frequency, in which the Bloch vector appears stationary.

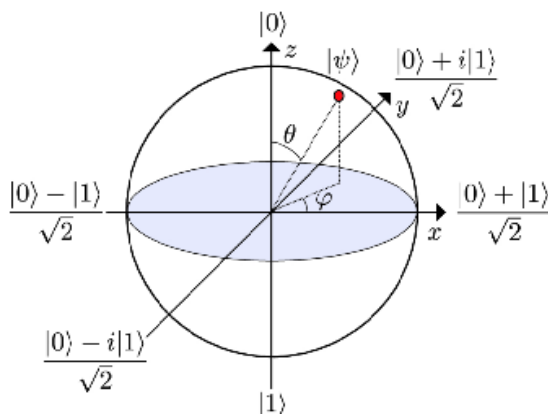


Figure 1: Unit vector on Bloch sphere.

The physical realization of quantum information processing needs to fulfill the Di Vincenzo criteria [20]:

- I.* A scalable physical system with well characterized qubits.
- II.* The ability to initialize the state of the qubits to a simple fiducial state.
- III.* Long relevant coherence times, much longer than the gate operation time.
- IV.* A “universal” set of quantum gates.
- V.* A qubit-specific measurement capability.

Superconducting qubits answer well to these criteria at the hardware level, since they rely on the circuitual engineering of macroscopic artificial atoms, known as **Josephson junctions**. Josephson junctions are the main circuitual elements in superconducting electronics, and exploit the intrinsic quantum nature of superconductors. In the following, we will provide the main concepts behind superconductivity and the Josephson effect, to better understand the operating principle of superconducting qubits.

1.2 Superconductivity and Josephson effect

The superconductivity is a thermodynamical state of matter that occurs in some materials below a critical temperature T_C . Example of superconducting material are Mercury, Aluminum, Cuprates and many other metals [21]. Peculiar properties of the superconductive state are [22]:

- Perfect conductivity, i.e the resistivity drops to zero leading to dissipationless current flow;
- Meissner effect: a superconductor manifests perfect diamagnetism expelling magnetic field up to a critical value H_c . For this reason, supercurrent flows only on the material surface within a region of λ thickness, called London penetration depth.

The consideration set out above apply to I-Type superconductors. Different behavior emerges in II-Type superconductors: after a first critical magnetic field value H_{c1} the material is still superconducting but it lets himself be pierced by external magnetic field lines up to a second critical value H_{c2} . This condition is called Abrikosov-Shubnikov phase.

Another interesting property, consequence of the two presented above, and useful for many application is:

- Flux quantization: in superconducting devices with a ring geometry the magnetic flux field is quantized, $\Phi = n\frac{h}{2e} = n\Phi_0$, where $\Phi_0 = \frac{h}{2e}$ is the flux quantum.

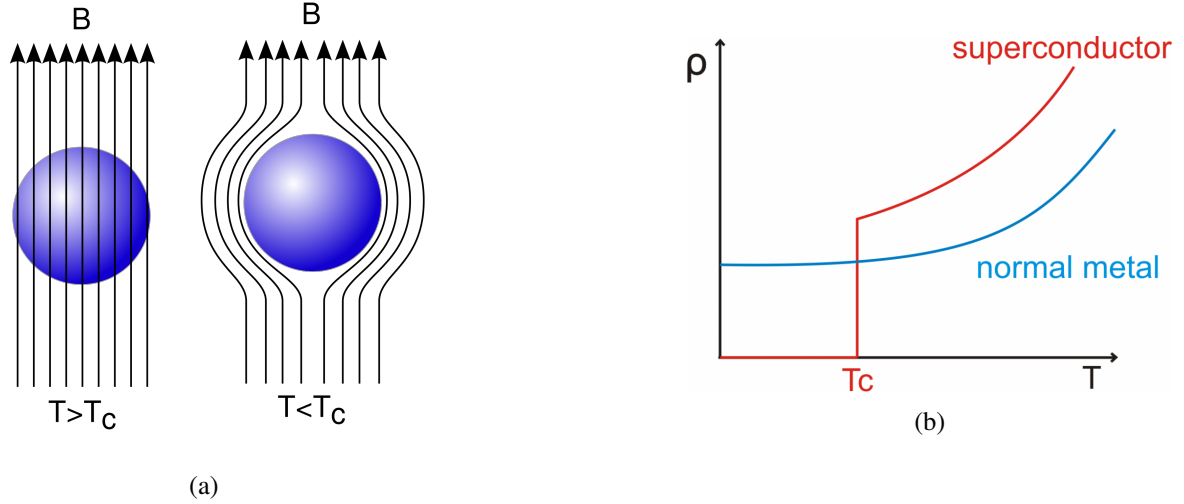


Figure 2: Superconductivity manifestations: perfect diamagnetism in (a) and zero resistivity in (b).

All the phenomenology of conventional superconductors can be fully explained by means of the Bardeen-Cooper-Schrieffer (BCS) theory of superconductivity [23]: below a critical temperature T_C , virtual electron-phonon interactions allow to couple two electrons with opposite spin and momentum into a Cooper pair [24]. Being Cooper-pairs boson-like particles, they can condensate in one macroscopic quantum wavefunction state, $\Psi(r, t) = \psi_0(r, t)e^{i\theta(r, t)}$, and hence coherently flow in the material without any dissipation. This is the key for building macroscopic artificial atoms. Indeed by coupling two superconducting materials through a non-superconducting barrier, it is possible to establish a coherent flow of Cooper pairs. This is called **Josephson effect**, and arises in what are known as Josephson junctions [8].

A Josephson Junction (JJ) is composed of an insulating material layer interposed between two superconductors (Fig. 3a). In case the insulator is thin enough, the wave functions of the two superconductors overlap, resulting in a transfer of Cooper pair from one island to the other as a function of their phase difference $\varphi = \varphi_1 - \varphi_2$. The two fundamental equations of the Josephson effect are:

$$I_s = I_c \sin \varphi, \quad (2)$$

$$\frac{\partial \varphi}{\partial t} = \frac{2e}{\hbar} V. \quad (3)$$

The first equation (Eq. (2)) describes the tunneling supercurrent I_s as a function of the phase difference φ , and states that this is limited by the critical current I_c , the maximum current that can flow through the junction before it switches to the resistive state with non-zero voltage. This depends on parameters like geometry and materials [7].

The second one (Eq. (3)) describes the time evolution of phase difference as a function of the voltage V across the junction with e and \hbar the electron charge and the reduced Planck constant, respectively. Moreover the JJ is characterized by a non linear $I - V$ characteristic shown in Fig. 3b.

The JJ acts as a non linear inductor [25] whose inductance is:

$$L_J = \frac{\hbar}{2eI_c \cos \varphi}. \quad (4)$$

This means that the potential energy of a JJ is also non-linear: by combining the first and second Josephson equations, we derive the phase dependence of the energy stored in the JJ as:

$$U_s = \int_0^t I_s(t)V(t)dt = \frac{\hbar}{2e}I_c \int_0^\varphi \sin \phi d\phi = \frac{\hbar I_c}{2e}(1 - \cos \varphi), \quad (5)$$

where $E_J = \frac{\hbar I_c}{2e} = \frac{I_c \Phi_0}{2\pi}$ is the Josephson energy.

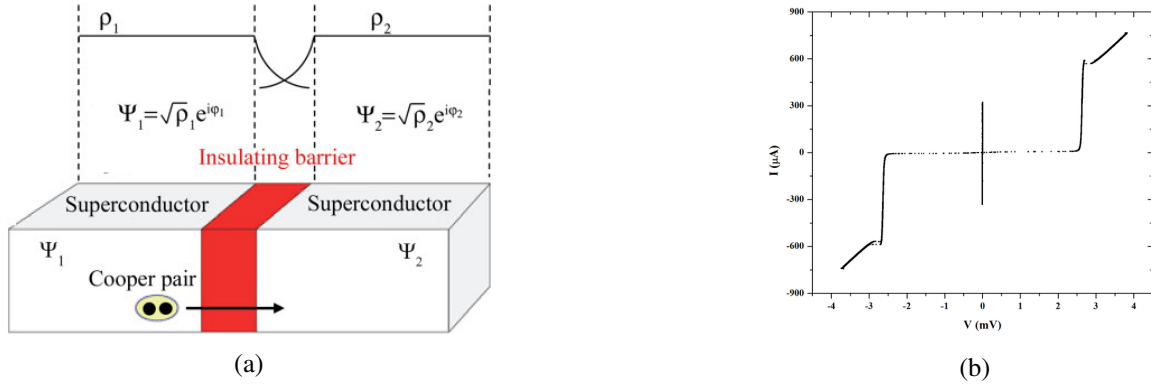


Figure 3: In (a) the circuitual schematics of a JJ showing a Cooper pair tunneling through the insulating barrier between two superconductor, due to the macroscopic wavefunctions superposition in the barrier. In (b), non-linear $I - V$ characteristic of a JJ when it is current-biased by and external DC current.

1.3 From CPB to Transmon

The starting point to describe the dynamics of a superconducting qubit circuit is the classical description of a linear LC resonant circuit (Fig. 4a), a system in which the energy oscillates between electrical energy in the capacitor C and magnetic energy in the inductor L [7].

The Hamiltonian of LC circuit is analogous to that of harmonic oscillators with frequency $\omega = \sqrt{LC}$ and mass $m = C$,

$$H = \frac{Q^2}{2C} + \frac{\Phi^2}{2L}. \quad (6)$$

Defining the reduced flux $\phi = 2\pi\Phi/\Phi_0$ and the reduced charge $n = Q/2e$, and promoting them to quantum operators, it is possible to write down the quantum-mechanical Hamiltonian:

$$H = 4E_C n^2 + \frac{1}{2} E_L \phi^2, \quad (7)$$

where $E_C = e^2/(2C)$ is the charging energy required to add each electron of the Cooper-pair to the island and $E_L = (\Phi_0/2\pi)^2/L$ is the inductive energy. The quantum operator n is the excess number of Cooper-pairs on the island, and ϕ is the “gauge-invariant phase” across the inductor.

The Hamiltonian in Eq. (7) is identical to that of a quantum harmonic oscillator (QHO) with ϕ as the generalized position coordinate, where the first term corresponds to the kinetic energy and the second term is the potential energy. The solution to this eigenvalue problem gives an infinite series of eigenstates $|k\rangle$ with $k \in \mathcal{N}$, whose corresponding eigenenergies E_k are all equidistantly spaced, $E_{k+1} - E_k = \hbar\omega_r$. Here, $\omega_r = \sqrt{8E_L E_C}/\hbar = 1/\sqrt{LC}$ denotes the resonant frequency of the system (Fig. 4b). This linear characteristic of the QHO makes the simple LC circuit inadequate for processing quantum information. As matter of fact, a system can be used as a qubit only if it is possible to define a computational subspace consisting of two well distinct and addressable energy states, in which transitions can be driven without exciting higher order energy levels in the system [7]. In order to solve this problem it is necessary to add some anharmonicity (or non-linearity) into the system, so to achieve different transition frequencies $\omega_{0 \rightarrow 1}$ and $\omega_{1 \rightarrow 2}$.

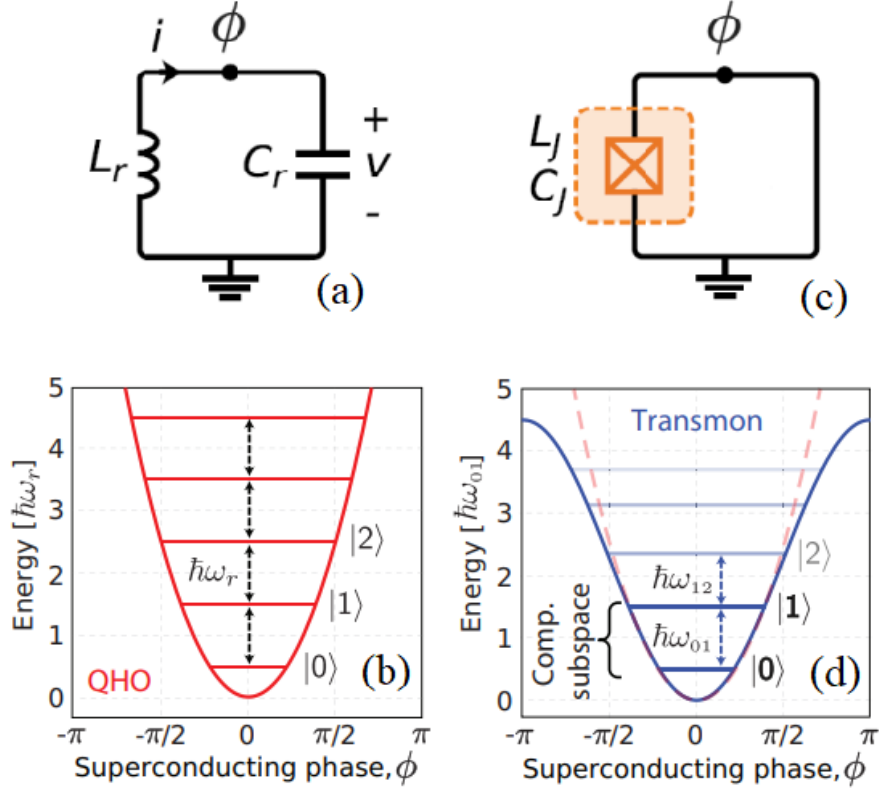


Figure 4: In (a) LC circuit schematics, with a potential energy that resembles a QHO energy levels in (b). In (c) circuit schematics of a JJ with non-linear potential energy (d).

The introduction of the Josephson junction (in Fig. 4c), a nonlinear, dissipationless circuit element, leads to the required conditions [7][8][9].

By replacing the linear inductor of the QHO with a Josephson junction, the Hamiltonian in Eq. (7) reads as

$$H = 4E_C n^2 - E_J \cos \varphi, \quad (8)$$

where $E_C = e^2/(2C_\Sigma)$, $C_\Sigma = C_s + C_J$ is the total capacitance, which includes the shunt capacitance C_s and the self-capacitance of the junction C_J , and E_J the Josephson energy (Sec. 1.2).

The Hamiltonian in Eq. (8) shows a potential energy that no longer takes a parabolic shape, but rather features a cosinusoidal form, which makes the energy spectrum non-degenerate and allows to identify a uniquely addressable quantum two-level system (Fig. 4d).

The system dynamics is governed by two dominant energy scales, reflected in the E_J/E_C ratio. This parameter is fundamental in order to define the working regime of a superconducting qubit.

As an example, one of the first implementation of a superconducting qubit, the **Cooper-pair box** (CPB), or charge qubit, is composed of a superconductive island linked to a charge reservoir by a Josephson Junction (Fig. 5), and works in $E_J \leq E_C$ regime (charge regime) [9].

The CPB Hamiltonian is:

$$\hat{H} = 4E_C (\hat{n} - n_g)^2 - E_J \cos \hat{\varphi}, \quad (9)$$

where \hat{n} and n_g denote the number of Cooper pairs transferred between the islands and the effective offset charge of the device, measured in units of the Cooper pair charge $2e$. The offset charge can be externally controlled by a gate voltage V_g capacitively coupled to the island such that $n_g = \frac{Q}{2e} + \frac{C_g V_g}{2e}$ [17].

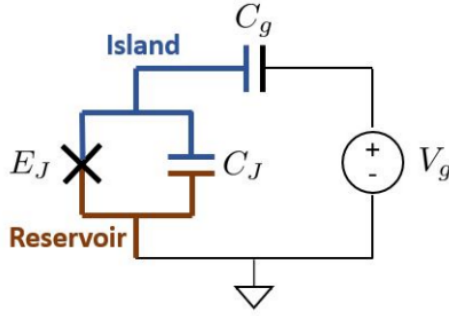


Figure 5: Circuital diagram of a CPB with a single JJ.

The CPB Hamiltonian in Eq. (9) can be solved exactly in the phase basis in terms of Mathieu functions [26] whose eigenenergies are:

$$E_m(n_g) = E_C a_{2[n_g + k(m, n_g)]}(-E_J/2E_C). \quad (10)$$

Here $a_\nu(q)$ denotes Mathieu's characteristic value, and $k(m, n_g)$ is a function sorting the eigenvalues. As shown in Fig. 6, the eigenenergy spectrum of the CPB depends on the ratio E_J/E_C . In case of low E_J/E_C , the energy levels strongly fluctuates as a function the gate offset charge. This induces a high charge noise sensitivity far from the so-called "sweetspots", i.e. where $dE/dn_g = 0$. This is the main reason why CPBs had shown low coherence times, which made their use impractical in large-scale quantum computing [17]. However, in Ref. [9], it is shown that, by increasing the E_J/E_C ratio around 50, it is possible to efficiently suppress charge noise fluctuations, so that the energy levels become more and more stable against charge noise.

In order to increase the ratio E_J/E_C , the JJ in the CPB is shunted by a capacitor in parallel C_q (Fig. 7a). In this way, the total capacitance of the circuit is increased, thus effectively reducing the charging energy to around few hundreds of megahertz. This novel device is called **transmon** (transmission line shunted plasma oscillation) qubit, and typically uses Aluminum JJs with critical currents of the order of few tens of nanoamperes [8]. This provides Josephson energies of few tens of gigahertz, that compared with E_C gives $E_J/E_C \gg 1$.

One of the fundamental quantities of a transmon qubit is the anharmonicity [9]:

$$\alpha = E_{12} - E_{01}, \quad (11)$$

with E_{ij} the energy separation between levels i and j . A transmon qubit is basically a weakly anharmonic oscillator with a negative anharmonicity, $\alpha = -E_C$ [7]. It is then important to mention that reducing E_C , also the anharmonicity decreases. This may seem a drawback: as the higher order energy levels become more similar in energy to the computational two-level system, they start to interfere. However, the transmon exploits a remarkable property: the charge dispersion reduces exponentially in E_J/E_C , while the anharmonicity only decreases algebraically with a slow power law in E_J/E_C , hence an energy ratio sufficiently large ($E_J/E_C \geq 50$) can suppress charge sensitivity, while at the same time preserving the computational space from higher order energy levels on a certain extent [9].

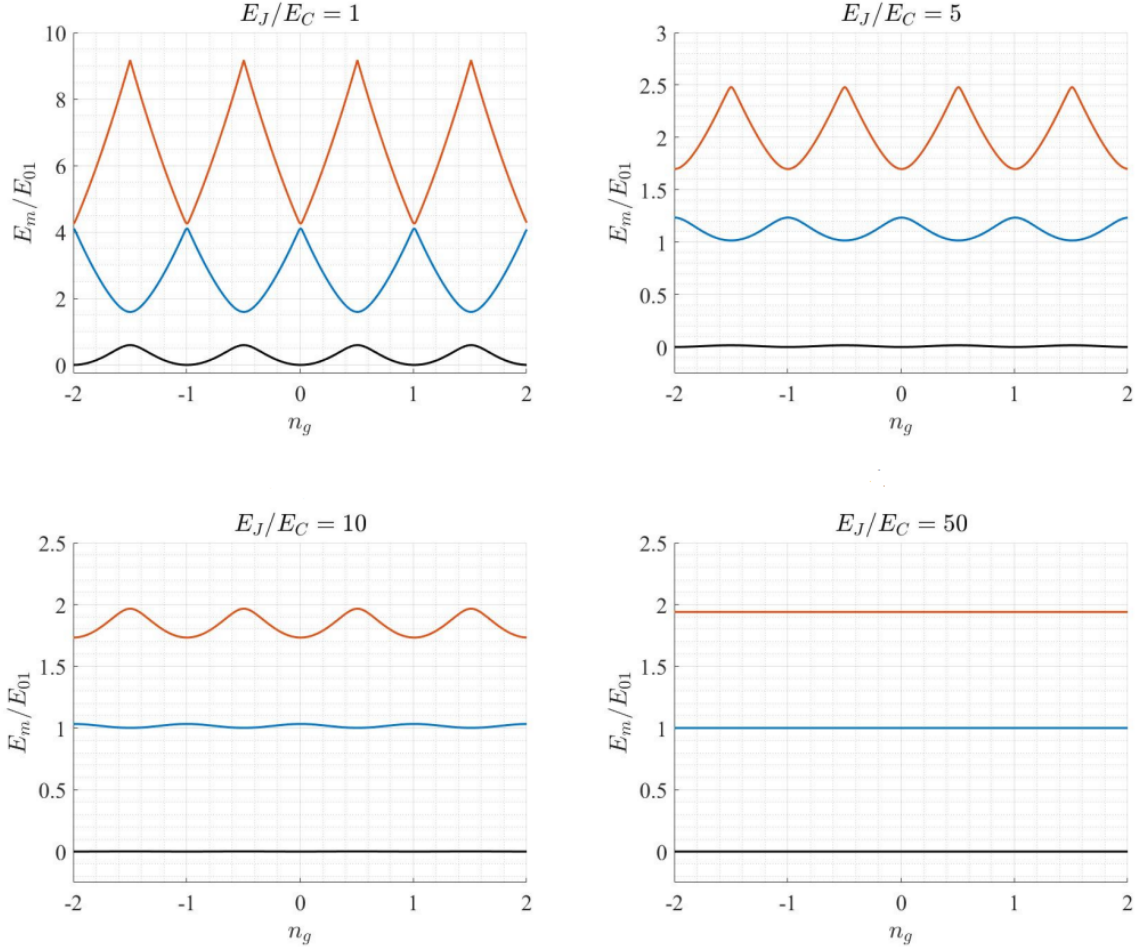


Figure 6: Eigenenergies E_m (first three levels, $m = 0, 1, 2$ of the qubit Hamiltonian) as a function of the effective offset charge n_g for different ratios E_J/E_C . Energies are given in units of the transition energy E_{01} , evaluated at the degeneracy point $n_g = 1/2$.

1.4 Control and Readout in Transmons

Transmon qubit versatility relies on its circuitual design. It is engineered to feature flux tunability by external flux, allowing to tune the qubit frequency for certain applications, as well as to tune more qubits on resonance establishing quantum entanglement between coupled qubits. Moreover, it is possible to perform quantum non-demolition readout measurement of the qubit state, and to control the qubit state through opportunely shape drive pulses.

1.4.1 Flux tunability

One widely-used technique in transmon architectures is to use a loop interrupted by two identical junctions in place of a single JJ, forming a DC Superconducting Quantum Interference Device (**DC-SQUID**) (Fig. 7) [9]. Due to the interference between the two arms of the SQUID, the total critical current of the DC-SQUID can be tuned by applying a magnetic flux threading the loop. In this case, the transmon is flux-tunable, and is also known as *split-transmon*. The addition of a flux-tunable element in the circuit is the key to implement two-qubit gate operations, allowing to set two qubits on resonance in a controlled way.

Exploiting the DC-SQUID loop it is possible to tune up the transmon, modifying the effective E_J by applying an external magnetic flux ϕ_{ext} [27]:

$$\omega_q(\phi_{ext}) = \sqrt{8E_J(\phi_{ext})E_C} - \frac{E_C}{2}, \quad (12)$$

where

$$E_J(\phi_{ext}) = E_{J\Sigma} \cos\left(\frac{\pi\phi_{ext}}{\phi_0}\right) \sqrt{1 + d^2 \tan^2\left(\frac{\pi\phi_{ext}}{\phi_0}\right)}, \quad (13)$$

and, being $E_{J1,2}$ the Josephson energies of the two JJs of the SQUID,

$$d = \frac{E_{J1} - E_{J2}}{E_{J1} + E_{J2}}. \quad (14)$$

The latter is known as asymmetry parameter and can influence the flux effect on the qubit frequency in terms of noise sensitivity: working at zero derivative points $\frac{d\omega_q}{d\phi_{ext}} = 0$ flux noise sensitivity is always minimized [9]. However, for asymmetric split-transmons, the qubit frequency typically assumes a smoother dependence as a function of the external flux fields, thus allowing to operate the qubit even far from the sweetspot [9]. In this thesis, we have worked with symmetric flux-tunable transmons. Therefore, we typically prefer to work in the sweetspot of the qubits to suppress flux noise, whenever possible.

1.4.2 Quantum non-demolition readout

To achieve high fidelity quantum non-demolition (QND) measurements, transmons are operated in the “dispersive” regime [7]. Since the qubit in transmon architecture is capacitively coupled to a superconducting resonator, which acts as a probe, it is possible to infer the qubit state by interrogating the resonator rather than directly interacting with the qubit.

The qubit-resonator interaction is described by the Jaynes-Cummings Hamiltonian:

$$H_{JC} = \omega_r \left(a^\dagger a + \frac{1}{2} \right) + \frac{\omega_q}{2} \sigma_z + g \left(\sigma_+ a + \sigma_- a^\dagger \right), \quad (15)$$

where ω_r and ω_q denote the resonator and qubit frequencies, respectively, g is the transverse qubit-resonator coupling rate, a^\dagger and a are the resonator single excitation creation and annihilation operators, σ_+ and σ_- operators represent the qubit exciting and de-exciting processes.

In the $\Delta = |\omega_q - \omega_r| \ll g$ limit, detuning between the qubit and the resonator is small compared with their coupling rate and excitations are coherently swapped between the two systems leading to a quantum demolition readout. Instead, in dispersive regime, the qubit is far detuned from the resonator, thus $\Delta \gg g$, and there is no longer a direct exchange of energy between the two systems. In this regime the Hamiltonian in Eq. (15) can be approximated using second-order perturbation theory in terms of g/Δ , known as the dispersive approximation [28]:

$$H_{JC_d} = (\omega_r + \chi\sigma_z) \left(a^\dagger a + \frac{1}{2} \right) + \frac{\widetilde{\omega}_q}{2} \sigma_z, \quad (16)$$

where $\chi = g^2/\Delta$ is the *dispersive shift* and $\widetilde{\omega}_q = \omega_q + g^2/\Delta$ is an induced Lamb shift due to the void fluctuations in the resonator. Hence, since the readout resonator frequency will shift depending on the state of the qubit, as shown in Fig. 7b, it is possible to encode the quantum state into specific voltage levels by fixing the readout resonator frequency corresponding to the $|0\rangle$ state of the qubit.

It is worth to note that the dispersive regime applies only in the so called “*low-photon*” regime, i.e. when the readout signal has sufficiently low power. As a matter of fact, the qubit-resonator coupling strength g depends on the number of photons in the resonator [7]. The larger this number, the higher is the chance to saturate the qubit energy levels, falling in what is known as *bare state* of the resonator.

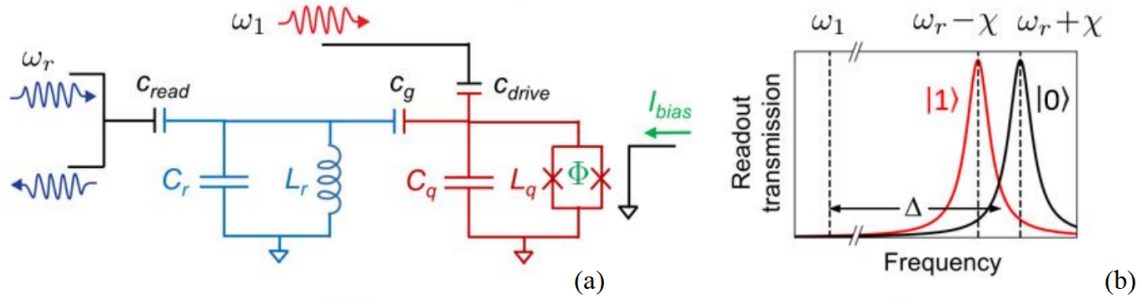


Figure 7: In (a) equivalent circuit of a flux-tunable transmon qubit coupled with a LC resonator for readout (light blue), and a transmission line for control signals (black). In (b) the dispersive shift χ of the resonator frequency ω_r depending on the qubit state.

1.4.3 Qubit drive

The initialization of qubit state, stated by Di Vincenzo criteria II, and the qubit driving along the Bloch sphere, is obtained through a controlled radio frequency (RF) signal, which resonates with the qubit, and is shaped according to the desired operation. In case of a capacitive coupling between the drive signal and the transmon (Fig. 7a), the Hamiltonian reads as [7]:

$$H = H_{JC} + H_d = H_{JC} + \frac{C_d}{C_\Sigma} V_d(t) \hat{Q}, \quad (17)$$

where H_{JC} is the transmon Hamiltonian (Eq. (15)), \hat{Q} is the charge operator, C_d is the coupling capacitance, $C_\Sigma = C_d + C$ the total capacitance, and $V_d(t)$ is the drive signal. By writing \hat{Q} in terms of raising and lowering operators

$$\hat{Q} = -iQ_{zpf}(a - a^\dagger), \quad (18)$$

where $Q_{zpf} = \sqrt{\hbar/2Z}$ is the zero-point charge fluctuations and $Z = \sqrt{L/C}$ is the impedance of the circuit to ground, and since $(a - a^\dagger) \propto \sigma_y$, the drive Hamiltonian H_d becomes:

$$H_d = \frac{C_d}{C_\Sigma} V_d(t) \sqrt{\hbar/2Z} \sigma_y, \quad (19)$$

and the total qubit Hamiltonian (omitting for simplicity the readout term in Eq. (16)) becomes:

$$H = \underbrace{-\frac{\omega_q}{2} \sigma_z}_{H_0} + \underbrace{\Omega V_d(t) \sigma_y}_{H_d}, \quad (20)$$

where $\Omega = \frac{C_d}{C_\Sigma} \sqrt{\hbar/2Z}$, and H_0 is the qubit two level system with ω_q its transition frequency. Then, using the Rotating Wave Approximation (RWA), the drive Hamiltonian reads as [7]:

$$H_d = \Omega V_d(t) (\sigma_y \cos \omega_q t - \sigma_x \sin \omega_q t). \quad (21)$$

Assuming that the drive voltage $V_d(t)$ has the generic form

$$V_d(t) = V_0 s(t) \sin(\omega_d t + \phi) = V_0 s(t) (\cos \phi \sin \omega_d t + \sin \phi \cos \omega_d t), \quad (22)$$

where $V_0 s(t)$ sets the drive amplitude with $s(t)$ a dimensionless envelope function, and adopting the definitions

$$I = \cos \phi \quad \text{In-phase component}, \quad (23)$$

$$Q = \sin \phi \quad \text{Out-of-phase component}, \quad (24)$$

one can apply the prosthaphaeresis formulae. Finally, by expressing the drive pulse in the dipole approximation, valid for $\delta\omega = \omega_q - \omega_d \ll \omega_q + \omega_d$, one can drop fast rotating terms and H_d takes the form:

$$\tilde{H}_d = \frac{\Omega V_0 s(t)}{2} [(-I \cos \delta\omega t + Q \sin \delta\omega t) \sigma_x + (I \sin \delta\omega t - Q \cos \delta\omega t) \sigma_y]. \quad (25)$$

When $\delta\omega = 0$, i.e. when the drive signals resonate with the qubit frequency,

$$\tilde{H}_d = \frac{\Omega V_0 s(t)}{2} (I\sigma_x + Q\sigma_y), \quad (26)$$

showing that for an in-phase pulse ($\phi = 0$) the drive applies a rotation around the x -axis of the Bloch sphere, whereas for an out-of-phase pulse ($\phi = \frac{\pi}{2}$) it applies a rotation around the y -axis. Therefore, one can implement the main single-qubit gates in the universal gate set reported later in Sec. 2.2.2, i.e. the X and Y gates, opportunely setting the phase of drive signals.

1.5 Couplings between superconducting qubit

The implementation of two-qubit gates requires a coupling between two qubits which can be achieved in many ways, for instance via direct capacitive or inductive coupling or via capacitively coupled resonator [7].

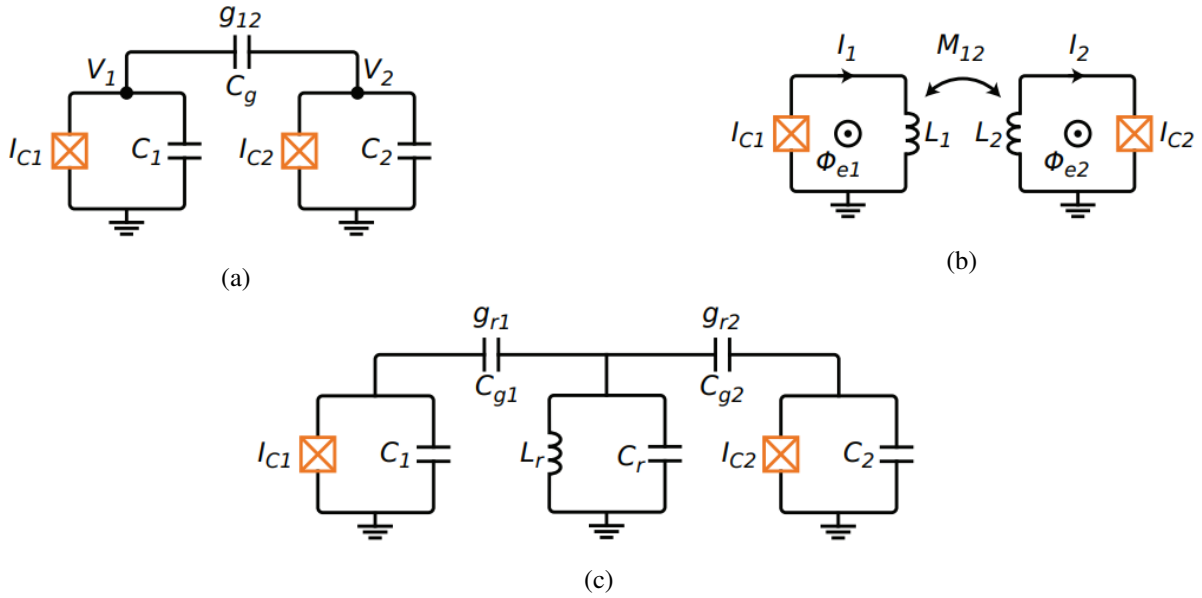


Figure 8: Schematic of capacitive and inductive coupling between two superconducting qubits: in (a) direct capacitive coupling, where the voltage nodes of two qubits V_1 and V_2 are connected by a capacitance C_g ; in (b) direct inductive coupling, where the two qubits are coupled via mutual inductance M_{12} ; in (c) capacitive coupling via a coupler in form of a linear resonator.

The Hamiltonian that describes two coupled systems takes the generic form:

$$H = H_1 + H_2 + H_{int}. \quad (27)$$

In this case, $H_{1,2}$ represent the isolated qubits Hamiltonians, while H_{int} is the interaction term, which features different forms according to the particular coupling. Taking into account two transmon qubits capacitively coupled through a high-frequency resonator coupler (Fig. 8c), which is specifically the case of the device analyzed in this work, the effective Hamiltonian of this system in the dispersive limit, i.e.

when both qubits frequency is detuned from the resonator coupler frequency, takes the form [29]:

$$H_{eff} = \sum_{i=1,2} \left(\frac{\hbar\omega_{qi}}{2} + \hbar\chi_i\sigma_i^z \right) + \hbar\omega_r a^\dagger a + \hbar J(\sigma_1^- \sigma_2^+ + \sigma_2^- \sigma_1^+), \quad (28)$$

where ω_{qi} are the qubits frequencies, ω_r is the resonance frequency of the coupling resonator and $\pm\chi_i$ are the dispersive qubit-state-dependent shifts of the resonator frequency. The last term describes the transverse exchange interaction between the qubits of strength $J = \frac{g_1 g_2}{2} \left(\frac{1}{\Delta_1} + \frac{1}{\Delta_2} \right)$ with the detuning $\Delta_{1,2} = \omega_{1,2} - \omega_r$ and coupling strengths $g_{1,2}$: the qubit-qubit interaction results in a virtual exchange of photons with the coupling resonator. When the qubits are degenerate with each other, an excitation in one qubit can be transferred to the other qubit by virtually becoming a photon in the cavity. Coherent interaction between the two qubits is observed by performing spectroscopy of their transition frequencies while applying a magnetic flux in order to tune qubits on resonance with each other and revealing an "avoided level crossing" (Fig. 9). The new eigenstates of the coupled system are [30]:

$$\left\{ |00\rangle, |\psi_s\rangle = \frac{1}{\sqrt{2}} (|01\rangle + |10\rangle), |\psi_a\rangle = \frac{1}{\sqrt{2}} (|01\rangle - |10\rangle), |11\rangle \right\}. \quad (29)$$

For large qubit-qubit detuning, i.e. $\delta \rightarrow \infty$, the two two-level systems realize asymptotically $|01\rangle$ and $|10\rangle$ states, as $|\psi_a\rangle \rightarrow |10\rangle$ and $|\psi_s\rangle \rightarrow |01\rangle$. On the other hand, when the detuning δ decreases, the entangled $|\psi_s\rangle$ and $|\psi_a\rangle$ are realized and a gap opens in the energy spectrum. The possibility to establish an avoided level crossing, hence a finite exchange of energy between two qubits, is fundamental for the implementation of multi-qubit gates.

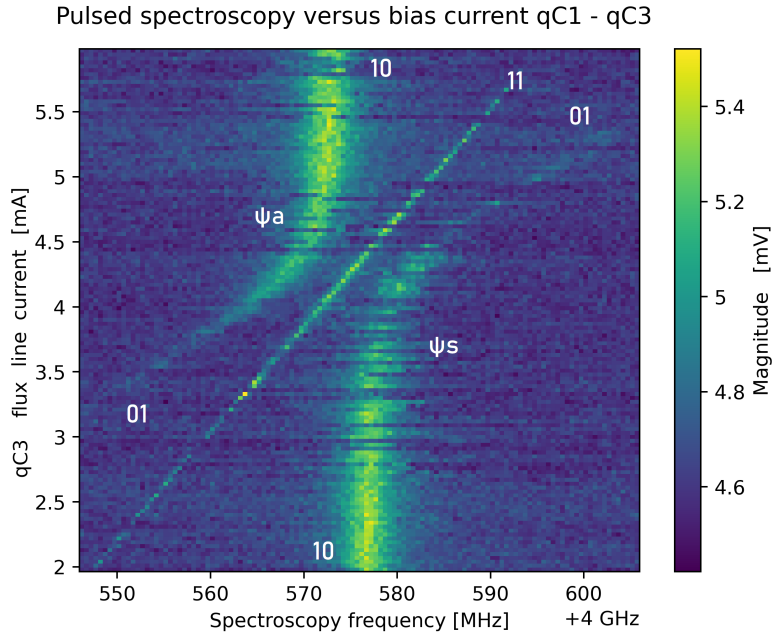


Figure 9: Spectroscopic measurement of the avoided level crossing as function of flux threading one qubit (qC3) with the second qubit at a fixed frequency (qC1).

2 Coherence and Fidelity benchmarking

The possibility to implement quantum algorithms in superconducting quantum processors is currently severely limited by three main bottlenecks:

- i) The number of coupled qubits so far is still not yet compatible with the required number to perform feasible quantum computing [14];
- ii) The errors committed when implementing quantum gates are still too large;
- iii) Superconducting qubits are strongly affected by decoherence, even more when considering multiple qubits coupled together.

In this thesis, we have characterized a 25-qubit transmon-based superconducting quantum processing unit, which behaves as a NISQ (Noisy and Intermediate-Scale Quantum) device [13]. This is the first prototype in Italy, and among the very few in Europe, with such a complexity in terms of number of coupled qubits on the same chip, which will be used in the near future for the implementation of quantum algorithms. As a first fundamental step in order to assess its feasibility for such implementation, it is required to study its performances in terms of fidelity and coherence, which is the main goal of this work. In this chapter, we provide the theory behind this interesting subject, which will be discussed and applied in the remaining of this work.

2.1 Impact of noise in qubits

Random, uncontrollable physical processes in the qubit control and measurement equipment, or in the local environment surrounding the quantum processor, are sources of noise that lead to decoherence and reduce the operational fidelity of the qubits [7].

The source of noise can be categorized in: *systematic noise*, which arises from a process that is traceable to a fixed control or readout error, leading to the same error each time, and then can be corrected through proper calibration; *stochastic noise*, which arises from random fluctuations of parameters that are coupled to our qubit. In turn, decoherence phenomena can be primarily categorized in **longitudinal relaxation**, **transverse relaxation** and **pure dephasing** [7].

Within the standard Bloch-Redfield picture of two-level system dynamics, the density matrix ρ_{BR} for the qubit state (Eq. (1)) reads as:

$$\rho_{BR} = \begin{pmatrix} 1 + (|\alpha|^2 - 1)e^{-\Gamma_1 t} & \alpha\beta^* e^{i\delta\omega t} e^{-\Gamma_2 t} \\ \alpha^*\beta e^{-i\delta\omega t} e^{-\Gamma_2 t} & |\beta|^2 e^{-\Gamma_1 t} \end{pmatrix}, \quad (30)$$

in which $e^{-\Gamma_1 t}$ and $e^{-\Gamma_2 t}$ are, respectively, the longitudinal and transverse decay functions, and the $e^{i\delta\omega t}$ term, where $\delta\omega = \omega_q - \omega_d$, accounts for cases where the qubit frequency ω_q differs from the rotating-frame frequency ω_d . Note that the matrix is constructed such that for $t \gg (T_1, T_2)$, the upper-left matrix element will approach unit value, indicating that all the population relaxes to the ground state.

2.1.1 Longitudinal relaxation

The longitudinal relaxation rate Γ_1 is defined as:

$$\Gamma_1 \equiv \frac{1}{T_1}. \quad (31)$$

T_1 is the 1/e decay time in the exponential decay function in Eq. (30), and it is the characteristic time scale over which the qubit population will relax to ground state.

Indeed, Γ_1 rate describes the depolarization, often referred to as "energy relaxation", along the qubit quantization axis (see Fig. 10). This depolarization occurs due to energy exchange with an environment,

generally leading to both an "up transition rate" $\Gamma_{1\uparrow}$ (excitation from $|0\rangle$ to $|1\rangle$), and a "down transition rate" $\Gamma_{1\downarrow}$ (relaxation from $|1\rangle$ to $|0\rangle$). Thus, the longitudinal relaxation rate can be written as:

$$\Gamma_1 \equiv \frac{1}{T_1} = \Gamma_{1\uparrow} + \Gamma_{1\downarrow}. \quad (32)$$

These transition processes follow the Boltzmann equilibrium statistics, then $\Gamma_{1\uparrow} \propto e^{-\frac{\hbar\omega_q}{k_B T}}$. Since superconducting qubits are typically operated at very low temperatures, $\Gamma_{1\uparrow}$ can be neglected and only the down-rate $\Gamma_{1\downarrow}$ contributes. For superconducting transmon qubits, typical T_1 values are of the order of tens or few hundreds of μs [7].

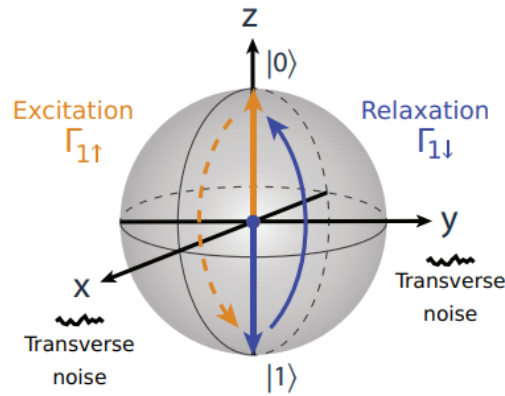


Figure 10: Longitudinal relaxation of the qubit state on the Bloch sphere [7].

Longitudinal relaxation is caused by transverse noise, which couples to the qubit via the x - or y -axis, driving transitions between states $|0\rangle$ and $|1\rangle$. Types of noise which lead to longitudinal relaxation are:

- Spontaneous emission, i.e. radiative decay due to the qubit coupling with the electromagnetic field inside the transmission line resonator [9];
- Purcell effect, i.e. an enhanced spontaneous emission of photons that occurs into the readout resonant cavity [7][9][31];
- Charge noise in terms of dielectric losses, due to the charge fluctuations in the defects or charge traps that reside in interfacial dielectrics, in the junction tunnel barrier and in the substrate of the qubit [7];
- Quasiparticle noise, due to thermal breaking of Cooper pairs [7][32];
- Flux coupling noise, due to the coupling of the transmon to an external magnetic flux bias, for tuning purpose, when on resonance with the qubit [7]. Coherence times in presence of this noise are of the order of milliseconds [7], thus compared with the other mentioned above, doesn't affect predominantly the qubit relaxation.

2.1.2 Pure dephasing

The pure dephasing rate Γ_φ describes depolarization in the $x - y$ plane of the Bloch sphere. Pure dephasing is caused by longitudinal noise that couples to the qubit via the z -axis leading to stochastic fluctuations of qubit frequency ω_q , such that it is no longer equal to the rotating frame frequency ω_d , and causing the Bloch vector to precess forward or backward in the rotating frame, leading to a complete depolarization of the azimuthal angle φ (see Fig. 11).

In contrast to energy relaxation, pure dephasing is not a resonant phenomenon, therefore noise at any frequency can modify the qubit. Secondly, since pure dephasing doesn't involve energy exchange with the environment, it is in principle reversible.

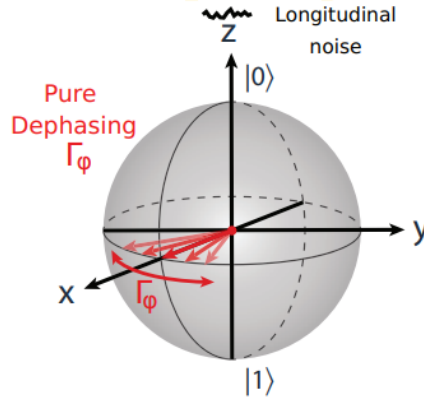


Figure 11: Pure dephasing of a qubit on the Bloch sphere [7].

In case of transmon qubit, principal noise sources that lead to pure dephasing are:

- Charge noise, which derives from fluctuations of the charge in the superconducting islands of a JJ [7];
- Magnetic flux noise, which originates from the stochastic flipping of magnetic dipoles (spins) that reside on the surfaces of the superconducting metals comprising the qubit, and resulting in random fluctuations of the effective magnetic field that biases flux-tunable qubits [7][9];
- Critical current noise, which is generated by trapping and detrapping of charges associated with spatial reconfigurations of ions inside the JJ [9];
- Photon number fluctuation, typically due to radiation coming from higher temperature stages in the cryogenic environment used to cooldown the qubit [7].

2.1.3 Transverse relaxation

The transverse relaxation rate is:

$$\Gamma_2 \equiv \frac{1}{T_2} = \frac{\Gamma_1}{2} + \Gamma_\phi. \quad (33)$$

It describes the loss of coherence of a superposition state (for example $\frac{1}{\sqrt{2}}(|0\rangle + |1\rangle)$) and it is caused by both longitudinal noise and transverse noise. Such a relaxation event is also a phase-breaking process, because once it occurs, the Bloch vector points to the north pole $|0\rangle$ (see Fig. 12), and there is no longer any knowledge of which direction it was pointing along the equator. In other words, the relative phase of the superposition state is lost. For superconducting transmon qubits, typical T_2 values are of the order of tens or few hundreds of μs [7].

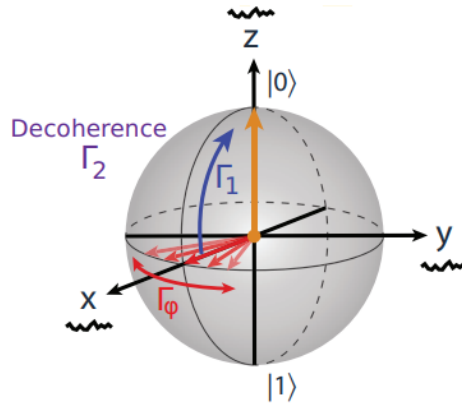


Figure 12: Transverse relaxation of a qubit on the Bloch sphere [7].

2.2 Universal Quantum Computing

The Di Vincenzo criteria *IV* demands for a Universal set of logic operations in order to physically implement a quantum computer. Superconducting quantum processors successfully answer for this requirement, since they allow to implement what is known as "*Gate-based Quantum Computing*". The minimum number of gates required to build a universal quantum computer defines a "universal gate set" [7], which must include operations that are able to rotate the Bloch vector around arbitrary axes on the Bloch sphere (i.e. a complete single-qubit gate set), and at least one entangling two-qubit operation. As shown in Sec. 1.4, the circuitual design of superconducting transmon qubits allows for the implementation of controllable rotations around the different axes of the Bloch sphere, henceforth to design microwave and flux pulses able to perform single-qubit gates. Moreover, the possibility to couple two or more qubits in the processor allows to perform two-qubit gates. In the following, we will report a detailed description of the most fundamental single- and two-qubit gates in transmon qubits.

2.2.1 Single-qubit gates

In classical boolean logic, bits can assume two deterministic values, state 0 or state 1, whereas qubits, as discussed in Sec. 1.1, besides the classical states $|0\rangle$ and $|1\rangle$, can also assume arbitrary superpositions $\alpha|0\rangle + \beta|1\rangle$, corresponding to any other position on the sphere.

Single-qubit operations, i.e. quantum single-qubit gates, translate an arbitrary quantum state from one point on the Bloch sphere to another point by rotating the Bloch vector a certain angle about a particular axis. As shown in Fig. 13, there are several single-qubit gates, each represented by a unitary matrix that describes the quantum operation in the computational basis of the σ_z operator eigenvectors, i.e. $|0\rangle \equiv [1 \ 0]^T$ and $|1\rangle \equiv [0 \ 1]^T$ [7].

In particular, as shown in Fig.13:

- ▷ The *Identity gate* \mathbb{I} ideally performs no rotation on the state of the qubit.
- ▷ The *X, Y and Z gates* perform a π rotation about the respective axis.
- ▷ The *S-gate* performs a $\pi/2$ rotation about the z axis.
- ▷ The *T-gate* performs a rotation of $\pi/4$ about the z axis.
- ▷ The *Hadamard gate* H performs a π rotation about an axis diagonal in the $x - z$ plane.

GATE	CIRCUIT REPRESENTATION	MATRIX REPRESENTATION	TRUTH TABLE	BLOCH SPHERE						
I Identity-gate: no rotation is performed.		$I = \begin{pmatrix} 1 & 0 \\ 0 & 1 \end{pmatrix}$	<table border="1"> <thead> <tr> <th>Input</th> <th>Output</th> </tr> </thead> <tbody> <tr> <td> 0⟩</td> <td> 0⟩</td> </tr> <tr> <td> 1⟩</td> <td> 1⟩</td> </tr> </tbody> </table>	Input	Output	0⟩	0⟩	1⟩	1⟩	
Input	Output									
0⟩	0⟩									
1⟩	1⟩									
X gate: rotates the qubit state by π radians (180°) about the x-axis.		$X = \begin{pmatrix} 0 & 1 \\ 1 & 0 \end{pmatrix}$	<table border="1"> <thead> <tr> <th>Input</th> <th>Output</th> </tr> </thead> <tbody> <tr> <td> 0⟩</td> <td> 1⟩</td> </tr> <tr> <td> 1⟩</td> <td> 0⟩</td> </tr> </tbody> </table>	Input	Output	0⟩	1⟩	1⟩	0⟩	
Input	Output									
0⟩	1⟩									
1⟩	0⟩									
Y gate: rotates the qubit state by π radians (180°) about the y-axis.		$Y = \begin{pmatrix} 0 & -i \\ i & 0 \end{pmatrix}$	<table border="1"> <thead> <tr> <th>Input</th> <th>Output</th> </tr> </thead> <tbody> <tr> <td> 0⟩</td> <td>$i 1\rangle$</td> </tr> <tr> <td> 1⟩</td> <td>$-i 0\rangle$</td> </tr> </tbody> </table>	Input	Output	0⟩	$i 1\rangle$	1⟩	$-i 0\rangle$	
Input	Output									
0⟩	$i 1\rangle$									
1⟩	$-i 0\rangle$									
Z gate: rotates the qubit state by π radians (180°) about the z-axis.		$Z = \begin{pmatrix} 1 & 0 \\ 0 & -1 \end{pmatrix}$	<table border="1"> <thead> <tr> <th>Input</th> <th>Output</th> </tr> </thead> <tbody> <tr> <td> 0⟩</td> <td> 0⟩</td> </tr> <tr> <td> 1⟩</td> <td>$- 1\rangle$</td> </tr> </tbody> </table>	Input	Output	0⟩	0⟩	1⟩	$- 1\rangle$	
Input	Output									
0⟩	0⟩									
1⟩	$- 1\rangle$									
S gate: rotates the qubit state by $\frac{\pi}{2}$ radians (90°) about the z-axis.		$S = \begin{pmatrix} 1 & 0 \\ 0 & e^{i\frac{\pi}{2}} \end{pmatrix}$	<table border="1"> <thead> <tr> <th>Input</th> <th>Output</th> </tr> </thead> <tbody> <tr> <td> 0⟩</td> <td> 0⟩</td> </tr> <tr> <td> 1⟩</td> <td>$e^{i\frac{\pi}{2}} 1\rangle$</td> </tr> </tbody> </table>	Input	Output	0⟩	0⟩	1⟩	$e^{i\frac{\pi}{2}} 1\rangle$	
Input	Output									
0⟩	0⟩									
1⟩	$e^{i\frac{\pi}{2}} 1\rangle$									
T gate: rotates the qubit state by $\frac{\pi}{4}$ radians (45°) about the z-axis.		$T = \begin{pmatrix} 1 & 0 \\ 0 & e^{i\frac{\pi}{4}} \end{pmatrix}$	<table border="1"> <thead> <tr> <th>Input</th> <th>Output</th> </tr> </thead> <tbody> <tr> <td> 0⟩</td> <td> 0⟩</td> </tr> <tr> <td> 1⟩</td> <td>$e^{i\frac{\pi}{4}} 1\rangle$</td> </tr> </tbody> </table>	Input	Output	0⟩	0⟩	1⟩	$e^{i\frac{\pi}{4}} 1\rangle$	
Input	Output									
0⟩	0⟩									
1⟩	$e^{i\frac{\pi}{4}} 1\rangle$									
H gate: rotates the qubit state by π radians (180°) about an axis diagonal in the x-z plane. This is equivalent to an X-gate followed by a $\frac{\pi}{2}$ rotation about the y-axis.		$H = \frac{1}{\sqrt{2}} \begin{pmatrix} 1 & 1 \\ 1 & -1 \end{pmatrix}$	<table border="1"> <thead> <tr> <th>Input</th> <th>Output</th> </tr> </thead> <tbody> <tr> <td> 0⟩</td> <td>$\frac{ 0\rangle + 1\rangle}{\sqrt{2}}$</td> </tr> <tr> <td> 1⟩</td> <td>$\frac{ 0\rangle - 1\rangle}{\sqrt{2}}$</td> </tr> </tbody> </table>	Input	Output	0⟩	$\frac{ 0\rangle + 1\rangle}{\sqrt{2}}$	1⟩	$\frac{ 0\rangle - 1\rangle}{\sqrt{2}}$	
Input	Output									
0⟩	$\frac{ 0\rangle + 1\rangle}{\sqrt{2}}$									
1⟩	$\frac{ 0\rangle - 1\rangle}{\sqrt{2}}$									

Figure 13: Quantum single-qubit gates. For each gate, the name, a short description, quantum circuit representation, matrix representation, truth tables, and effect on Bloch vector [7].

One can notice that I , X , Y , Z gates correspond to the Pauli matrices σ_0 , σ_x , σ_y and σ_z , respectively: since Pauli matrices are unitary, they are also reversible, thus applying a gate and its opposite should result in the state vector returning to its original form [7]. Moreover, it's important to say that applying the *Hadamard* gate to a single qubit creates a superposition state of both $|0\rangle$ and $|1\rangle$. Indeed by making several measurements of the qubit state, prepared in the $|0\rangle$ state, after a H -gate is applied, a 50% probability to be either in $|0\rangle$ or in $|1\rangle$ should be observed, unless statistical errors are present [33].

2.2.2 Two-qubit gates

Two-qubit quantum-logic gates are generally conditional gates and take two qubits as inputs, one as control qubit, and the other as target qubit [7]. These gates are represented by unitary operators in the two-qubit state basis vectors $|00\rangle \equiv [1 \ 0 \ 0 \ 0]^T$, $|01\rangle \equiv [0 \ 1 \ 0 \ 0]^T$, $|10\rangle \equiv [0 \ 0 \ 1 \ 0]^T$, $|11\rangle \equiv [0 \ 0 \ 0 \ 1]^T$ which are applied to the target qubit, yielding a result depending on the control qubit state. Thus two-qubit gates are reversible operations too. Common two-qubit gates are (Fig. 14):

- ▷ The Controlled NOT (*CNOT*) gate, which flips the state of the target qubit when the control qubit is in the excited state $|1\rangle$.
- ▷ The Controlled Phase (*CPHASE* or *CZ*) gate applies a Z-gate to the target qubit when the control qubit is in state $|1\rangle$.
- ▷ The *i*SWAP gate acts to swap an excitation between the two qubits providing an additional phase.

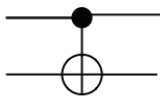
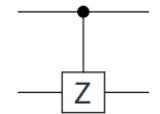
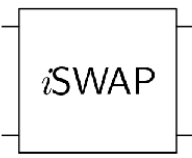
GATE	CIRCUIT REPRESENTATION	MATRIX REPRESENTATION	TRUTH TABLE										
Controlled-NOT gate: apply an X-gate to the target qubit if the control qubit is in state $ 1\rangle$		$CNOT = \begin{pmatrix} 1 & 0 & 0 & 0 \\ 0 & 1 & 0 & 0 \\ 0 & 0 & 0 & 1 \\ 0 & 0 & 1 & 0 \end{pmatrix}$	<table border="1"> <thead> <tr> <th>Input</th> <th>Output</th> </tr> </thead> <tbody> <tr> <td>$00\rangle$</td> <td>$00\rangle$</td> </tr> <tr> <td>$01\rangle$</td> <td>$01\rangle$</td> </tr> <tr> <td>$10\rangle$</td> <td>$11\rangle$</td> </tr> <tr> <td>$11\rangle$</td> <td>$10\rangle$</td> </tr> </tbody> </table>	Input	Output	$ 00\rangle$	$ 00\rangle$	$ 01\rangle$	$ 01\rangle$	$ 10\rangle$	$ 11\rangle$	$ 11\rangle$	$ 10\rangle$
Input	Output												
$ 00\rangle$	$ 00\rangle$												
$ 01\rangle$	$ 01\rangle$												
$ 10\rangle$	$ 11\rangle$												
$ 11\rangle$	$ 10\rangle$												
Controlled-phase gate: apply a Z-gate to the target qubit if the control qubit is in state $ 1\rangle$		$CPHASE = \begin{pmatrix} 1 & 0 & 0 & 0 \\ 0 & 1 & 0 & 0 \\ 0 & 0 & 1 & 0 \\ 0 & 0 & 0 & -1 \end{pmatrix}$	<table border="1"> <thead> <tr> <th>Input</th> <th>Output</th> </tr> </thead> <tbody> <tr> <td>$00\rangle$</td> <td>$00\rangle$</td> </tr> <tr> <td>$01\rangle$</td> <td>$01\rangle$</td> </tr> <tr> <td>$10\rangle$</td> <td>$10\rangle$</td> </tr> <tr> <td>$11\rangle$</td> <td>$- 11\rangle$</td> </tr> </tbody> </table>	Input	Output	$ 00\rangle$	$ 00\rangle$	$ 01\rangle$	$ 01\rangle$	$ 10\rangle$	$ 10\rangle$	$ 11\rangle$	$- 11\rangle$
Input	Output												
$ 00\rangle$	$ 00\rangle$												
$ 01\rangle$	$ 01\rangle$												
$ 10\rangle$	$ 10\rangle$												
$ 11\rangle$	$- 11\rangle$												
<i>i</i> SWAP gate: swaps an excitation between the two qubits		$iSWAP = \begin{pmatrix} 1 & 0 & 0 & 0 \\ 0 & 0 & -i & 0 \\ 0 & -i & 0 & 0 \\ 0 & 0 & 0 & 1 \end{pmatrix}$	<table border="1"> <thead> <tr> <th>Input</th> <th>Output</th> </tr> </thead> <tbody> <tr> <td>$00\rangle$</td> <td>$00\rangle$</td> </tr> <tr> <td>$01\rangle$</td> <td>$-i 10\rangle$</td> </tr> <tr> <td>$10\rangle$</td> <td>$-i 01\rangle$</td> </tr> <tr> <td>$11\rangle$</td> <td>$11\rangle$</td> </tr> </tbody> </table>	Input	Output	$ 00\rangle$	$ 00\rangle$	$ 01\rangle$	$-i 10\rangle$	$ 10\rangle$	$-i 01\rangle$	$ 11\rangle$	$ 11\rangle$
Input	Output												
$ 00\rangle$	$ 00\rangle$												
$ 01\rangle$	$-i 10\rangle$												
$ 10\rangle$	$-i 01\rangle$												
$ 11\rangle$	$ 11\rangle$												

Figure 14: Quantum two-qubit gates. For each gate, the name, a short description, quantum circuit and matrix representation, and the truth tables. Adapted from [7].

Some two-qubit gates, such as *CNOT* and *CZ*, are also called "*entangling gates*", because they can take product states as input and produce entangled states as output, also called *Bell states* [7].

To get the representative unitary matrix of *i*SWAP two-qubit gate, let's start from the total Hamiltonian $H = H_1 + H_2 + H_{int}$ (Eq. (27)). The interaction Hamiltonian H_{int} of two capacitively coupled qubits can be written as [7]:

$$H_{int} = J\sigma_{y1} \otimes \sigma_{y2}. \quad (34)$$

By using the RWA, then dropping the fast rotating terms, and exploiting the flux tunability to bring qubits on resonance by means of an external flux, Eq. (34) becomes [7]:

$$H_{int} = J(\sigma_1^+ \sigma_2^- + \sigma_1^- \sigma_2^+) = \frac{J}{2}(\sigma_{x1} \sigma_{x2} + \sigma_{y1} \sigma_{y2}). \quad (35)$$

Eq. (35) shows that a capacitive interaction leads to a swapping of excitations between the two qubits, also said 'XY' interaction. The unitary matrix corresponding to a XY (swap) interaction is:

$$U(t) = \begin{bmatrix} 1 & 0 & 0 & 0 \\ 0 & \cos Jt & -i \sin Jt & 0 \\ 0 & -i \sin Jt & \cos Jt & 0 \\ 0 & 0 & 0 & 1 \end{bmatrix}. \quad (36)$$

Again, tuning the qubits into resonance for a time $t = \frac{\pi}{2J}$, one can implement the i SWAP:

$$U\left(\frac{\pi}{2J}\right) = \begin{bmatrix} 1 & 0 & 0 & 0 \\ 0 & 0 & -i & 0 \\ 0 & -i & 0 & 0 \\ 0 & 0 & 0 & 1 \end{bmatrix} \equiv iSWAP, \quad (37)$$

which simultaneously swaps an excitation between the two qubits, adding a phase of $i = e^{i\frac{\pi}{2}}$. From an operative point of view, the i SWAP is performed at the avoided level crossing where $\Phi = \Phi_{iSWAP}$ (Fig. 9). It consists in fixing the lower frequency qubit in the pair in its sweetspot and then tuning the higher frequency qubit, initially prepared in its excited state $|1\rangle$, until they are on resonance. By waiting for a time τ in this configuration, the excitation is swapped back and forth between the two qubits, as shown in Fig. 15.

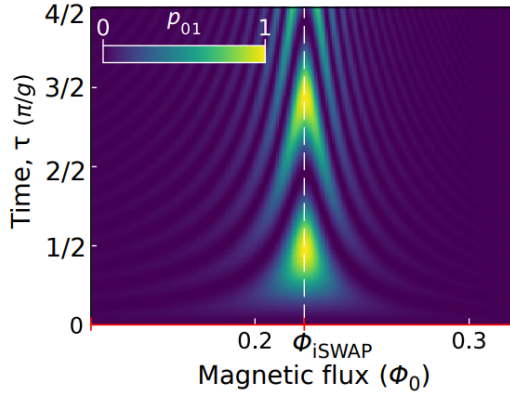


Figure 15: Probability of swapping into the $|01\rangle$ state as a function of time and flux. The pulse sequence corresponds to preparing the $|10\rangle$ state and performing a typical i SWAP operation for a time τ [7].

While for the i SWAP gate higher energy levels of the qubit could be neglected, in case of a transmon qubit they can be used to implement the CZ gate. It is possible to show that in order to implement a CZ gate the avoided level crossing must occur between the $|11\rangle$ and the $|20\rangle$ states. The Hamiltonian for this system written in the $\{|00\rangle, |01\rangle, |10\rangle, |11\rangle, |02\rangle, |20\rangle\}$ -basis is given by [7]:

$$H = \begin{bmatrix} E_{00} & 0 & 0 & 0 & 0 & 0 \\ 0 & E_{01} & J & 0 & 0 & 0 \\ 0 & J & E_{10} & 0 & 0 & 0 \\ 0 & 0 & 0 & E_{11} & \sqrt{2}J & \sqrt{2}J \\ 0 & 0 & 0 & \sqrt{2}J & E_{02} & 0 \\ 0 & 0 & 0 & \sqrt{2}J & 0 & E_{20} \end{bmatrix}, \quad (38)$$

where the $|02\rangle, |20\rangle \leftrightarrow |11\rangle$ transitions are scaled by a factor $\sqrt{2}$ due to the higher photon number [7].

By preparing the system in the state $|11\rangle$ and moving towards the avoided crossing, the resulting unitary operator in the computational basis is given by:

$$U_{ad}\left(\frac{\pi}{2J}\right) = \begin{bmatrix} 1 & 0 & 0 & 0 \\ 0 & e^{i\theta_{01}(\ell)} & 0 & 0 \\ 0 & 0 & e^{i\theta_{10}(\ell)} & 0 \\ 0 & 0 & 0 & e^{i\theta_{11}(\ell)} \end{bmatrix}, \quad (39)$$

where $\theta_{ij}(\ell(\tau))$ is the phase acquired by the state $|ij\rangle$ along the trajectory (ℓ) in (Φ, t) -space during time τ . The movement should be sufficiently slow on a time-scale set by J , i.e. the movement should be adiabatic. In terms of applied flux, the avoided crossing between the $|11\rangle \leftrightarrow |20\rangle$ state happens before $|10\rangle \leftrightarrow |01\rangle$ (due to the negative anharmonicity of the transmon, $\alpha \simeq -E_C$) and consequently ℓ does not take the states through the Φ_{iSWAP} operating point (see Fig.16). Moreover, it is possible to define the ζ parameter which quantifies the difference in phase acquired by the $|11\rangle$ relative to the single excitation states, also known as the repulsion of the $|11\rangle$ due to the $|20\rangle$ state [7]:

$$\zeta = (\omega_{11} - (\omega_{01} + \omega_{10})). \quad (40)$$

Then if one chooses a trajectory ℓ_π such that $\theta_{11} = \pi$ and, after the adiabatic process, the single-qubit phases get erased by means of applied flux, such that $\theta_{10}(\ell_\pi) = \theta_{01}(\ell_\pi) = 0$, the matrix in Eq. (39) becomes:

$$U_{ad} = \begin{bmatrix} 1 & 0 & 0 & 0 \\ 0 & 1 & 0 & 0 \\ 0 & 0 & 1 & 0 \\ 0 & 0 & 0 & -1 \end{bmatrix} \equiv CZ. \quad (41)$$

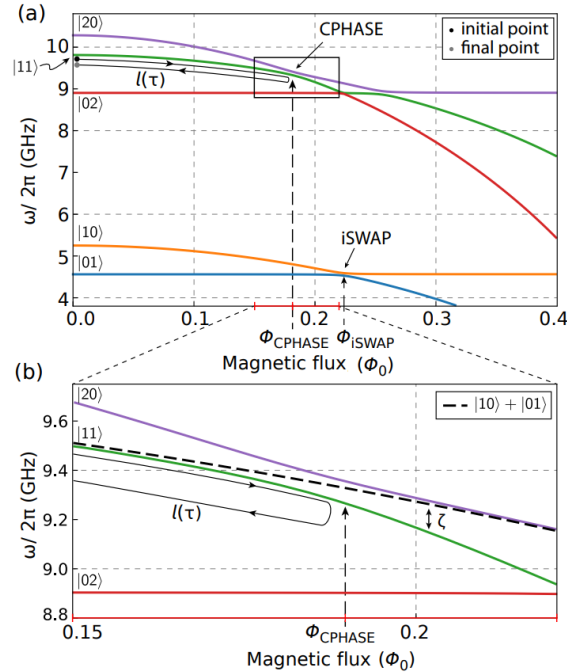


Figure 16: In (a) the spectrum of two coupled transmon qubits as a function of the local magnetic flux for the higher frequency qubit. The two lower branches corresponding to $|01\rangle$ and $|10\rangle$ are involved in the $iSWAP$ gate operation. The avoided crossing indicated in the black box is used to implement the CZ gate. The black line with arrows delimited by the gray and black dots indicates a $\ell(\tau)$ trajectory used to implement the gate. In (b) the zoom in of the $|20\rangle \leftrightarrow |11\rangle$ avoided crossing: the parameter ζ quantifies the difference in energy between $|11\rangle$ and $|10\rangle + |01\rangle$ [7].

Once discussed the main logical operations that one can implement in multi-qubit transmon devices, we can finally define an example of Universal gate set as [7]:

$$\mathcal{G}_0 = \{X_\theta, Y_\theta, Z_\theta, Ph_\theta, CNOT\}, \quad (42)$$

where $Ph_\theta = e^{i\theta}\mathbb{I}$ applies an overall phase θ to a single qubit. Therefore, a Universal gate set must include the minimum number of gates required to perform all possible operations in terms of Bloch vector rotations about arbitrary axes and entangling gates. Here, the $CNOT$ plays the role of entangling gate and it can be implemented by using both CZ gate combined with H gates or two $iSWAP$ gates combined with $X_{\frac{\pi}{2}}$ and $Z_{\pm\frac{\pi}{2}}$ gates (Fig. 17).

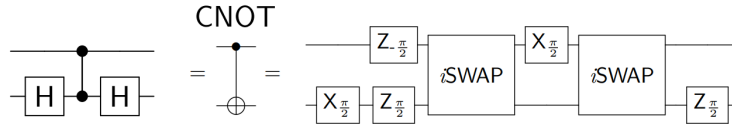


Figure 17: $CNOT$ gate implemented by using CZ or $iSWAP$ gates.

Moreover, in the frame of \mathcal{G}_0 gate set, the Hadamard gate can be decomposed as:

$$H = Ph_{\frac{\pi}{2}} Y_{\frac{\pi}{2}} Z_{\pi} = i \frac{1}{\sqrt{2}} \begin{bmatrix} 1 & -1 \\ 1 & 1 \end{bmatrix} \begin{bmatrix} -i & 0 \\ 0 & i \end{bmatrix} = \frac{1}{\sqrt{2}} \begin{bmatrix} 1 & 1 \\ 1 & -1 \end{bmatrix}. \quad (43)$$

It is therefore quite clear that, in order to successfully run quantum algorithms, it must be possible to implement each and any of these gates in the best way possible, i.e. with the lowest chance of error. In this thesis, we have focused on one particular technique to quantify the gate fidelity and benchmark the performances of a quantum processor: the randomized benchmarking.

2.3 Fidelity and Randomized Benchmarking

The number of performable gates in a quantum computer has been theorized to be orders of magnitude larger than the number of available qubits. Then, to build and test such a large system, a modular design is essential. The concept of scalable gate-based quantum computing denotes a strategy of designing systems and gates in testable sub-parts, keeping well in mind errors in computational quantum gates are unavoidable. However, one can make an effort in detecting, mitigating and correcting such errors, falling under the broad title of *fault-tolerance* [57]. In this paradigm, by reducing the probability that a gate acts erroneously, one can reduce the extra coding overheads required. Therefore, it is first of all important to define a way to quantify quantum processors performances in terms of their error rate.

The scientific community introduced a mathematical and physical way to quantify the quality of the qubit performances by means of the *state*, *gate* and *readout fidelity* [15]. In this thesis we will focus in particular on the evaluation of gate fidelity.

For a system consisting of n qubits, there are 2^n pure quantum states that correspond to classical states of n bits (i.e. $\{|0\rangle, |1\rangle\}$ for a single qubit and $\{|00\rangle, |01\rangle, |10\rangle, |11\rangle\}$ for two qubits). These orthogonal states additively generate all pure quantum states of n qubits, thus a vector space V over the complex numbers of dimension 2^n [15]. When describing systems about which one does not have complete knowledge, for instance when there is a possibility of unwanted interaction to occur, it is useful the concept of mixed states, i.e. statistical ensembles of pure states. Any mixed state of a finite number of qubits can be represented by a density matrix $\rho = \sum_{i,j} \rho_{i,j} |i\rangle\langle j|$, with $\{|i\rangle\}_i$ in any basis in V . Moreover, mixed states can be represented as $2^n \times 2^n$ matrices over complex numbers. Here we report some properties of these density matrix:

- ρ is Hermitian and positive semi-definite;
- $Tr(\rho) = 1$;
- $\rho^2 = \rho$.

An interaction that maps all pure states into other pure states is constrained to have a unitary (or anti-unitary) matrix representation U acting on the space vector V . The result of this interaction acting on a system represented by a density matrix ρ is given by $U\rho U^\dagger$. In practice, $U\rho U^\dagger$ represents the ideal implementation of unitary quantum gates. However, the implementation of these gates will always be affected by environmental noise which leads to decoherence, so they will not actually be unitary. Being $\hat{\Lambda}_U$ the experimental implementation of a gate, the quality of $\hat{\Lambda}_U$ is the degree to which the density operator $\hat{\Lambda}_U(\rho) = \Lambda\rho\Lambda^\dagger$ is close to $U\rho U^\dagger$.

The *state fidelity* describes the discrepancy between an experimental density matrix σ and its theoretical expectation ρ as [15]:

$$F(\rho, \sigma) = Tr \left(\sqrt{\sqrt{\rho}\sigma\sqrt{\rho}} \right)^2. \quad (44)$$

Note that if $\rho = |\psi\rangle\langle\psi|$ is a pure state, then $F(|\psi\rangle\langle\psi|, \sigma) = \langle\psi|\sigma|\psi\rangle$. Moreover, if $\sigma = |\phi\rangle\langle\phi|$ is also a pure state, then the definition further simplifies to $F(|\psi\rangle\langle\psi|, |\phi\rangle\langle\phi|) = |\langle\psi|\phi\rangle|^2$, which is the square of the overlap between the two pure states.

The definition of state fidelity can be extended to a definition of *gate fidelity* as [15]:

$$F(U, \hat{\Lambda}_U) = \int d\rho F(U\rho U^\dagger, \hat{\Lambda}_U(\rho)). \quad (45)$$

Operationally, this fidelity describes the average probability that, after initializing the system in a random known state, a measurement after an applied operation will result in the correct expected final state.

For a pure state $\rho = |\psi\rangle\langle\psi|$, the integrand in Eq. (45) becomes:

$$F(U\rho U^\dagger, \hat{\Lambda}_U(\rho)) = \langle\psi|U^\dagger\hat{\Lambda}_U(|\psi\rangle\langle\psi|)U|\psi\rangle, \quad (46)$$

which reduces to 1 if $\hat{\Lambda}_U(\rho) = U\rho U^\dagger$, i.e. $\hat{\Lambda}_U$ exactly implements the unitary gate U .

There are two fundamental difficulties in practically exploiting such definition: first, averaging over all pure states is not experimentally possible, and second, no ideal inverse gate exists. The first problem might be solved if the integral over all states in the gate fidelity definition is formally equal to a sum over a finite representative set of states. About the second problem, if the inverting gate U^\dagger is actually a faulty operation $\hat{\Lambda}_{U^\dagger}$ as well (as it must be in a real experiment), then one must attempt to distinguish between the errors of the operations $\hat{\Lambda}_{U^\dagger}$ and $\hat{\Lambda}_U$ in the data analysis through gate fidelity comparison.

An alternative approach to fidelity calculation is the *Randomized Benchmarking* (RB) procedure, a Monte-Carlo integration over a randomized set of quantum states [15]. This approach relies on random initialization and measurements of the system state: the advantage of a randomized approach is in its faster convergence rate, simplicity, and immunity to certain adversarial noise models. Moreover, the solution employed by the RB for the ill-characterized gates is to try to ensure that the preparation and measurement steps are consistently faulty in a simple way so that these faults might be estimated and eliminated during the analysis [34]. The RB procedure extracts the average gate fidelity over a set of gates by performing fidelity estimations on randomized sequences of gates from that set, thus, the resultant fidelity describes the aggregate quality of the quantum control, instead of the quality of any particular gate. This makes standard RB a poor tool for diagnosing specific errors but an excellent tool for describing overall performance.

In standard RB procedure the chosen gate set for the fidelity test is the so called Clifford gate set. Clifford gates are generated by $C_i = e^{\pm i\sigma_u \frac{\pi}{2}}$ with $u = x, y$, then the complete set of single-qubit Clifford gates is $\{\mathbb{I}, \pm X_\pi, \pm Y_\pi, \pm Z_\pi, \pm X_{\frac{\pi}{2}}, \pm Y_{\frac{\pi}{2}}, \pm Z_{\frac{\pi}{2}}\}$ [35]. The RB protocol steps are then:

- Initialize the system in the ground state;
- Apply a sequence of random Clifford gates, in the pattern $\prod_i C_i \mathcal{P}_i$ with \mathcal{P}_i the Pauli rotations, i.e. \mathbb{I}, X, Y and Z ;
- Apply the last inverse Clifford or Pauli pulse to return to the initial state, i.e. the ground state;
- Perform repeated measurements of the state to estimate the average fidelity;
- Repeat with an increased number of applied gates.

In case no error has occurred during the operations sequence, the system would return to its initial state and the experimental fidelity should be equal to 100%, i.e. the probability to measure the ground state is 1. However experimental average fidelity features an exponential decay with the increasing number of Clifford gates (called also "survival probability") due to the noise effecting operations outputs and that can be well described with the introduction of the depolarizing channel [15]. The depolarizing channels are superoperators of the form $(1 - p)X + \frac{p \text{Tr}(X)}{d} \mathbb{I}$ parameterized by a single real number p , called *strength*: a depolarizing channel of strength 0 is the identity superoperator and does not change whatever operator to which it is applied; a depolarizing channel of strength 1 replaces the operator with a normalized identity operator (with $d = 2^n$). Lastly, considering the composition of two depolarizing channels $\hat{\Lambda}_a$ with strength p_a and $\hat{\Lambda}_b$ with strength p_b [15],

$$\left(\hat{\Lambda}_a \circ \hat{\Lambda}_b\right)(X) = (1 - p_a)(1 - p_b)X + (1 - (1 - p_a)(1 - p_b)) \frac{\text{Tr}(X)}{d} \mathbb{I} \quad (47)$$

is also a depolarizing channel with strength $(1 - (1 - p_a)(1 - p_b))$. Then, the average fidelity of a length- l sequence is described by a product of l depolarizing channels of the same strength $p_s = \frac{\epsilon_s}{\alpha_n}$, with ϵ_s the probability that a step could introduce an error, and one additional depolarizing channel of different strength $p_m = \frac{\epsilon_m}{\alpha_n}$ with ϵ_m corresponding to the State Preparation And Measurement (SPAM) probability errors. The result is a depolarizing channel with strength $1 - (1 - p_m)(1 - p_s)^l$ which gives the average fidelity as [15]:

$$F_l = (1 - \alpha_n) + \alpha_n \left(1 - \frac{\epsilon_m}{\alpha_n}\right) \left(1 - \frac{\epsilon_s}{\alpha_n}\right)^l, \quad (48)$$

where $\alpha_n = \frac{2^n - 1}{2^n}$ for n qubits. Therefore, the measurement of the gate fidelity allows to get information on the quality of the gate implemented on the actual hardware too.

Finally, with optimized control, the fidelity is limited by decoherence processes such as energy decay and dephasing. The reduction on average fidelity due to these uncorrelated process for a N -qubit system is [36]:

$$\bar{F}_N = 1 - \frac{d}{2(d+1)} \tau \sum_{k=1}^N \left(\Gamma_1^k + \Gamma_\varphi^k \right), \quad (49)$$

where $d = 2^N$, Γ_1 and Γ_φ are the characteristic rates of the qubit, and τ is the mean duration of the gate regardless of which one is applied (further details in Appendix A).

Finally, let us now give a definition of *readout fidelity*, which is strictly related to the Signal to Noise Ratio (*SNR*) of the integrated signal power of the detector used to infer qubit state. In transmon qubits, for example, it is related to the *SNR* of the voltage measured across the readout resonator in the dispersive regime used to identify the qubit state indirectly and in a quantum non-demolitive way (Sec. 1.4.2). A qualitative relationship is given by the formula [37]:

$$F = \text{erf} \left(\sqrt{\frac{\tau_{int} SNR}{2}} \right), \quad (50)$$

where erf is the error function and $\tau_{int} = \frac{t}{T_1}$ is a dimensionless integration time normalized to the qubit decay time. This expression, valid only in the ideal case of no qubit decay, states that maximizing the *SNR* correspond to maximizing the fidelity. A specific definition of *SNR* is given in Ref. [38]:

$$SNR = \frac{\eta \kappa |\beta|^2 \cos^2(\theta_\beta - \phi)}{\Gamma_1}, \quad (51)$$

where:

- $\eta = \frac{\kappa_{out}}{\kappa_{in} + \kappa_{out}} \frac{1}{N_{noise} + 1}$ is the detection efficiency, where N_{noise} is the effective number of noise photons in the measurement and, κ_{in} and κ_{out} are the resonator decay rates with respect to the input and output line capacitively coupled (see Fig. 18) [39]. The model suggests that once a photon has entered the resonator, it has only two possible paths to exit. Then, measuring only at the output port (i.e. in the limit $\kappa_{out} \gg \kappa_{in}$) this value approaches the maximum of 1. It is quite important to note that when working in the dispersive regime, input signals in the readout resonator of a transmon are very weak, and therefore cryogenic amplification stages are required, which add to the complexity of the circuitual components on chip. In fact, considering the noise figure, defined as $\mathcal{F} = SNR_{in}/SNR_{out}$, which describes the degradation of the *SNR* as it passes through each circuitual component, it is shown that cascaded components lead to a total noise figure given by [39]:

$$\mathcal{F}_{tot} = \mathcal{F}_1 + \frac{\mathcal{F}_2 - 1}{G_1} + \frac{\mathcal{F}_3 - 1}{G_1 G_2} + \dots, \quad (52)$$

where \mathcal{F}_i is the noise factor at the i^{th} stage of amplification and G_i is the gain of the i^{th} amplification stage. This formula states that the first amplifier is the most important for the effective noise level of the system, i.e. N_{noise} [39].

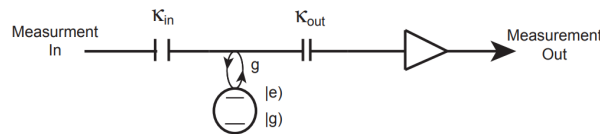


Figure 18: Readout line couplings with the inferred resonator [39].

- The presence of $\kappa = \kappa_{in} + \kappa_{out}$ in Eq. (51) is only a formal issue, since it would be canceled considering the explicit form of η . However, it is important to note that larger κ will also result in a larger Purcell decay, actually resulting to be a damping factor. Purcell decay rate is given by [39]:

$$\kappa \frac{g^2}{\Delta^2} = \Gamma_{Purcell} \geq \Gamma_1 = \frac{1}{T_1}, \quad (53)$$

where g and Δ are, respectively, the coupling and the frequency detuning between the qubit and the resonator (Sec. 1.4.2).

- $\beta = \alpha_e(t) - \alpha_g(t)$ is the state discrepancy, i.e. the distance in the (I,Q)-plane between the ground state $|\alpha_e(t)\rangle$ and the excited state $|\alpha_g(t)\rangle$, with the associated angle $\theta_\beta = \arg(\beta)$ (Fig. 19). It gives information about how well the readout hardware is able to distinguish between the two possible output states, detecting the actual output of a operation.

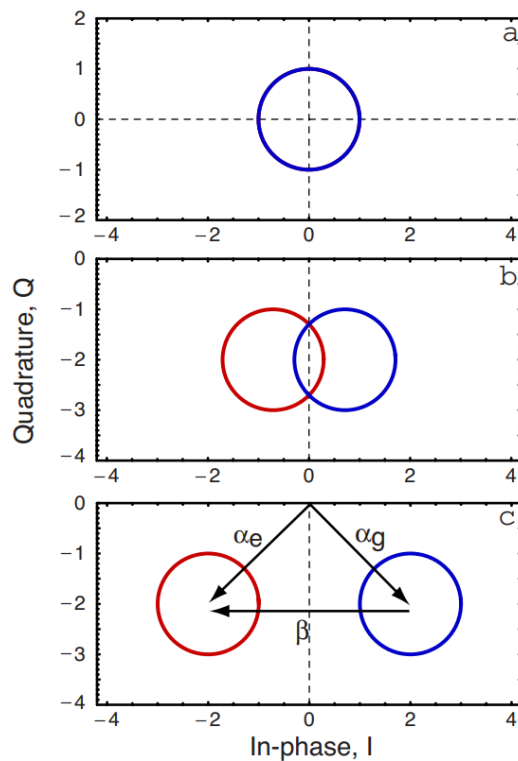


Figure 19: Representation of the resonator state in (I,Q)-space for increasing qubit-field interaction times, i.e. photon population in resonator, from $t = 0$ in (a) to steady state solutions in (c). In this last case $\theta_\beta = \pi$, corresponding to all of the information stored in the in-phase component I, and no information stored in the out-of-phase component Q [38].

In conclusion, the decoherence and the user's ability to prepare initial quantum states, as well as to implement Universal gate sets and readout its output, set a limit to the performances of a quantum computer, and it is fundamental to quantify all of the possible sources of error coming from decoherence effects, faulty control and readout. In this thesis, we have primarily focused on coherence and gate fidelity benchmarking, and will leave the study of readout fidelity to future work.

3 Experimental setup and protocols

In this chapter we will give an overview of the experimental setup exploited during this thesis, starting from the quantum processing unit design in Sec. 3.1. Then we will describe the dilution refrigerator system and the cooling procedure that allows to reach sufficiently low temperatures to operate the quantum processor in Sec. 3.2, and give an overview of cryogenic and room temperature electronics needed for control and readout signal generation in Sec. 3.3 and Sec. 3.4. Indeed, being the typical range of frequencies of transmon qubits compatible with $4 - 6 \text{ GHz}$, it is straightforward to note that the operation temperature should be below $100 - 200 \text{ mK}$. Dilution refrigerators are the best cryogenic platform to achieve this goal, and it is of fundamental importance to engineer the cryogenic electronics in order to protect the qubit from external spurious noise as much as possible to preserve coherence. Furthermore, we will give an overview of characterization procedures in Sec. 3.5 with a special focus on control and pulse shape optimization and errors correction protocols in Sec. 3.6 and 3.7, respectively. Lastly we will describe measurement protocols to characterize the qubit coherence times in Sec. 3.8 and the Randomized Benchmarking in Sec. 3.9.

3.1 Quantum Processing Unit (QPU)

The QPU characterized in this master thesis is a **Contralto-D** processor produced by QuantWare, spin-off company of the University of Delft [40].

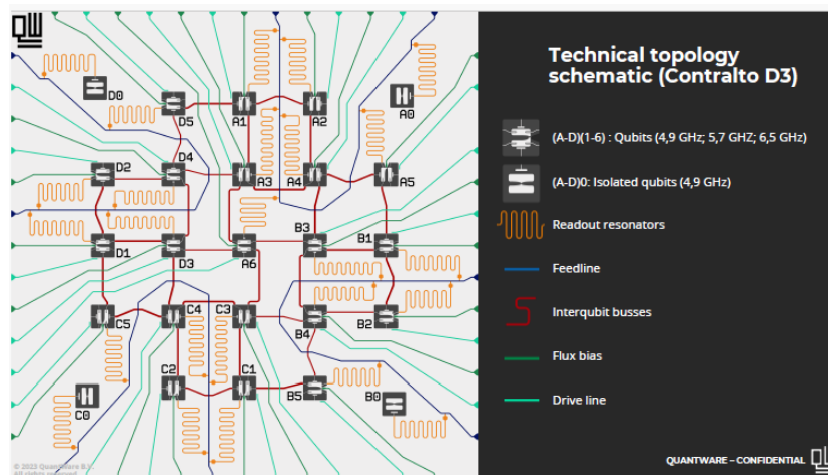


Figure 20: QPU circuitual schematics and description: false-color microscopic image of the QuantWare Contralto-D chip.

This processor features 21 fully connected flux-tunable qubits and 4 fixed-frequency isolated qubits. In Fig. 20, we show a microscope false-color image of the chip, provided by the producer and a schematic representation of the chip connectivity.

In order to perform multiplexed readout of the qubits, namely a simultaneous readout of all qubits through multimode signals, there are 4 feedlines (A,B,C,D marked in blue in Fig. 20 and 21) each connected to 5 qubits through superconducting CoPlanar Waveguide (CPW) readout resonators (marked in orange in Fig. 20 and 21), except for feedline A, which is coupled to 6 qubits. Readout resonators frequency depends on geometrical parameters, including the length of the CPW. On each feedline, the length of the resonators changes in order to guarantee different readout resonator frequencies, ranging from 7 to 7.8 GHz .

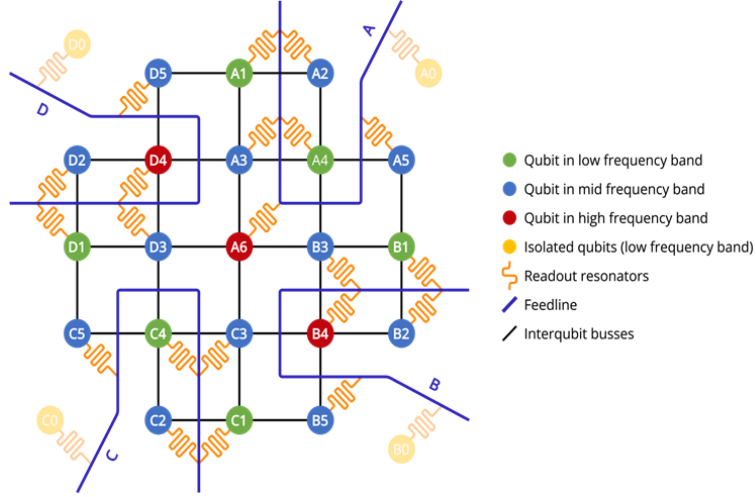


Figure 21: QPU circuitual schematics and description: schematic representation of the qubit-qubit matrix connectivity and frequency scales.

Every flux tunable qubit features a flux bias line and a drive line. The former is a transmission line inductively coupled to the superconducting DC-SQUID of the flux tunable transmon (marked in green in Fig. 20). In this way, current signals sent to these lines generate a concatenated and maximized magnetic field perpendicular to the area of the DC-SQUID. The latter is a capacitively coupled transmission line (marked in light green in Fig. 20), thus guaranteeing maximum coupling with the electric field counterpart of microwave radiations. This design is commonly depicted in state-of-the-art superconducting QPU, and well-known in superconducting transmon qubit design. Finally, the qubit in the QPU are coupled with their neighbors via resonator buses (marked in red in Fig. 20), in a rectangular-like 2D connection matrix, as schematized in Fig. 21.

Conversely, isolated qubits (A0, B0, C0, D0) are used for coherence benchmarking, being these systems not only isolated from other qubits, but also from external connections for control and frequency tunability.

Finally, qubits features different operative frequency bands, as typically requested for circuitual design suitable for advanced quantum error detection and correction [41]. By following the color coding in Fig. 21 we can identify:

- Green and yellow ones, working in a low frequency band ($\sim 4 - 5 \text{ GHz}$);
- Blue ones, working in a mid frequency band ($\sim 5 - 6 \text{ GHz}$);
- Red ones, working in a high frequency band ($\sim 6 - 7 \text{ GHz}$).

In the following we report the qubits and resonators parameters provided by the builder and to be compared with the measured ones (Tab.1).

	Qubit frequency GHz	Resonator frequency GHz
A1	4.82	7.20
A2	5.45	7.44
A3	5.56	7.56
A4	4.90	7.32
A5	5.45	7.68
A6	6.05	7.80
B1	4.72	7.20
B2	5.23	7.44
B3	5.39	7.56
B4	6.16	7.80
B5	5.45	7.68
C1	4.55	7.20
C2	5.38	7.44
C3	5.41	7.56
C4	4.61	7.32
C5	5.38	7.68
D1	4.63	7.20
D2	5.32	7.44
D3	5.34	7.56
D4	6.14	7.80
D5	5.19	7.68

Table 1: Contralto-D QPU qubits and resonators factory frequencies: in green low frequency band qubits, in blue mid frequency band qubits and in red high frequency band qubits.

The sample is then mounted on a PCB, which allows direct connection between the chip and the cryogenic lines, and protected first by a copper-plated cavity, and then by two stages of magnetic shielding, which use the Meissner effect to expel spurious external magnetic fields (Sec. 1.2). The sample package is finally mounted at the lowest temperature stage of a dilution refrigerator (Fig. 22).



Figure 22: Contralto-D QPU stage: at the center, the copper-plated cavity which hosts the qubits; on the edges, the qubits drive and flux lines, and feedlines connections.

3.2 The dilution refrigerator

Modern dilution refrigerators provide operative temperatures around 10 mK and exploit the peculiar thermodynamics of a mixture of $He^3 - He^4$, as proposed by H. London and G.R. Clarke [42]. The dilution procedure requires a starting temperature of about liquid helium (4.2 K). By means of the Joule-Thomson effect, the mixture is compressed and condensed, reaching the liquid He^3 temperature ($1.8 - 2\text{ K}$), thus allowing for both the two gases to be in the liquid phase at this stage (condensation). Then, at temperatures below 0.8 K (depending on concentration), the $He^3 - He^4$ mixture will separate into two phases: a He^3 rich phase (concentrated phase) and a He^3 poor phase (dilute phase), as shown in Fig. 23a. The concentrated phase becomes pure He^3 while in the dilute He^4 rich phase there is 6.6% of He^3 . The enthalpy of He^3 in the dilute phase is larger than in the concentrated phase, hence, the energy required to move He^3 atoms from the concentrated to the dilute phase is taken from a well isolated environment, named Mixing Chamber (see Fig. 23b, 8 and Fig. 24c), resulting in a cooling effect due the evaporation of the dilute phase. This process is called "evaporation", and occurs in the Still chamber (see Fig. 23b, 4 and Fig.24a). Together with the condensation and the dilution, this is one of the fundamental step in the cooldown procedure. The three steps are continuously run in a closed cycle through the use of scroll, turbo and compressors pumps in a Gas Handling System (GHS), connected to the cryostat through the condensing pumping line (used for inserting the mixture in the dilution unit, see Fig. 23b, 1), and Still pumping line (used to maintain the phase separation in the cycle in the evaporation process, see Fig. 23b, 2).

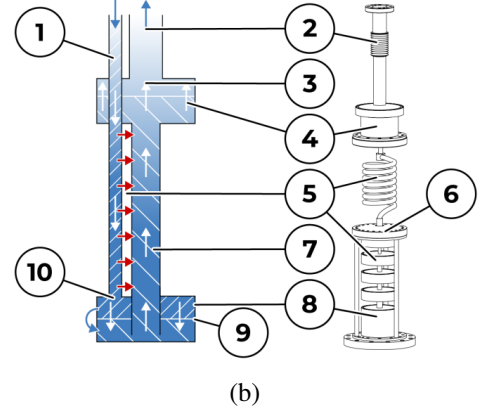
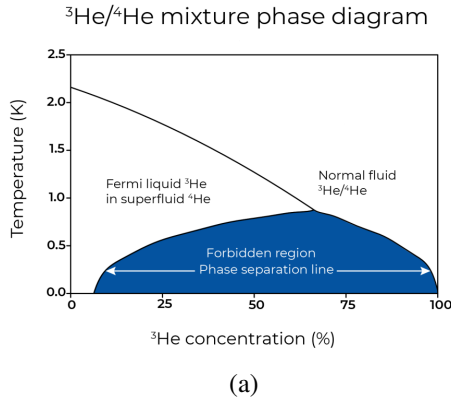


Figure 23: Evaporation process: in (a) Phase diagram of He^3-He^4 mixture. In (b) Dilution unit scheme: (1) Condensing Line, (2) Still Pumping Line, (3) He^3 rich gas phase, (4) Still, (5) Heat exchangers, (6) Cold Plate, (7) He^3 poor phase, (8) Mixing Chamber, (9) Phase separation, (10) He^3 rich phase.

Based on the different cooldown stages, the cryostat (see Fig. 24), a Bluefors **XLD1000SL** system [43], is made of several plates, characterized by different temperatures:

- the RT plate, where the connections to the GHS and the room-temperature electronics is made;
- the 50K plate, where a temperature of 50 K is reached in normal operation;
- the Still plate, where a temperature of ~ 800 mK is reached and the Still chamber (in Fig. 24a) sits;
- the Cold plate, where heat exchangers (in Fig. 24b) are located;
- the MXC plate, where two Mixing chambers (in Fig. 24a) are located, and is the coldest stage of the cryostat. Here, the base temperature in normal operation is of the order of 10 mK.

The dilution refrigerator used in this work is a dry dilution fridge, meaning that the 4.2K required for starting the condensation cycle is achieved through the use of two Cryomech Pulse Tube coolers. The pulse tubes are thermally anchored to the 50K plate, and to the 4K plate, through flexible copper braids to damp any possible vibration caused by the pulse tube. The mixture is henceforth precooled to < 4.2 K, assisted by the presence of different heat exchangers: first by a Cold Trap at approximately 50K which takes out any contamination of circulation by freezing; then by two Heat Switches¹ installed between the 4K flange and the Still flange and between the Still and MXC flanges that enable thermal contact during the initial pre-cool stage. The thermal contact is disabled once low temperature regime is reached.

3.3 Cryogenic electronics

The cryostat architecture is designed to host the cryogenic electronics required for qubit characterization. The cryostat is equipped with slots (sideloaders) dedicated to pre-assembled microwave RF coaxial cables sets, which can be freely moved, changed and upgraded. At the time of writing, the cryostat is equipped with a total of 96 lines, separated in three sideloaders. We have four types of lines engineered to fulfill specific operation tasks on the quantum processor: 48 control lines, 32 flux lines, 8 output lines and 8 pump lines, which will be dedicated in the future for Traveling Wave Parametric Amplification (TWPA) cryogenic devices [44]. Since in this work we have not yet exploited such devices, we won't give details on their operation, nor discuss the specifics of the cryogenic lines.

¹The Heat Switches consist of two copper heat exchanger parts, one on the high and on one the low temperature side, separated by a stainless-steel tube (designed to minimize heat transfer when disabled) and filled with helium gas (when enabled) that plays the role of heat conductor medium between them.

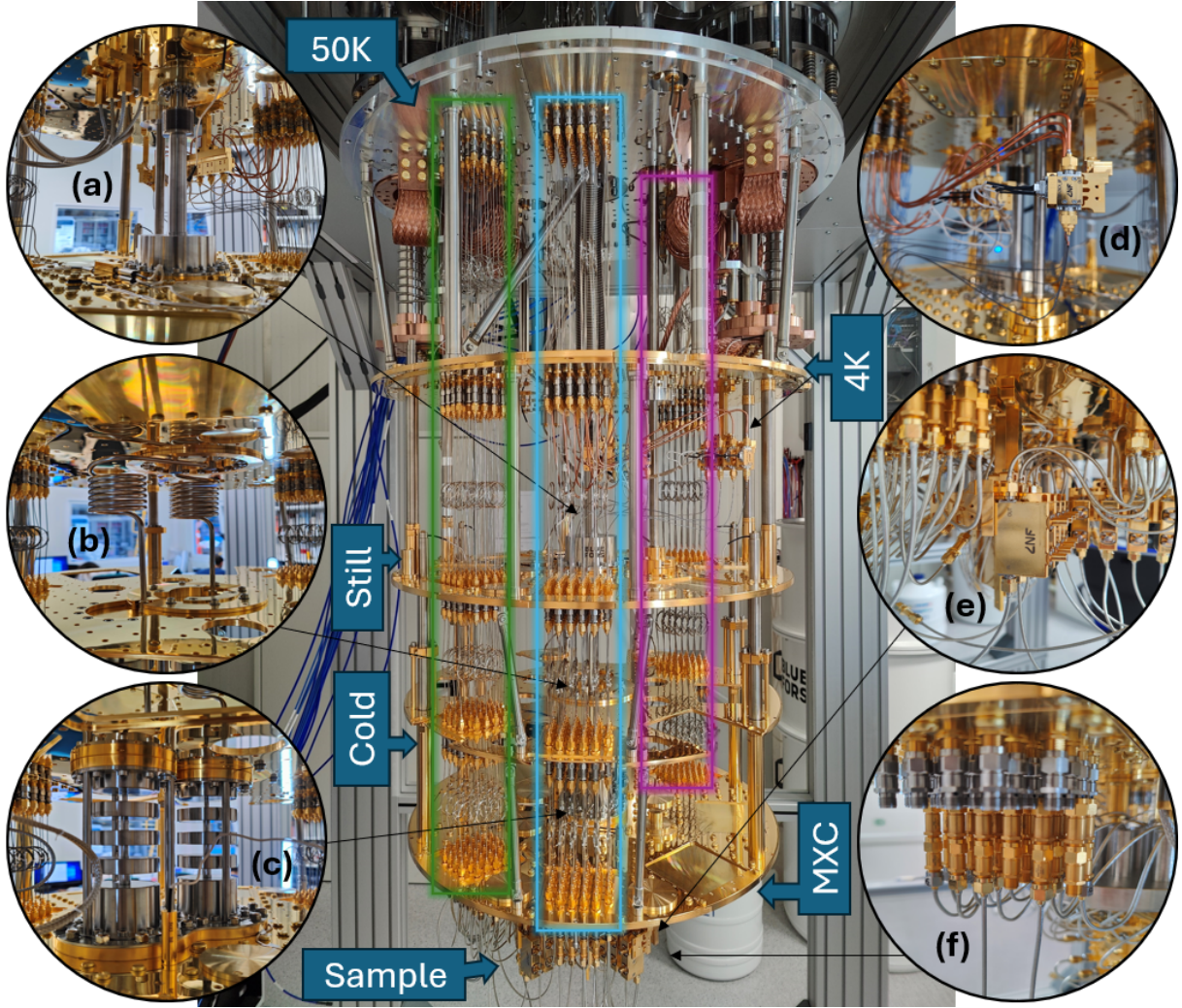


Figure 24: Cryostat stages: from the top, the 50K plate, 4K plate, Still plate at $\sim 800\text{ mK}$, Cold plate, Mixing Chamber plate and sample compartment at $\sim 10\text{ mK}$. On the left insets, the Dilution unit: Still chamber (a), Heat exchangers (b), and Mixing chamber (c). On the right insets, the amplification chain with HEMTs on 4K stage (d), isolators (e) and output line filters (f) on MXC stage. For the sideloaders setup: drive lines highlighted in the **green box**, input and output lines in the **blue box**, and flux lines in the **purple box**.

Input lines (green and blue box in Fig. 24) for both control and readout of the qubits, i.e. to provide the input signals in the feedline of readout resonators in the QPU, are made of stainless steel which provide the lowest passive heat load [45]. Furthermore they are equipped with 20 dB cryogenic attenuators on the 4K, Cold and MXC plates resulting in a -60 dB total attenuation, which adds to $\sim -10\text{ dB}$ of the lines themselves, in order to minimize black body room temperature radiation, known as Johnson-Nyquist noise [45]. Secondly they are equipped with an Eccosorb low pass filter with a 10 GHz cutoff (see Fig. 25).

Output lines (blue box in Fig. 24) are made of copper from room temperature stage to 4K plate, and of superconducting NbTi to minimize signal loss, and are properly thermalized at each plate of the cryostat through 0 dB cryogenic attenuators. Moreover these output lines are equipped with double junction isolators at the MXC stage (Fig. 24e), and with High Electron Mobility Transistor (HEMT) amplifiers (Fig. 24d) with nominal amplification of 40 dB between $4\text{ - }8\text{ GHz}$ (see Fig.25). Lastly, further amplification is obtained through three 16 dB amplifiers at RT stage.

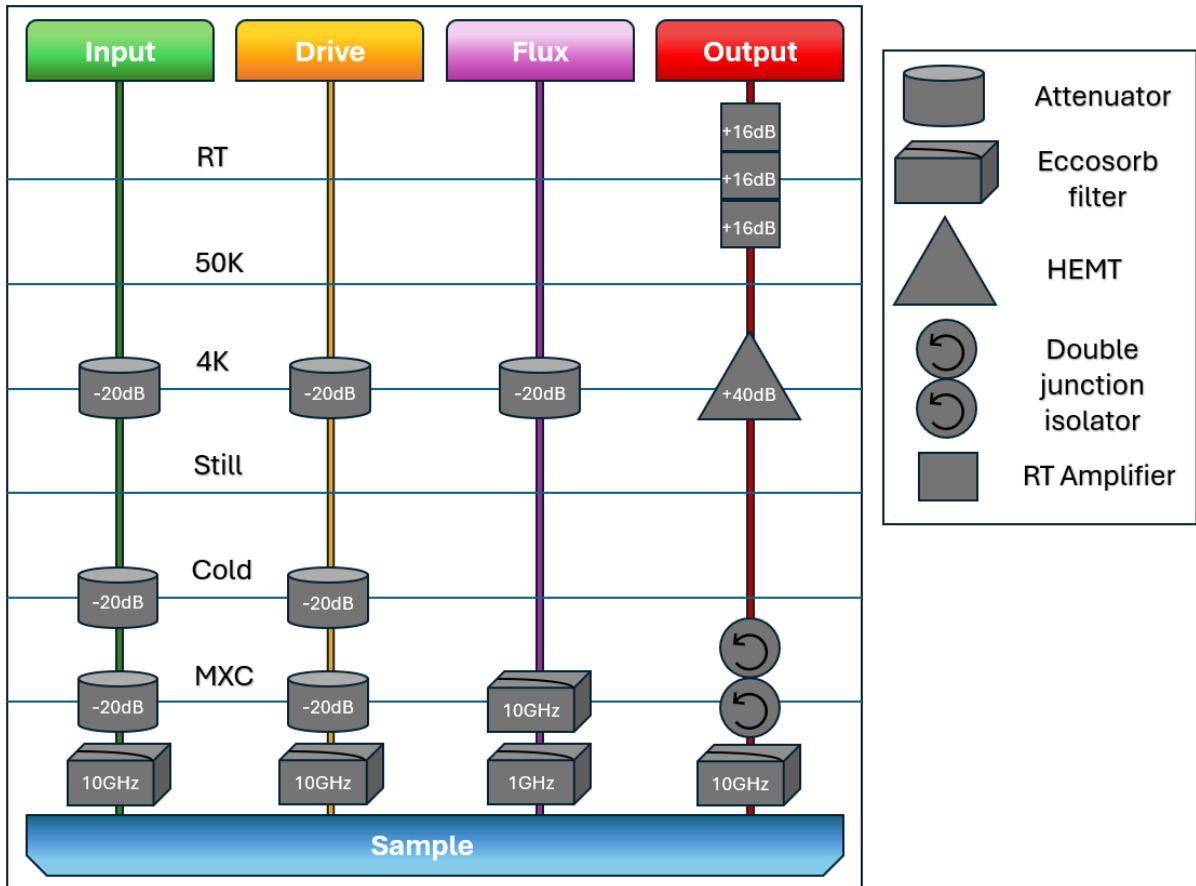


Figure 25: Cryogenic setup including feedline Input and Output lines, and qubit Drive and Flux lines, each with its own attenuators, filters and amplifiers.

Since amplifiers are noisy devices it is convenient to distribute them on a stage where the nominal temperature is higher than their noise temperature: HEMTs amplifiers feature 1.5 K noise temperature, indeed, they have been anchored at the 4K plate. The double junction isolators at the MXC attenuate backwards signals from the HEMTs to the qubit stage generated because of the finite noise temperature of about 35 dB , thus further protecting the qubits from spurious noise and signals. This adds the presence of 10 GHz Eccosorb filters, mounted at the MXC plate.

Finally flux lines (purple box in Fig. 24) allow for both DC and AC signals: these are used to generate both fast RF flux-based two-qubit gates, as well as setting the best flux-point operation for multi-qubit devices. They are made of superconducting NbTi below 4K stage, and of stainless steel above it. These lines are equipped with a -20 dB attenuator on 4K plate, which is sufficient to mitigate qubit dephasing due to current thermal noise [45], and with two low-pass filters (see Fig. 25): the first one with a 1 GHz cutoff to cut thermal noise at qubit frequency, and compatible with standard duration of two-qubit gates (\sim hundreds of MHz), then the second one for a 10 GHz cutoff aimed to avoid pulses non-linearity effects [45].

3.4 Room temperature electronics and acquisition software framework

Electronic characterization of the QPU at room temperature was performed using the **QBLOX** electronics [46][47], composed of one QBLOX Cluster and two SPI racks.

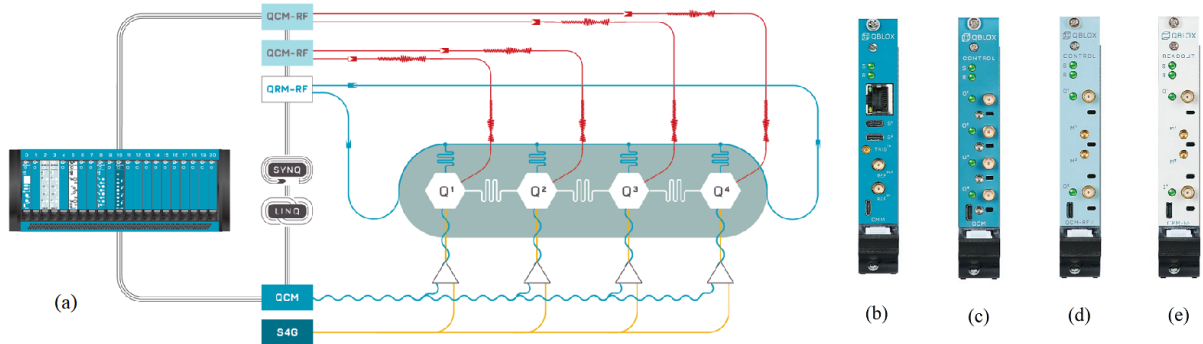


Figure 26: QBLOX instruments: (a) Schematics of Cluster and SPI Rack modules for a 4 transmons display with every dedicated line, (b) CMM, (c) QCM, (d) QCM-RF, (e) QRM-RF [46].

The QBLOX Cluster (Fig. 26a) is a scalable instrument which hosts different type of Modules, listed as follows.

- CMM module (Fig. 26b): present in every Cluster in slot 0, it allows communication from and to the host PC via Ethernet and the other modules. It is in charge of:
 - i) distributing a 10 MHz clock-reference signal among the instruments;
 - ii) controlling that the distributed reference clocks are length matched and the phase of the clocks perfectly align. The protocol used for fully deterministic and fixed timing relations, is called SYNQ, and allows to synchronize both Analog and Digital signals in the Cluster's modules down to the picoseconds level. This is essential for the implementation of quantum algorithms in the fastest way possible.
- The Qubit Control Module (QCM) (Fig. 26c) is an instrument generally dedicated to qubit control using parameterized pulses. In this work, we have used such modules to generate fast flux pulses for two-qubit gates implementation. Pulses are stored as waveform envelopes in memory and can be parameterized by changing gain and offset. Outputs channel are in the base-band regime of $0 - 400\text{ MHz}$.
- The QCM-RF (Fig. 26d) is a RF signal generator designed for the control of quantum devices through parameterized pulses. The module incorporates six multiplexed sequence processors with frequency span of 500 MHz , thus in principle allowing to control six qubits with the same output channel (Fig. 28). Nevertheless, in this work we have dedicated each channel of the QCM-RF to just one qubit at a time. Specifically, each QCM-RF is provided with two independent output channels. Each output channel has its own local oscillator to facilitate internal up-conversion [47]. The module creates signals parameterized by variables such as gain, offset, Numerically Controlled Oscillator (NCO) frequency and phase, and also by waveform envelopes stored in memory. This parameterization is controlled by the AWG paths of each sequencer. The outputs of the AWG paths are mixed with the NCO by the onboard IQ mixers, enabling operation as modulated IQ signals. The RF up-conversion stage features two additional independent IQ mixers on-board for generating the output signals in the range of $2 - 18.5\text{ GHz}$, thus compatible with typical superconducting transmon qubit frequencies in our QPU.
- The Qubit Readout Module (QRM-RF) (Fig. 26e) synthesizes and acquires signals in the range of $2 - 18.5\text{ GHz}$ using internal RF conversion stages. Each module is equipped with one output and

one input channel (Fig. 28): the former generates the excitation required to readout the qubit state through up-conversion, similarly to what occurs in QCM-RF modules, the latter is used to acquire the readout response signal of the qubit. As for the QCM-RF, it is equipped with six sequencer processors onboard. Using parameterization, each sequencer can target six readout resonators at once, allowing for multiplexed readout of multiple qubits on the same channel. The AWG paths can generate the readout pulses and the acquisition paths can process the returning readout data through Analog to Digital Converters (ADC).

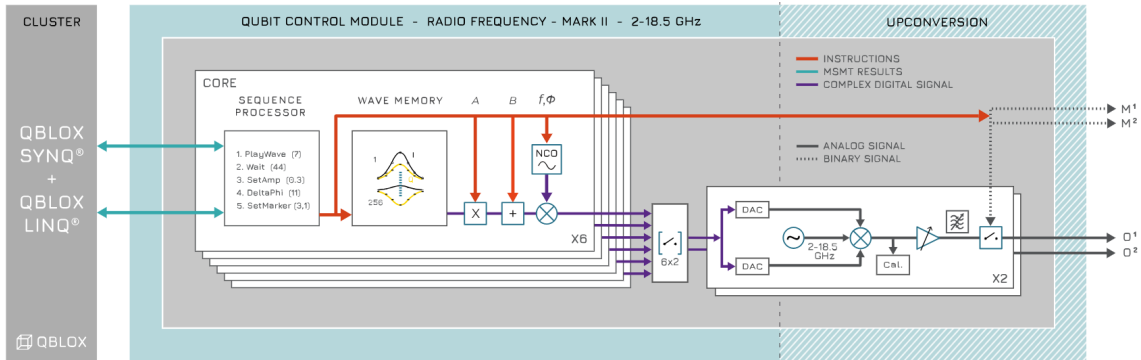


Figure 27: Block diagram of QCM-RF module showing the path from Cluster, to sequencer processors, AWG and NCO stages, until the up-conversion stage. Figure adapted from [46].

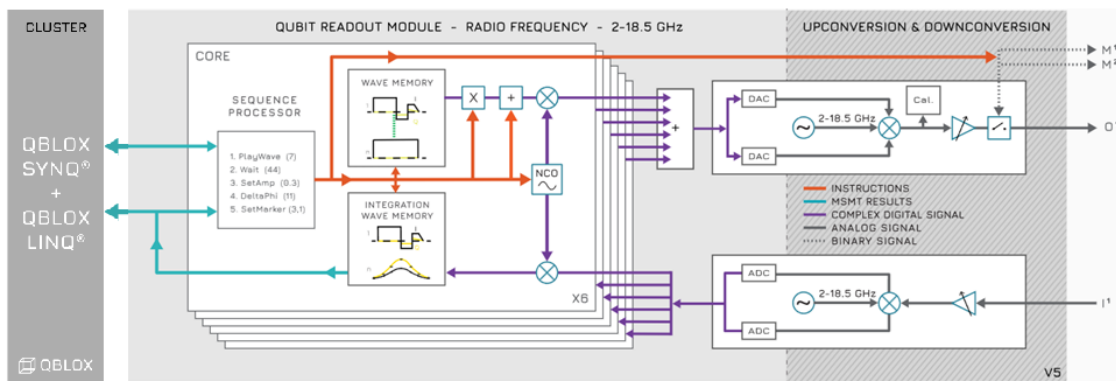


Figure 28: Block diagram of QRM-RF module showing the path from and to Cluster, with intermediate steps through sequencer processors, AWG and NCO stages, and up- and down-conversion stages. Figure adapted from [46].

Finally, in order to generate flux-based two-qubit gates, the QCM pulsed outputs are combined through bias tees at room temperature to ultra-low noise DC sources in two SPI racks. The SPI Rack (Fig. 29a) is a modular system for DC current and DC voltage source. Modules are designed to maximize output stability. Together with galvanically isolated control interface and isolated power supply, ground loops are avoided and interference is minimized. In this work, we have used either DAC current generators with 4 channels (S4g in Fig. 29c), or voltage generators with 16 channels (D5a in Fig. 29b).

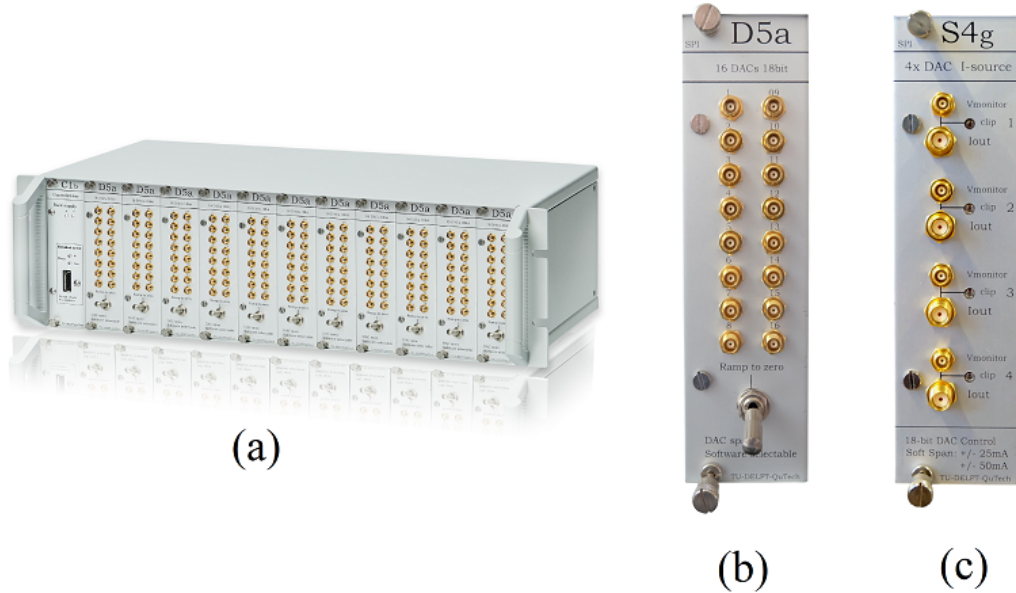


Figure 29: SPI instruments: (a) Rack, (b) D5a module, (c) S4g module.

Within this integration, we are able to detune transition frequencies of flux-tunable transmon qubits in our QPU with the lowest $1/f$ noise available.

The characterization and study of superconducting QPUs, as well as the implementation of quantum gates for algorithms, require a high-level data acquisition framework. The infrastructure used in this thesis has been built with the idea to be open. Therefore, our software codes are Python-based, and built on top of **Quantify** [48], which consists of **quantify-core** and **quantify-scheduler**.

Quantify-core enables users to quickly setup experiments while taking care of practical aspects such as data storage, live plotting of experiments, monitoring the state of instruments, and data analysis.

Quantify-scheduler is a Python module for writing quantum programs featuring a hybrid gate-pulse control model with explicit timing control allowing users to easily express complex quantum experiments.

The library that we use for diagnostic is SuperConducting Qubit Tool (SCQT) from Orange Quantum System [49], which embeds both protocols implementation and data analysis based on well-known physical models.

3.5 Single-qubit and resonator characterization

The implementation of a precise experimental protocol is crucial for the realization of high-fidelity gates. An accurate characterization of the single qubits is needed in order to be able to define the optimal control and readout signal features.

Resonator spectroscopy

In order to characterize the qubit, it is first necessary to characterize the readout resonator coupled with it. The first measurement is an heterodyne spectroscopy in order to identify its resonance frequency. Here, a single-tone signal in the range of the nominal resonator frequency is sent through the feedline. When this signal resonates with the readout resonator, a typical Lorentian dip in the transmission S_{21} stands out among the background due to the photons absorption (Fig. 30a). Once the frequencies of the resonators have been identified, a sweep in power of the feedline input signal is performed around the resonator frequency, in order to estimate the power of the readout tone which allows to enter in the single-photon (or low-photon) regime, fundamental for performing quantum non-demolition and dispersive readout of the qubit state (Sec. 1.4.2). As shown in Fig. 30b, for high values of the input power, the qubit is completely saturated and the input signal only resonates with the frequency of the isolated readout resonator (bare state). The dispersive regime is recovered by decreasing the input signal, i.e. pointing towards the single-photon regime [52].

Last characterization protocol is a flux spectroscopy (Fig. 30c), in which a readout resonator spectroscopy is performed as a function of a current applied to the flux line (i.e. flux treading the transmon SQUID), in order to observe the flux modulation of the resonator and to identify its periodicity and the current value at which the sweetspots occur.

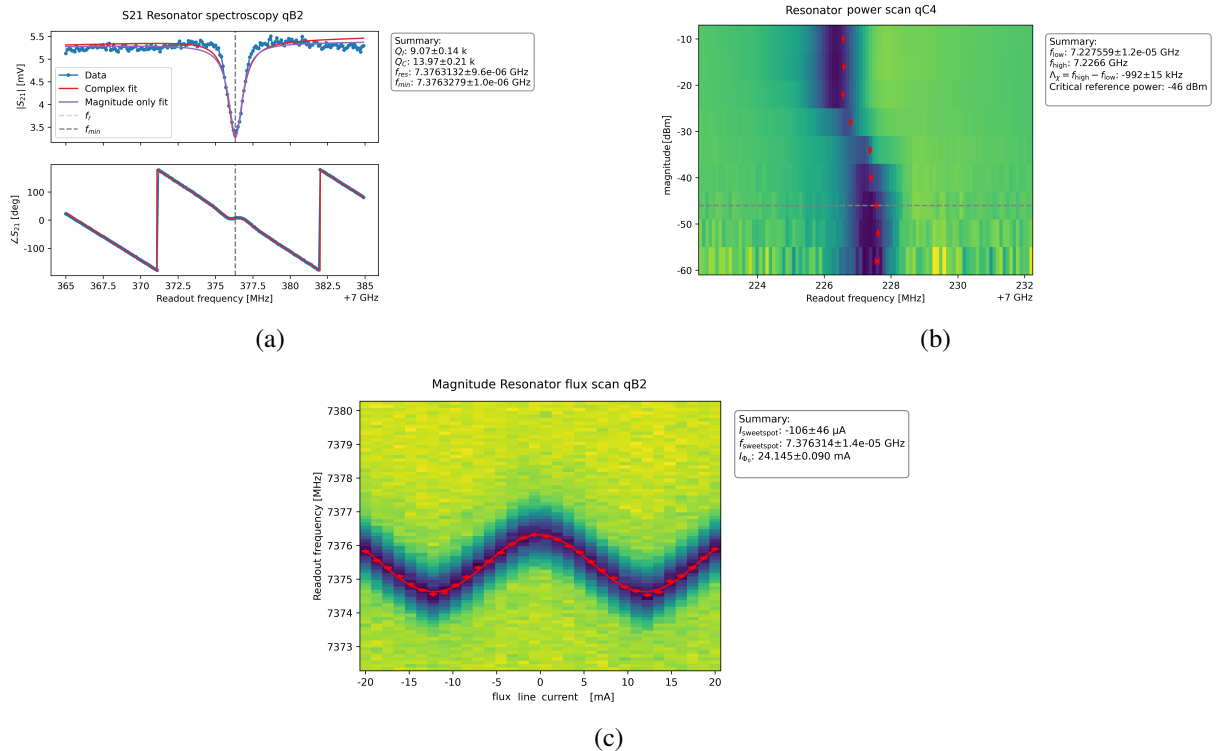


Figure 30: In **(a)** Resonator spectroscopy of qB2 as a function of transmitted and reflected signal; in **(b)** Power spectroscopy of qC4 showing the Δ_χ shift from the resonator bare state and low-photon regime; in **(c)** flux spectroscopy of qB2 resonator as a function of power.

Qubit spectroscopy

In order to provide a measurement of the qubit frequency, a two-tone spectroscopy is performed [52]. The two-tone signal is composed of an RF signal sent through the feedline, which is close to the resonance frequency of the readout resonator in the low-photon regime, and an RF signal that sweeps in frequency, sent through the dedicated qubit drive line, which excites the qubit (drive tone). The idea is to continuously send a weak microwave signal to the cavity at the low power, in order to leave the qubit in its ground state. Once the control signal resonates with the qubit transition frequency, the qubit passes to the excited state causing a shift in the cavity frequency. Thus, since the fixed input signal is no longer resonant with the cavity, the transmitted power S_{21} changes as depicted in Fig. 31a. Moreover, performing the same experiment as a function of the amplitude of the control signal, one can also experimentally observe higher orders energy transitions of the qubit. Given the negative anharmonicity of the transmon (Sec. 1.3), energy peaks can be measured at a frequency lower than the $|0\rangle \rightarrow |1\rangle$ transition frequency. For example, one can measure both the assisted two-photons $|0\rangle \rightarrow |2\rangle$ transition, or even the $|1\rangle \rightarrow |2\rangle$ transition for sufficiently high power (Fig. 31a). Finally, a flux spectroscopy of the qubit is also performed, in order to estimate the qubit flux arc, fundamental for the estimation of the qubit Josephson energy, the charging energy, the flux-tunable transmon asymmetry and the flux sweetspot (Fig. 31b).

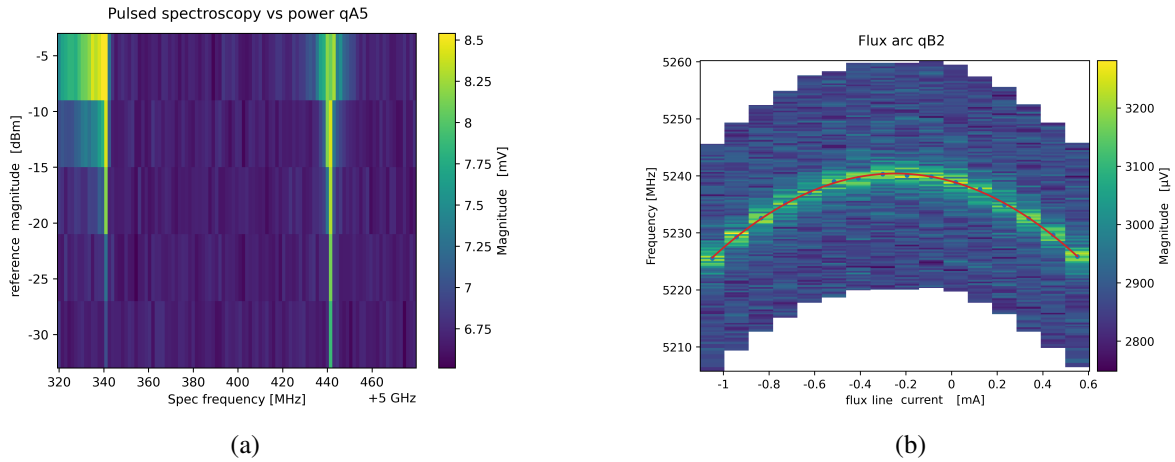


Figure 31: Qubit power spectroscopy of qA5 in (a), showing the first order transition frequency $|0\rangle \rightarrow |1\rangle$ at higher frequency than the assisted two-photon transition $|0\rangle \rightarrow |2\rangle$, and qB2 flux arc spectroscopy in (b) as a function of magnitude.

3.6 Control pulses optimization and hardware implementation

Time-domain measurements are at the core of the qubit coherence and fidelity benchmarking characterization. Here we describe a step-by-step sequence of experimental protocols to perform coherence and fidelity benchmarking experiments.

Rabi oscillation and Chevron plots

Rabi oscillations measurements provide the estimation of the π -pulse amplitude (Fig. 32a), a fundamental quantity for qubit gates implementation [50]. The π -pulse is a drive signal on-resonance with the qubit frequency with an amplitude able to bring the qubit from the ground state $|0\rangle$ to the first excited state $|1\rangle$. X , Y and Z gates, are in fact π -pulses, that allow to perform a 180° rotation of Bloch vector, with the only difference of a relative phase in the drive pulse.

When a qubit, initially in its ground state, is driven by a harmonically oscillating weak field with a

frequency ω_d close to its energy splitting ω_q (up to a factor of \hbar), its probability to be found in the excited state at a later time t is given by:

$$P = \frac{\omega_d^2}{\Omega_d^2 + \Delta^2} \frac{1 - \cos(\Omega_R t)}{2}, \quad (54)$$

where $\Delta = |\omega_d - \omega_q|$ is the detuning between the drive tone frequency and the qubit frequency, and $\Omega_R = \frac{\sqrt{\Delta^2 + \omega_d^2}}{2}$ is the Rabi frequency [50].

The operative procedure to measure the Rabi oscillations consists in sending a drive signal followed by a readout pulse (Fig.32b). The protocol can be performed both by fixing the power drive tone (i.e. the amplitude) while its duration, called *plateau*, is variable, or vice versa. In this thesis we have changed the amplitude of the drive tone from $-1V$ to $1V$, i.e. the maximum range of voltage that we can generate with the QCM-RF (Sec. 3.4). An example of the pulse chain in the two extremes of this range is shown in Fig. 32c and 32d.

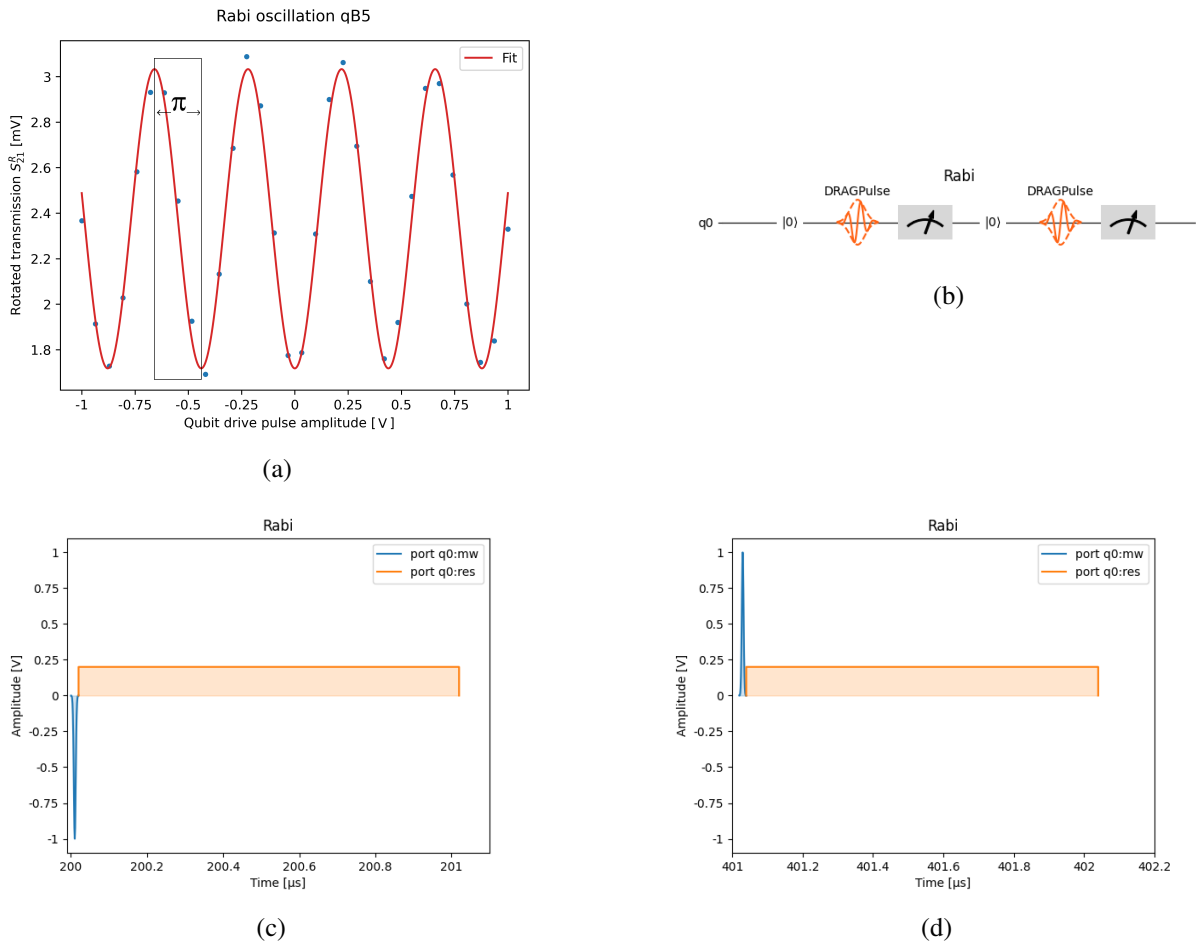


Figure 32: In (a) Rabi oscillation measurement of qB5 showing in the highlighted box the π -pulse, which corresponds to the half period; in (b) the Rabi protocol pulse sequence: the qubit is prepared in its ground state, then a drive pulse (see following Sec.3.6) is sent to it, followed by qubit state measurement. In (c) and (d) Drive pulse amplitude as a function of time showing the first and last pulse of the amplitude screening performed during the Rabi protocol (blue waveform) followed by resonator readout pulse (orange waveform).

In order to define the π -pulse, Eq. (54) states that the transition probability to the excited state is maximized when the drive tone is on resonance with the qubit frequency (Fig. 33). Therefore, the first calibration procedure for control pulses frequency involves what is known as Ramsey interferometry.

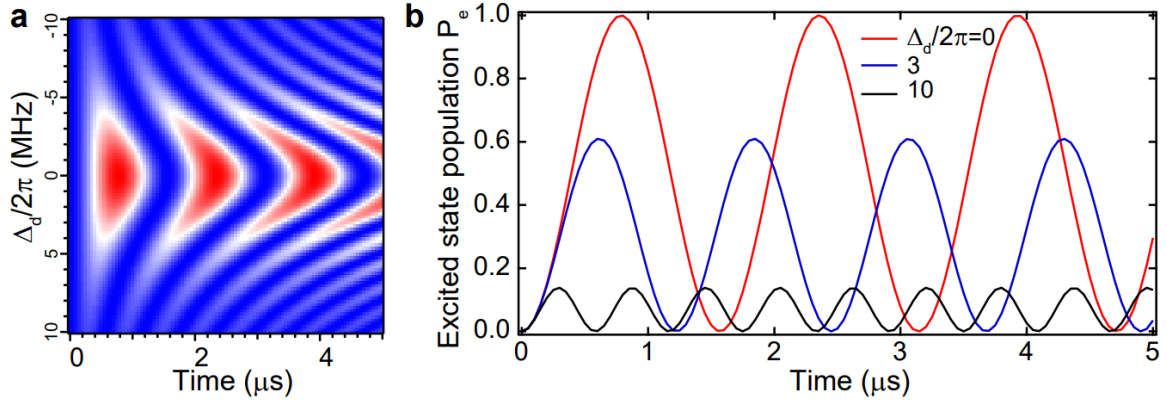


Figure 33: In (a) the 2D Chevron plot of the excited state population P versus time for different detunings Δ , and in (b) three cuts from the Chevron plot at different detuning values [52].

Ramsey interferometry

Ramsey interferometry protocol consists in preparing the qubit on the Bloch sphere equator applying a $X_{\pi/2}$ -pulse, i.e. a pulse whose amplitude is half of the π -pulse, measured through Rabi oscillations experiments (Fig. 34a). Then the qubit is left free to evolve spontaneously for a time τ . Subsequently, a second $X_{\pi/2}$ -pulse projects the Bloch vector back to the z -axis before inferring the qubit state (see Fig. 35). In presence of detuning $\delta\omega = |\omega_d - \omega_q|$ between the drive and qubit frequencies, the Bloch vector will start precess around the z -axis at a rate $\delta\omega$ [7]. As result, if the drive signal is off-resonance with

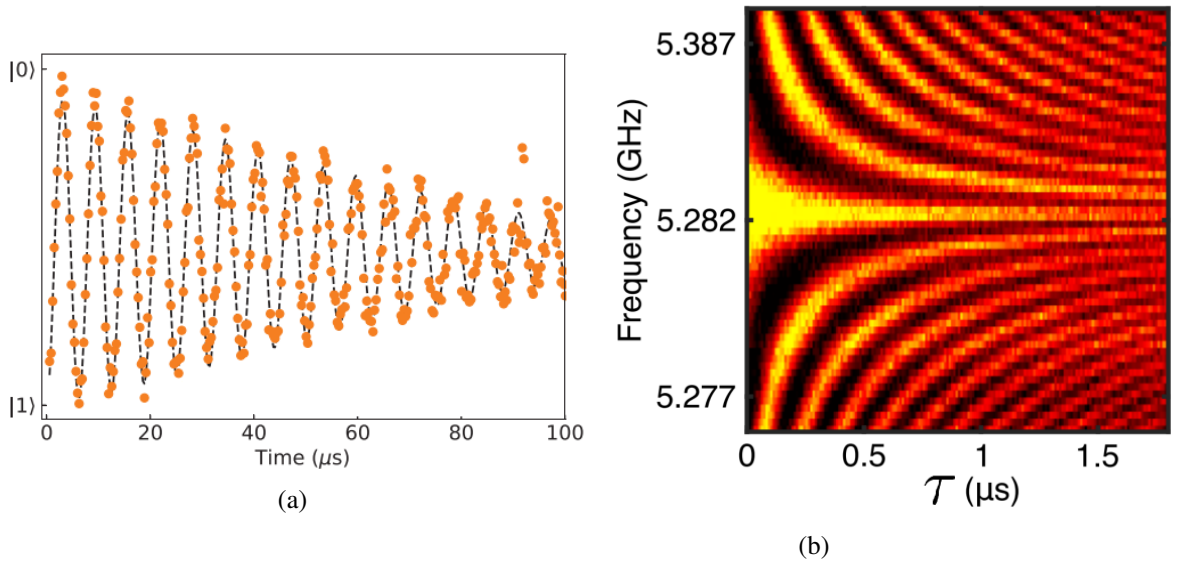


Figure 34: Ramsey Interferometry oscillation as function of time delay in (a) [7] and Ramsey fringes as a function of the qubit drive frequency and time delay τ between the two $\pi/2$ -pulses in (b) [54].

the qubit frequency, damped oscillations with an exponential decay $\propto \cos(\delta\omega t)e^{-\Gamma_2 t}$ with a characteristic time T_2^* arise (Fig. 34a). Repeatedly changing the drive tone and measuring Ramsey oscillations allow to erase these oscillations until the output exhibits only an exponential decay feature. The on-resonance drive frequency is then found as the center of the Ramsey fringes plot (Fig. 34b).

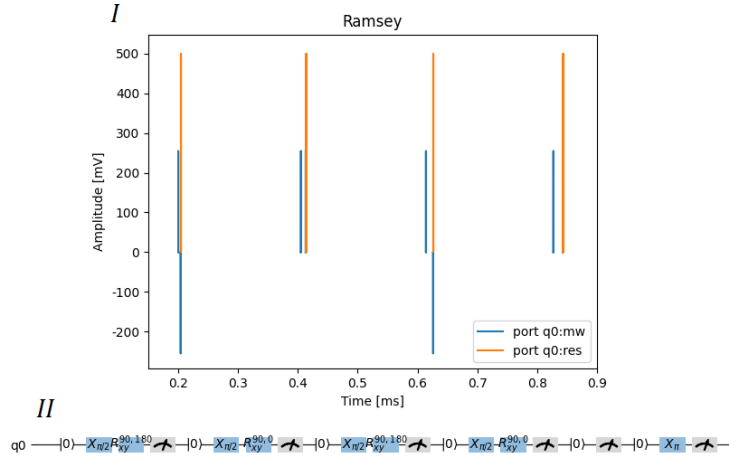


Figure 35: Pulses amplitude of qubit drive (blu data) and readout resonator (orange data) as a function of time delay (*I*), and sequence pulse of qubit drive (*II*).

Drive pulse shape optimization: DRAG scheme

Finally, for weakly anharmonic qubits, such as the transmon characterized by an anharmonicity (Eq. (11)) of the order of 200 to 300 MHz, drive pulses can have spectral contents that lead to non-zero overlaps with the higher orders energy levels. This may induce leakage errors, which take the qubit out of the computational subspace, and phase errors [7]. The latter occurs because of the repulsion between $|1\rangle$ and $|2\rangle$ levels due to the presence of the drive pulse, resulting in a change of $\omega_q^{0 \rightarrow 1}$ and leading to a relative phase accumulation between those levels.

The **DRAG scheme** (Derivative Reduction by Adiabatic Gate) is able to mitigate these two deleterious effects by applying an extra signal in the out-of-phase component of the control pulses (Eq. (24)) [7]. This operation modifies the waveform envelope $s(t)$ in Eq. (26) according to:

$$s(t) \rightarrow s'(t) = \begin{cases} s(t) & \text{on } I \\ \lambda \frac{\dot{s}(t)}{\alpha} & \text{on } Q \end{cases}, \quad (55)$$

where λ is a dimensionless scaling parameter and α is the anharmonicity (Fig. 36). For $\lambda = 0$ no DRAG correction is applied. The theoretically optimal choice for reducing phase error is $\lambda = 0.5$. Meanwhile, for reducing leakage error, it is $\lambda = 1$ [55][56]. Therefore a trade-off value is needed. However, it is possible to reduce both errors simultaneously by introducing a frequency detuning parameter δf to the waveform ($\delta f = 0$ corresponds to standard qubit frequency):

$$s'_{\delta f}(t) = s'(t)e^{i2\pi\delta f t}, \quad (56)$$

and choosing λ to minimize leakage errors [7].

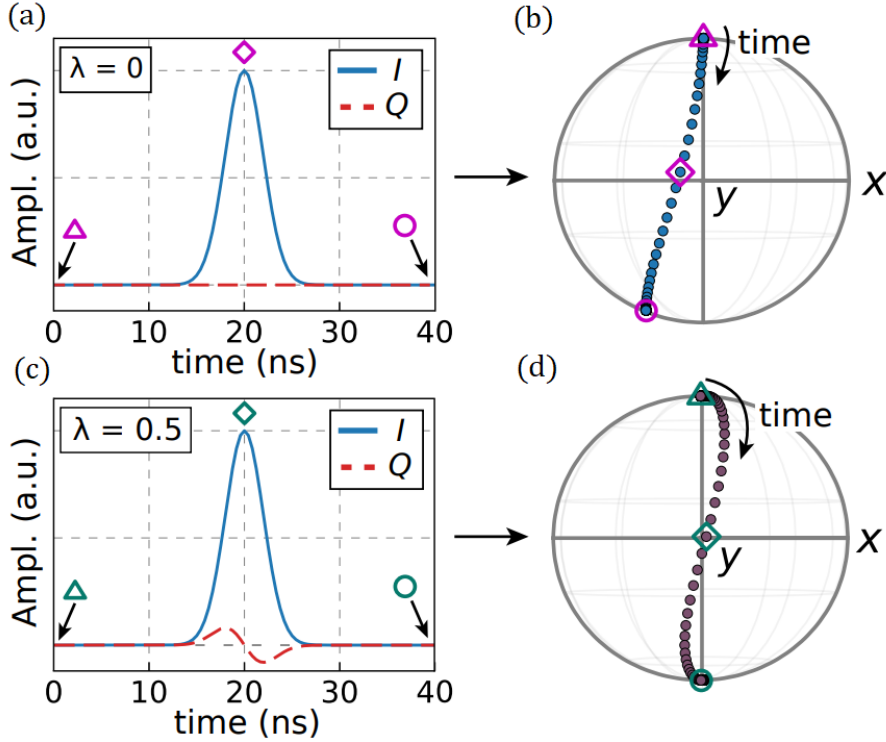


Figure 36: Comparison between a X_π pulse waveform without *DRAG* modulation ($\lambda = 0$) (a) with its resulting effect on a qubit initialized in the $|0\rangle$ state (b), and a X_π pulse waveform with *DRAG* modulation ($\lambda = 0.5$) (c) with its resulting effect (d). The dephasing error is visible as a deviation from the $|1\rangle$ state after the pulse in (b), then canceled after *DRAG* scheme in (d).

3.7 Detecting syndromes for control optimization

Rabi and Ramsey experiments are adequate tune-ups for most basic single-qubit experiments. However, higher quality rotations are often desirable for applications where a high fidelity is needed, as for algorithms. The *AllXY* sequence tests the result of all combinations of one or two single-qubit gates being sensitive to a variety of error syndromes [57]. During the protocol, 21 different pulse combination, belonging to the “Clifford set” of quantum gates [58], are performed on a qubit producing rotations around the x - and y -axes by an angle of $\pi/2$ or π before measuring its state. Since each pulse combination is sensitive to various errors to varying degrees, different errors will then have a distinct fingerprint in the deviation from the ideal response, providing a quick way of diagnosing problems [57].

The first tier of ordering, as seen in Tab. 2, is determined by the place that the qubit should reach on the Bloch sphere at the end of the sequence. Pulses that end up on the north or south pole are often relatively insensitive to errors, and so the most valuable information is primarily given by the pulses ending on the equator, being particularly sensitive to over rotations. This is because the expected value $\langle z \rangle$ is proportional to the cosine of the angle θ by which the Bloch vector has been rotated (e.g. $X(\theta)$).

Ideal $\langle z \rangle$	First pulse	Second pulse	Power dependence	Detuning dependence
1	ld	ld	1	1
1	$X(\pi)$	$X(\pi)$	$1 - 8\epsilon^2 + \mathcal{O}(\epsilon^4)$	$1 - \frac{\pi^2\epsilon^4}{32} + \mathcal{O}(\epsilon^6)$
1	$Y(\pi)$	$Y(\pi)$	$1 - 8\epsilon^2 + \mathcal{O}(\epsilon^4)$	$1 - \frac{\pi^2\epsilon^4}{32} + \mathcal{O}(\epsilon^6)$
1	$X(\pi)$	$Y(\pi)$	$1 - 4\epsilon^2 + \mathcal{O}(\epsilon^4)$	$1 - \epsilon^2 + \mathcal{O}(\epsilon^3)$
1	$Y(\pi)$	$X(\pi)$	$1 - 4\epsilon^2 + \mathcal{O}(\epsilon^4)$	$1 - \epsilon^2 + \mathcal{O}(\epsilon^3)$
0	$X(\pi/2)$	ld	$-\epsilon + \mathcal{O}(\epsilon^3)$	$(1 - \frac{\pi}{2})\epsilon^2 - \mathcal{O}(\epsilon^4)$
0	$Y(\pi/2)$	ld	$-\epsilon + \mathcal{O}(\epsilon^3)$	$(1 - \frac{\pi}{2})\epsilon^2 - \mathcal{O}(\epsilon^4)$
0	$X(\pi/2)$	$Y(\pi/2)$	$\epsilon^2 - \mathcal{O}(\epsilon^4)$	$-2\epsilon + \mathcal{O}(\epsilon^3)$
0	$Y(\pi/2)$	$X(\pi/2)$	$\epsilon^2 - \mathcal{O}(\epsilon^4)$	$2\epsilon - \mathcal{O}(\epsilon^3)$
0	$X(\pi/2)$	$Y(\pi)$	$\epsilon - \mathcal{O}(\epsilon^3)$	$-\epsilon - \mathcal{O}(\epsilon^2)$
0	$Y(\pi/2)$	$X(\pi)$	$\epsilon - \mathcal{O}(\epsilon^3)$	$-\epsilon - \mathcal{O}(\epsilon^2)$
0	$X(\pi)$	$Y(\pi/2)$	$\epsilon - \mathcal{O}(\epsilon^3)$	$-\epsilon - \mathcal{O}(\epsilon^2)$
0	$Y(\pi)$	$X(\pi/2)$	$\epsilon - \mathcal{O}(\epsilon^3)$	$-\epsilon - \mathcal{O}(\epsilon^2)$
0	$X(\pi/2)$	$X(\pi)$	$3\epsilon - \mathcal{O}(\epsilon^3)$	$\frac{3\pi\epsilon^2}{8} + \mathcal{O}(\epsilon^4)$
0	$X(\pi)$	$X(\pi/2)$	$3\epsilon - \mathcal{O}(\epsilon^3)$	$\frac{3\pi\epsilon^2}{8} + \mathcal{O}(\epsilon^4)$
0	$Y(\pi/2)$	$Y(\pi)$	$3\epsilon - \mathcal{O}(\epsilon^3)$	$\frac{3\pi\epsilon^2}{8} + \mathcal{O}(\epsilon^4)$
0	$Y(\pi)$	$Y(\pi/2)$	$3\epsilon - \mathcal{O}(\epsilon^3)$	$\frac{3\pi\epsilon^2}{8} + \mathcal{O}(\epsilon^4)$
-1	$X(\pi)$	ld	$-1 + 2\epsilon^2 + \mathcal{O}(\epsilon^4)$	$-1 + \frac{\epsilon^2}{2} + \mathcal{O}(\epsilon^4)$
-1	$Y(\pi)$	ld	$-1 + 2\epsilon^2 + \mathcal{O}(\epsilon^4)$	$-1 + \frac{\epsilon^2}{2} + \mathcal{O}(\epsilon^4)$
-1	$X(\pi/2)$	$X(\pi/2)$	$-1 + 2\epsilon^2 + \mathcal{O}(\epsilon^4)$	$-1 + 2\epsilon^2 + \mathcal{O}(\epsilon^4)$
-1	$Y(\pi/2)$	$Y(\pi/2)$	$-1 + 2\epsilon^2 + \mathcal{O}(\epsilon^4)$	$-1 + 2\epsilon^2 + \mathcal{O}(\epsilon^4)$

Table 2: $AIXY$ sequences. The first and second pulse are listed and ordered according to where the qubit should ideally end up: north pole, i.e. ground state (Ideal $\langle z \rangle = 1$), equator (Ideal $\langle z \rangle = 0$), or south pole, i.e. excited state (Ideal $\langle z \rangle = -1$) of the Bloch sphere. The analytically calculated leading-order power and detuning error dependence of the qubit z projection are shown [57].

By ordering the pulses according to this sensitivity, too much or too little power of the control signal yields a characteristic “step” pattern, shown in Fig. 37a. The remaining order is given by X and Y rotations in the first column of Tab. 2, which is helpful because the two axes feel the opposite effect of detuning, giving a characteristic “zig-zag” pattern, shown in Fig. 37b. Finally, one can also observe phase errors, mainly due the IQ mixer imperfections, such as amplitude imbalance and skewness. In this case, in Ref. [57] was introduced an X scale factor used to compensate for phase errors due to the presence of higher excited-state levels, shown in Fig. 37c. In this thesis, we did not focus on this last syndrome, but we exploited the $AIXY$ protocol to identify which parameters of the control pulses were to be corrected. For frequency detuning syndromes, we have iteratively run Ramsey experiments.

Frequency detuning correction through Ramsey experiments, amplitude correction through Flipping protocol and *DRAG* coefficient parameter optimization through Motzoi experiment are typically run iteratively, and checked by measuring the *AIIXY* response of the qubit. This allows to optimize the control pulses before performing coherence and fidelity benchmarking. In the following, we will report on the fundamental experimental protocols for measurement of coherence times, like relaxation, Ramsey and Echo times.

3.8 Coherence times

As introduced in Sec. 2.1, coherence times give information on qubit behavior in presence of noise. The T_1 measurement protocol (Fig. 40) consists in the preparation of the qubit in its excited state using an X_π -pulse, and then leave it to spontaneously decay to the ground state for a variable time τ , after which the qubit state is measured (see Fig. 40a). A single measurement will project the quantum state into either state $|0\rangle$ or state $|1\rangle$, with probabilities that correspond to the qubit polarization. To make an estimate of this polarization by statistics, one needs to identically prepare the qubit in $|0\rangle$ and $|1\rangle$, and repeat the experiment many times [7][52]. The expected behavior is an exponential decay, whose time constant identifies the relaxation time.

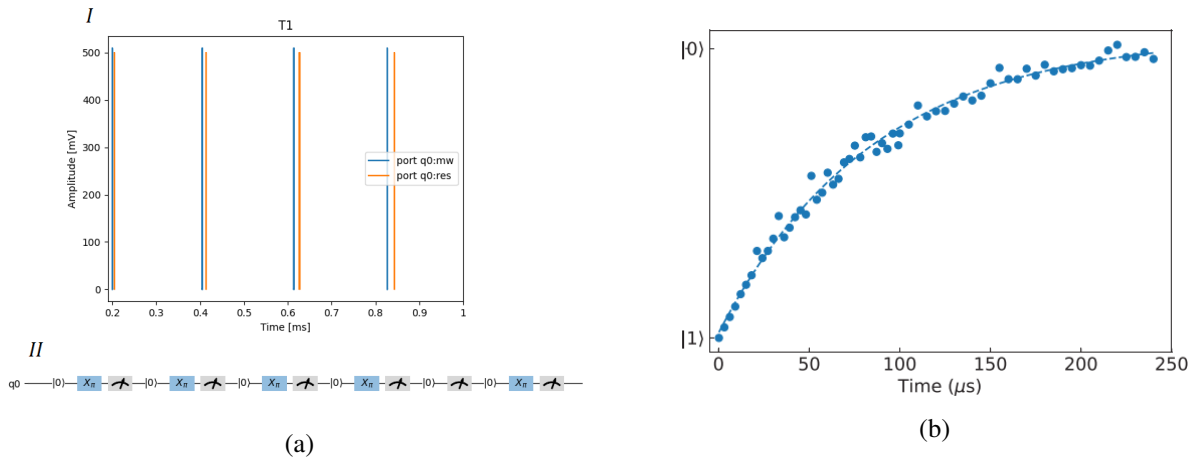


Figure 40: In (a) sequence pulses of T_1 measurement protocol: pulses amplitude of qubit drive (blu data) and readout resonator (orange data) as a function of time delay (*I*), and sequence pulse of qubit drive (*II*). In (b) exponential energy relaxation as function of time [7].

For what concerns the measurement of T_2 coherence time, in this thesis we have used two protocols: the **Ramsey** and **Spin-Echo** protocols. For the former, in contrast with operative procedure for the optimization in Sec. 3.6, the carrier frequency of the drive pulse is intentionally detuned from the qubit frequency by $\delta\omega$ for a simpler analysis in terms of fitting function, $\propto \cos(\delta\omega t)e^{-\Gamma_2 t}$ (see Fig. 34a). The exponential decay time of the Ramsey oscillation is also labeled as T_2^* , which is sensitive to inhomogeneous broadening. Which means, it is highly sensitive to quasi-static, low-frequency fluctuations that are constant within one experimental trial, but vary from trial to trial, e.g. due to $1/f$ -type noise [7].

This value for the coherence time typically differs from the one measured through the Hahn Spin Echo protocol, which is less sensitive to quasi-static noise. By placing a X_π -pulse at the center of a Ramsey interferometry experiment (see Fig. 41a), the quasi-static contributions to dephasing can be “refocused” leaving an estimate of T_{2E} (Fig. 41b), that is less sensitive to inhomogeneous broadening mechanisms. The pulses are generally chosen to be resonant with the qubit transition for a Hahn echo, since any frequency detuning would be nominally refocused anyway.

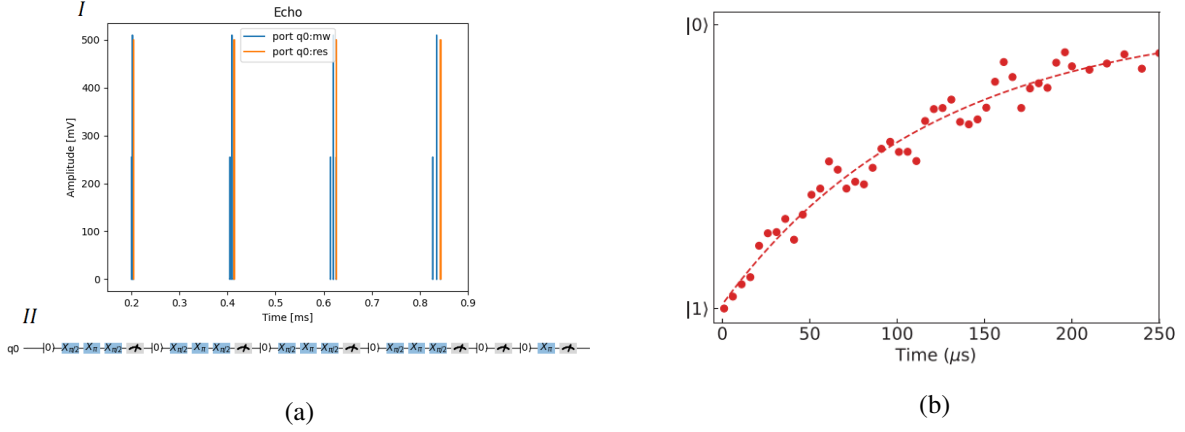


Figure 41: In (a) sequence pulses of T_{2E} measurement protocol: pulses amplitude of qubit drive (blue data) and readout resonator (orange data) as a function of time delay (I), and sequence pulse of qubit drive (II). In (b) exponential trend as function of time in Spin Echo protocol [7].

3.9 Randomized Benchmarking

The Randomized Benchmarking protocol performs an average gate fidelity evaluation which is robust to SPAM errors, allowing to gain an overall information on the hardware gate implementation [67]. As introduced in Sec. 2.3, RB protocol consists in applying a random sequence of N gate, sorted from the Clifford gate set $\{\mathcal{C}_i\}$ to the qubit, followed by one last inverse Clifford gate before measuring its state. Ideally the measured state should be identical to the initial state, i.e. ground state $|0\rangle$, but the actual measured state will be different due to the error induced by the gate implementation. The number of gates in a sequence is chosen to be $N_{Cl} = [1, 2, 4, 8, 16, 32, 64, 128, 256, 512, \dots]$ in order to easily obtain an exponential decay trend (Fig. 42). In order to perform repeated measurements with different gate combinations, for each sequence N_{Cl} , random gates are sorted through a certain number of seeds, i.e. random number generators. Therefore, for each sequence the survival probability $F_{|0\rangle}$, i.e. the average sequence gate fidelity, is measured. After the measurement, the p parameter is fitted using the model

$$F_{|0\rangle} = Ap^{N_{Cl}} + B. \quad (57)$$

Here A and B parameters give information about SPAM errors (further details in Appendix B). Then the gate fidelity over all the Clifford sequences is given by [67]:

$$F_{Cl} = 1 - \frac{d-1}{d}(1-p). \quad (58)$$

Lastly, it is possible to get an estimation of average gate fidelity per applied gate as [68]:

$$F_{avg.gate} = (F_{Cl})^{\frac{1}{1.875}}, \quad (59)$$

where the exponent of the root-square is related to the decomposition of each gate into the standard minimal sequence of π - and $\pi/2$ -pulses around the x and y axes, requiring an average $\langle N_P \rangle = 1.875$ pulses per Clifford.

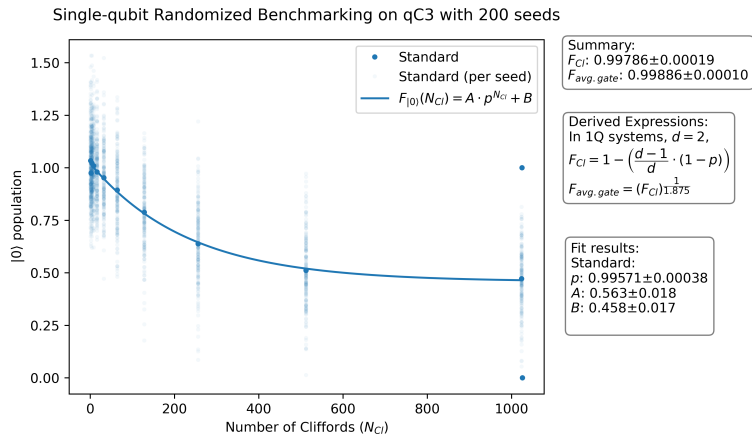


Figure 42: Single-qubit Randomized Benchmarking protocol on qC3 with 200 seeds per sequence.

4 Final results and discussion

In this chapter we will report the experimental results on the analysis of the Contralto-D QPU. In order to establish the quality of processor performance, for each qubit we have performed the calibration protocols described in Sec. 3 and then an evaluation of coherence times and gate fidelity. The experimental data have been acquired and analyzed through the hardware and software set-up described in Sec. 3.4. We here report a detailed discussion of the experimental procedure, as well as on the obtained results on one qubit, namely **B4**. The same approach has been used to characterize the other qubits of the QPU, for which we report a comparative analysis of their parameters.

4.1 Single-qubit characterization of qubit B4: a case study

To give an example of the experimental steps we have performed on each qubit to evaluate their performances in terms of single-qubit gate fidelity and coherence, in the following we report the complete characterization of qubit **B4**.

B4 resonator characterization

As discussed in Sec. 3.5, the first protocol concerns the characterization of the readout resonator coupled with the qubit.

The first step was to identify the resonance frequency of the resonator through heterodyne spectroscopy. Therefore, a single-tone signal in the range of the nominal resonator frequency was sent through the feedline. When this signal resonates with the readout resonator, a typical Lorentian dip in the transmission S_{21} stands out against the background, at the resonance frequency of the resonator, due to photons absorption. The nominal frequency reported by QuantWare was $f_{res}^* = 7.8 GHz$, while the measured resonance frequency was found to be $f_{res} = 7.579 \pm 1 * 10^{-3} GHz$ (Fig. 43).

Once the resonance frequency was identified, in order to estimate the readout tone power required to switch from the bare state of the resonator to the dressed state in low-photon regime, a sweep in power of the feedline input signal was performed around f_{res} . As shown in Fig. 44a, for a starting attenuation of $-20 dB$ on the input signal, the readout resonator is already transitioning to the low-photons regime, where we can recover $f_{low} = 7.579 \pm 1.0 * 10^{-3} GHz$, at a reference magnitude power of $-50 dB$.

Here, the frequency shift respect to that of the bare state was $\chi_{low} = -1.12 \pm 0.05 MHz$.

The last characterization test was the readout resonator flux spectroscopy which was performed in order to observe the flux modulation of the resonator and to identify the current value at which sweetspots occur. In this protocol, a sweep in frequency of the feedline input signal was performed while tuning the qubit with a current sent through the flux line, and so changing the flux threading the transmon's SQUID. As shown in Fig. 44b, the resonator sweetspot has been identified at a frequency

$f_{sweetspot} = 7.579 \pm 1.0 * 10^{-3} GHz$, which corresponds to a bias current value $I_{sweetspot} = -8.05 \pm 0.13 mA$. Moreover the modulation featured a period $I_{period} = 25.1 \pm 0.2 mA$.

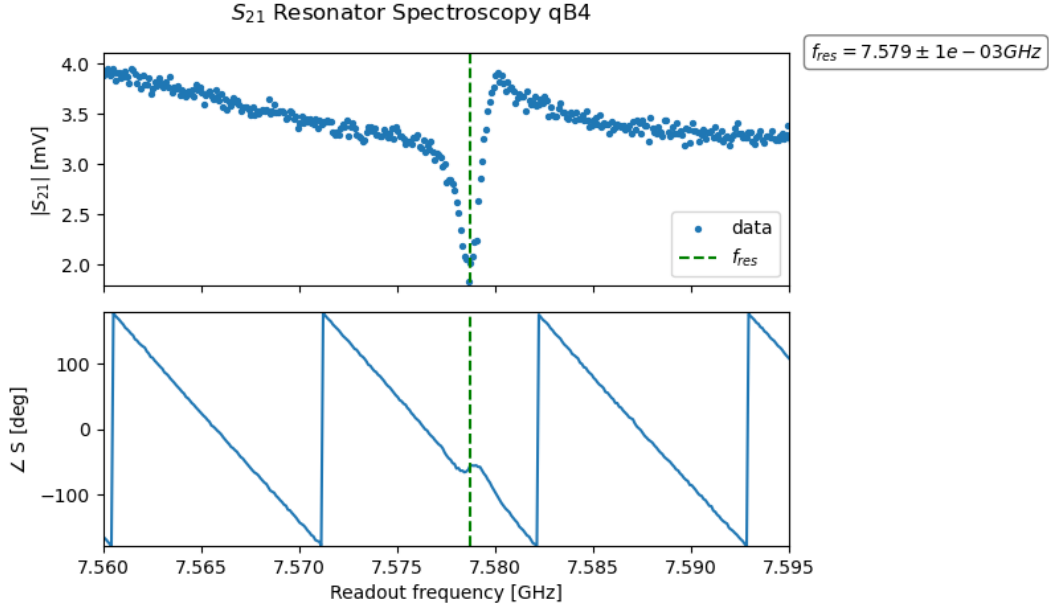


Figure 43: Qubit B4 resonator spectroscopy: magnitude S_{21} vs frequency in top panel, phase $\angle S$ vs frequency in bottom panel.

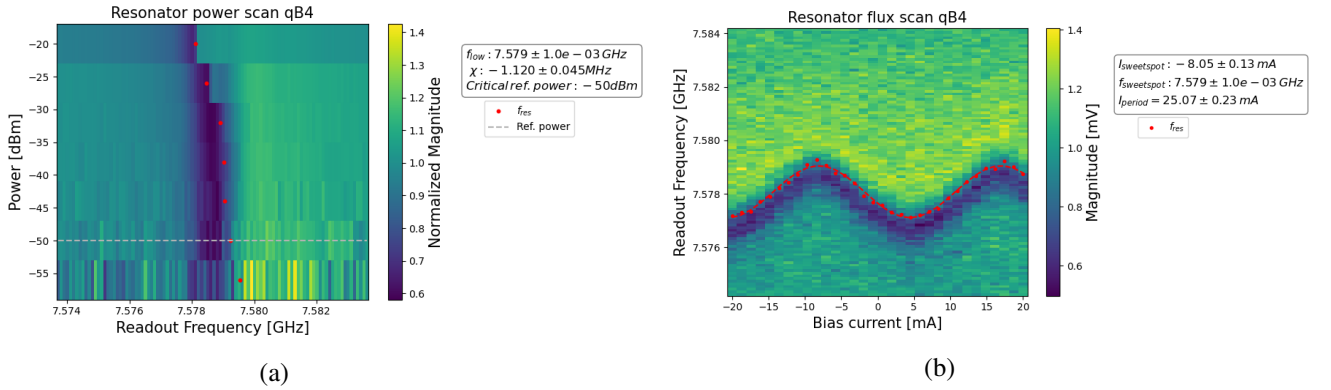


Figure 44: Qubit B4 resonator spectroscopy: in (a) power spectroscopy, in (b) flux spectroscopy.

B4 qubit characterization

The next step was the qubit characterization, starting from the measurement of the resonance frequency, followed by the qubit transitions frequencies evaluation and the sweetspot identification.

The first request was accomplished by a two-tone spectroscopy of the qubit: an RF signal was sent through the feedline close to the resonance frequency of the readout resonator in the low-photon regime f_{low} , and another RF signal that sweeps in frequency was sent through the qubit drive line exciting the qubit. As shown in Fig. 45 the measured resonance frequency was $f_{q,res} = 6.159 \pm 10^{-3} \text{ GHz}$, which is consistent with the high band frequencies working regime provided by QuantWare (Fig. 21 in Sec. 3.1).

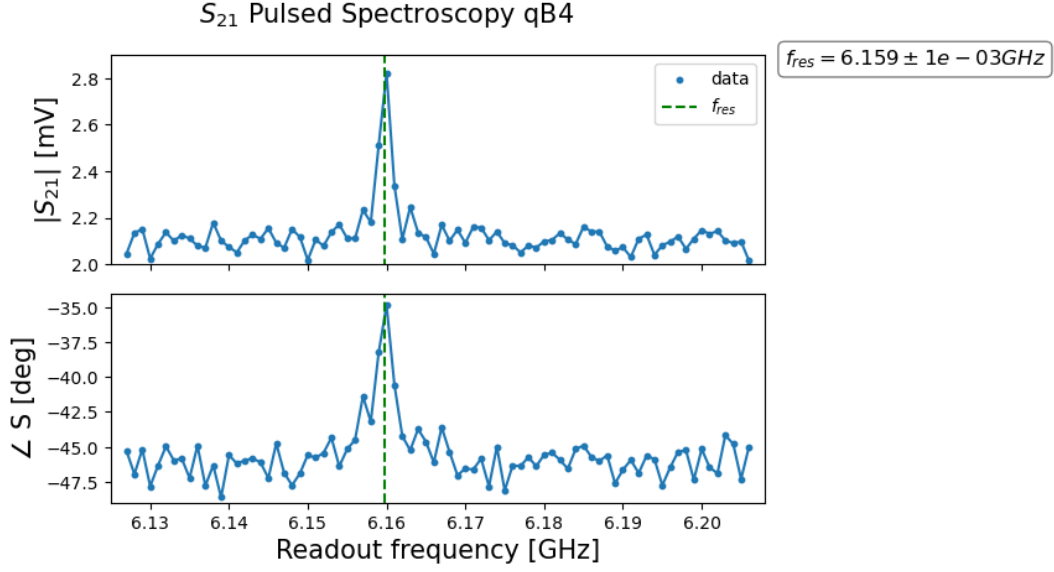


Figure 45: Qubit B4 resonator spectroscopy.

Subsequently, by performing the same experiment as a function of the power of the drive tone, it has been possible to identify energy peaks corresponding to the $|0\rangle \rightarrow |1\rangle$ transition and the $|0\rangle \rightarrow |2\rangle$ transition assisted by two photons. They have been observed at frequency values

$f_{01} = 6.168 \pm 10^{-3} \text{ GHz}$ and $f_{02}^* = 6.068 \pm 10^{-3} \text{ GHz}$, respectively. The f_{01} value is comparable with $f_{q,res}$. Note that f_{02}^* corresponds to the decay of only one of the 2 photons involved in the transition, then being actually the $\frac{f_{02}}{2}$ frequency value.

From these values, it is possible to estimate $f_{12} = (f_{02}^* * 2) - f_{01} = 5.968 \pm 3 * 10^{-3} \text{ GHz}$ and the anharmonicity $\alpha = -0.200 \pm 4 * 10^{-3} \text{ GHz} = -200 \pm 4 \text{ MHz}$, which is comparable to standard anharmonicity values in transmons [7]. Furthermore, since for the transmon qubit $\alpha \simeq -E_C$, we had a first estimation of the Charge energy $E_C^{(1)} = 200 \pm 4 \text{ MHz}$.

Then, in order to identify the qubit sweetspot, another two-tone spectroscopy was performed, but this time the second signal was sent to the qubit flux line for biasing it with a current, and resulting in a frequency modulation. As shown in Fig. 46b the measured qubit sweetspot occurs at a frequency $f_{q,sweetspot} = 6.1730 \pm 3.0 * 10^{-4} \text{ GHz}$, corresponding to a current $I_{q,sweetspot} = -8.51 \pm 4.0 * 10^{-2} \text{ mA}$, in agreement with the resonator current sweetspot $I_{q,sweetspot}$. Moreover, from this protocol it was possible to estimate E_C and E_J by using Eq. (12). Here, $E_C = 204 \pm 42 \text{ MHz}$ and $E_J = 24.0 \pm 0.3 \text{ GHz}$, considering a symmetric junction $d \simeq 0$ and $\frac{\Phi}{\Phi_0} \propto \frac{I - I_{q,sweetspot}}{I_{period}}$, where I_{period} is the frequency modulation period. Note that the charge energy E_C measured with this protocol is comparable with the previous $E_C^{(1)}$.

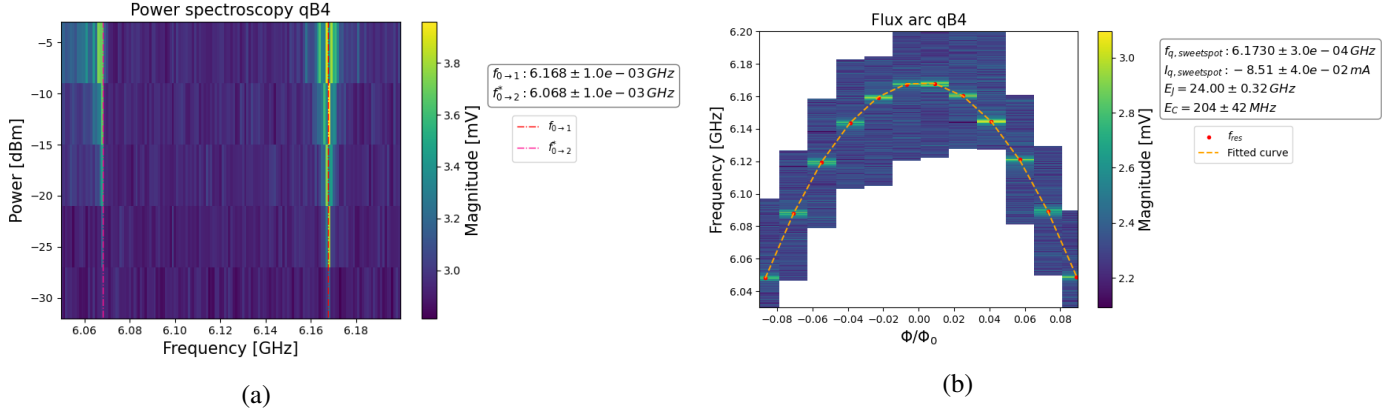


Figure 46: Qubit B4 spectroscopy: in (a) power spectroscopy, in (b) flux arc spectroscopy.

B4 control pulses calibration and optimization

At this point of the analysis, it was necessary to properly calibrate the drive pulses. As seen in Sec. 3.6, the first protocol to be performed is the Rabi oscillation experiment which provides a measure for the π -pulse. By changing the amplitude of the drive tone from $-1V$ to $1V$, the resulting plot features an oscillating trend (Fig. 47). Here, the half-period corresponds to the π - pulse = $0.532 \pm 0.002 V$ (Fig. 47).

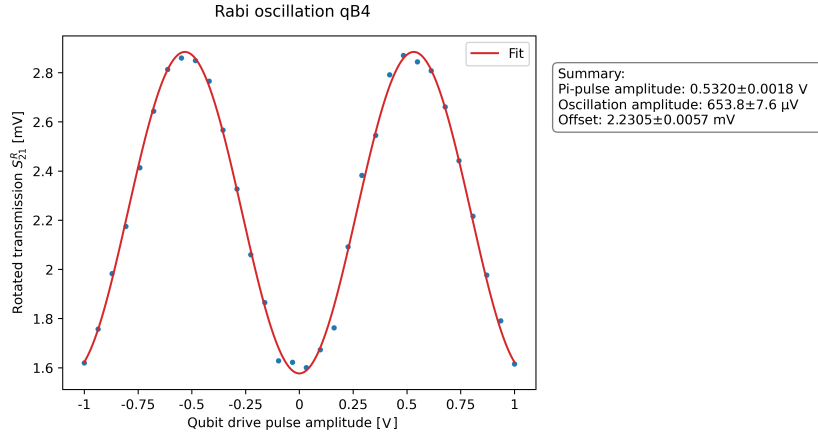


Figure 47: Rabi oscillation on qubit B4.

In order to offer a comparison between the control performances before and after the optimization procedures, a Randomized Benchmarking protocol was performed (Fig. 48b). For this preliminary measurement, it was chosen to set 5 seeds.

The result was an average gate fidelity of $F_{avg.gate}^{pre} = 0.9986 \pm 0.0004$.

Therefore, we started the optimization procedure by performing a first *AllXY* protocol in order to identify possible error syndromes (Sec. 3.7). As shown in Fig. 48a the central part of the plot featured a zig-zag pattern, pointing a possible detuning error.

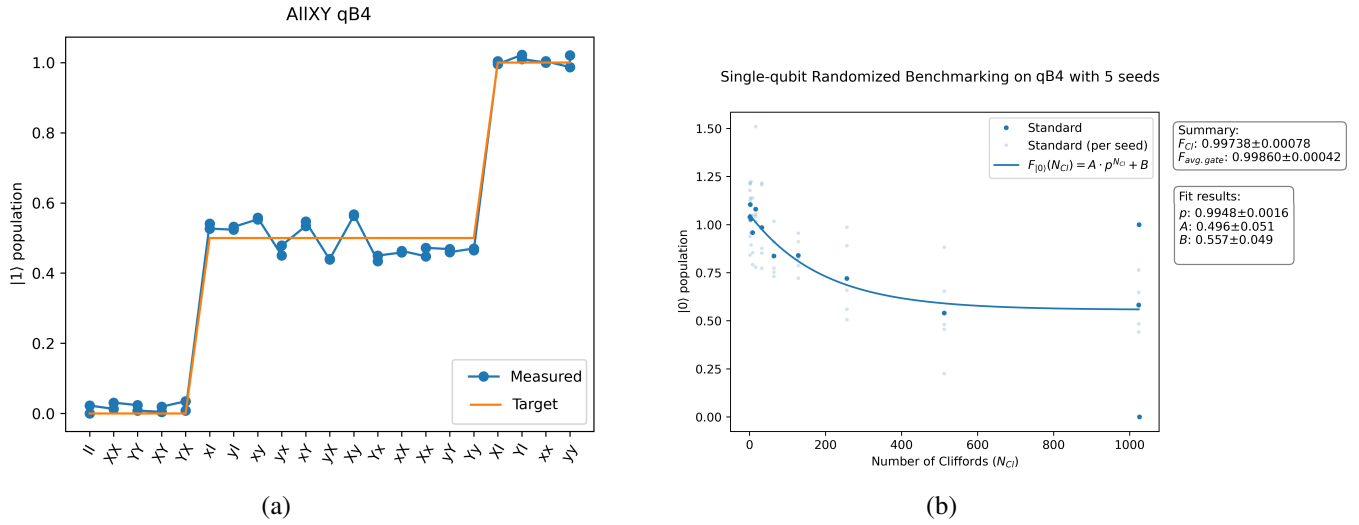


Figure 48: Starting point of the calibration and optimization: in (a) First trial *AllXY*; in (b) preliminary RB protocol with 5 seeds.

Therefore, we performed a Ramsey fringes protocol in order to find the optimal frequency of the drive tone. As described in Sec. 3.6, the Ramsey fringes protocol measures the response of the readout resonator coupled to the qubit as a function of qubit drive tone frequency and of the time delay between the two $\frac{\pi}{2}$ -pulses. As shown in Fig.49a, the optimal drive tone resonant frequency was found to be $f_{res} = 6.1603 \pm 2.0 \times 10^{-4} GHz$. This value for the qubit frequency is much more precise than the one estimated by the qubit spectroscopy experiment, because the Ramsey protocol is more sensitive to the drive-qubit frequency detuning. Therefore, it stands as our main reference for the experimental qubit frequency.

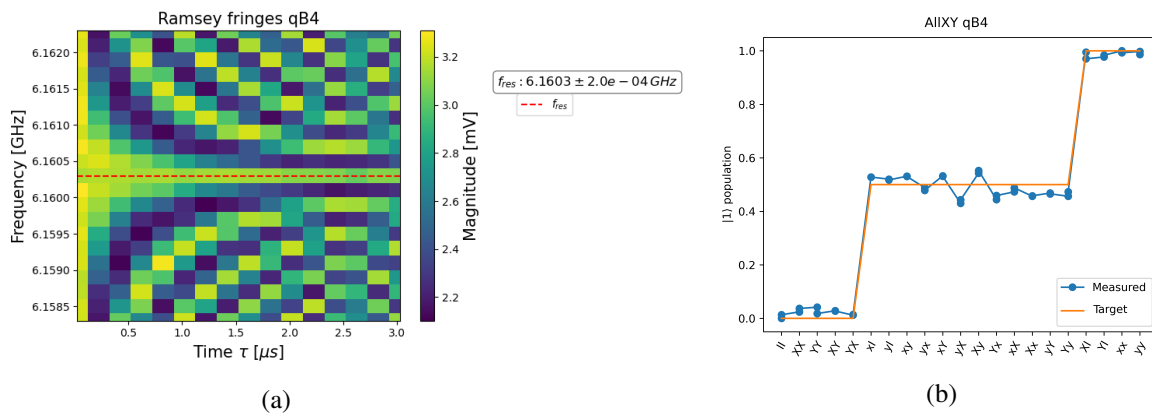


Figure 49: Ramsey fringes in (a) and *AllXY* protocol after frequency calibration through Ramsey interferometry in (b).

In the second *AllXY* trial (Fig. 49b) the pattern did not change, but rather the first and the last output operations in the central part of the plot featured opposite shifts, suggesting a possible error arising from a detuned *DRAG* parameter.

Then a Motzoi protocol was performed by taking $X_{\frac{\pi}{2}}Y_{\pi}$ and $Y_{\frac{\pi}{2}}X_{\pi}$ pulses which exhibit the opposite sign of error (Tab. 2) and finding the optimal *DRAG* coefficient at the crossing point of the resultant lines $\lambda = -0.058$ (Fig. 50a).

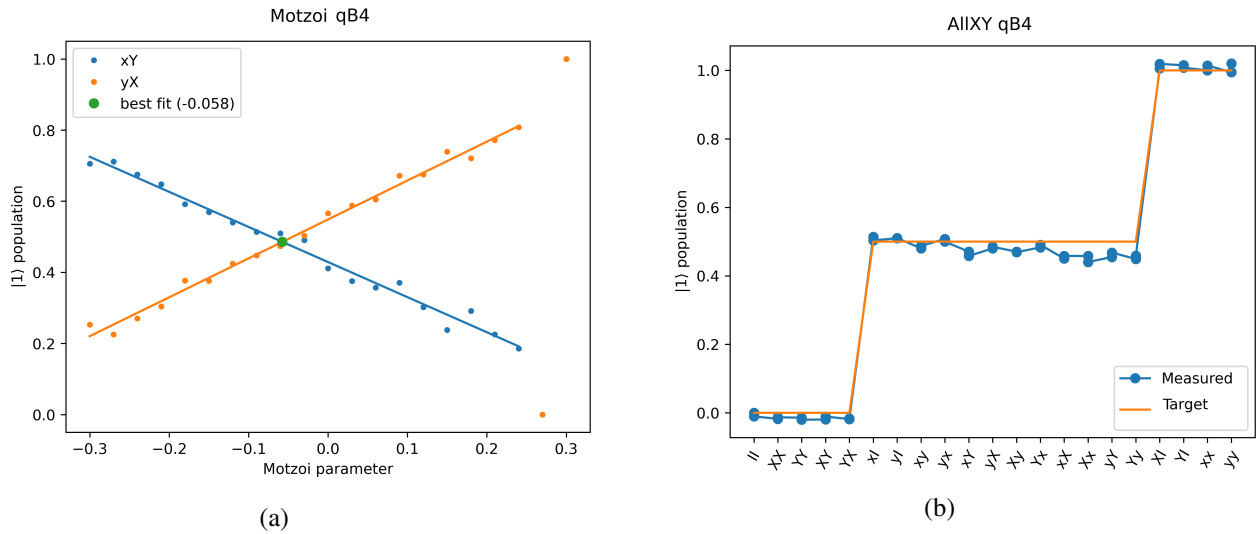


Figure 50: Motozi protocol in (a) and *AIIXY* protocol after Motzoi calibration in (b).

The subsequent *AIIXY* trial did not feature the zigzag pattern anymore, but a step pattern arose, suggesting a possible power syndrome (Fig. 50b).

Then a Flipping protocol was performed, which consists in preparing the qubit state on the equator, and then applying an increasing number of pairs of π -pulses. If the π -pulses causes an over- or undershoot, an oscillation pattern arise.

In the following we show the flipping protocol before (Fig. 51a) and after (Fig. 51b) applying the corrected pulse of $\pi = 0.523 V$. Finally, the last *AIIXY* trial, shown in Fig. 52, featured no remarkable syndrome, indicating we reached the optimal pulse calibration and that we have successfully corrected the control pulses.

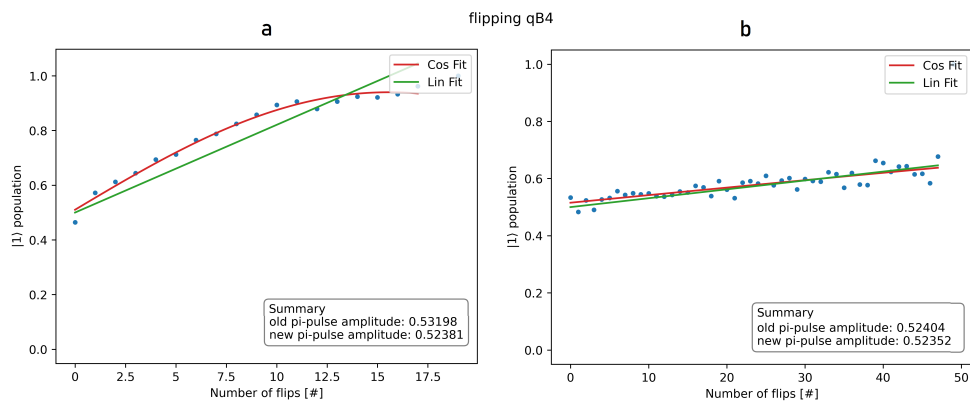


Figure 51: Flipping protocol: in a oscillation resulting from over- and undershot of π -pulse; in b no oscillation occurs after the pulse correction.

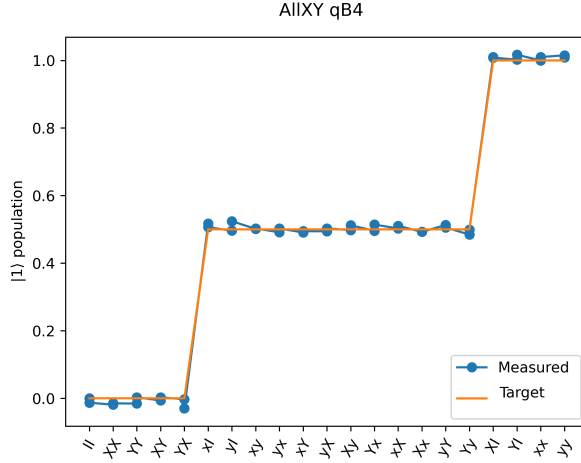


Figure 52: Fourth trial $AllXY$.

B4 Gate Fidelity

Since the qubit was completely characterized and the drive pulse was properly calibrated, all the requirements had been fulfilled in order to evaluate the qubit performance in terms of control quality. We performed the Randomized Benchmarking protocol, both with 5 seeds set for a comparative purpose (compare Fig. 53a with Fig. 48b), and with 200 seeds for a better evaluation (Fig. 53b). For the 5 seeds RB, we obtained an average gate fidelity $F_{avg.gate}^{post} = 0.9996 \pm 0.0002$, resulting higher than $F_{avg.gate}^{pre}$ as expected, since a proper calibration reduces the SPAM errors that affect the performances. For the 200 seeds RB we obtained $F_{avg.gate} = 0.99942 \pm 5.0 \times 10^{-5}$. These fidelity values are comparable to the state-of-the-art values [61], suggesting an efficient control optimization.

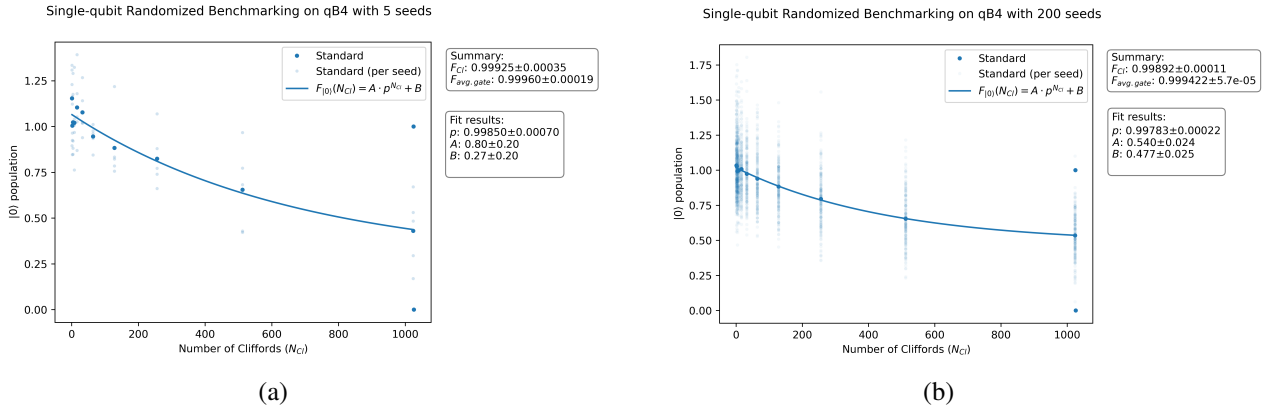


Figure 53: RB protocols after calibration and optimization in (a) RB protocol with 5 seeds; in (b) RB protocol with 200 seeds.

Coherence times

Lastly, we measured the coherence times of qB4 according to protocol described in Sec. 3.8. First we measured the relaxation time T_1 by preparing the qubit in its ground state, then exciting it by applying a π -pulse, and then leaving it to evolve spontaneously for a variable time τ before performing the measurement. The resultant exponential decay allows us to fit the characteristic time, which was found to be $T_1 = (25.3 \pm 0.9) \mu s$ (Fig. 54a). For a more accurate estimation, we performed several measurements in order to do a statistical analysis. As shown in Fig. 54b, the counts of T_1 have been collected in a count distribution with binning of 10.

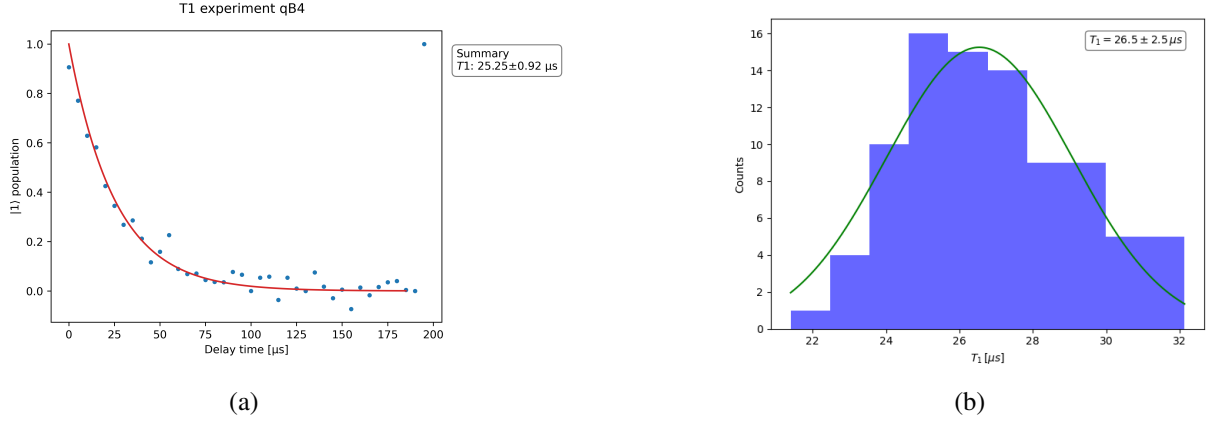


Figure 54: Qubit B4 relaxation time: in (a) T_1 measurement protocol; in (b) T_1 statistical analysis.

Moreover, according to Sec. 2.1, coherence times are affected by stochastic noise, therefore it is possible to estimate T_1 as the mean value of the normal distribution [7]. Here, the mean value is defined as $\mu = \frac{1}{N} \sum_{i=1}^N x_i$, where x_i are the N sampled data, while the error is given by the standard deviation, defined as $\sigma = \sqrt{\frac{1}{N} \sum_{i=1}^N (x_i - \mu)^2}$. The resulting relaxation time was $T_1 = (27 \pm 3) \mu s$.

Then, in order to measure T_2^* , a Ramsey Interferometry protocol was performed, in which the qubit is prepared on the equator by a $\frac{\pi}{2}$ -pulse, left to evolve spontaneously for a variable time τ , then followed by another $\frac{\pi}{2}$ -pulse before measuring its state. We decided to perform T_2^* measurement both for an off-resonant and an on-resonance qubit drive tone. In Fig. 55a it is shown the off-resonance case, in which we applied an artificial detuning of 150 kHz. As consequence of the off-resonant drive tone, an oscillation trend occurred, allowing for a damped oscillatory curve fitting (Sec. 3.6). The resultant time was $T_2^* = (7.3 \pm 0.5) \mu s$, with a fitted detuning between the drive signal frequency and the qubit resonance frequency of $\Delta = (306 \pm 2) kHz$. Conversely, in Fig. 55b it is shown the on-resonance case, after applying a correction to the detuning of 460 kHz and resulting only in the exponential decay. Here, $T_2^* = (7 \pm 3) \mu s$ and the fitted detuned was $\Delta = (14 \pm 3) kHz$. As with T_1 , a statistical analysis of T_2^* was performed too (Fig. 56). Here, the counts have been collected in a count distribution with binning of 12, and the normal distribution gave $T_2^* = (8.0 \pm 0.7) \mu s$.

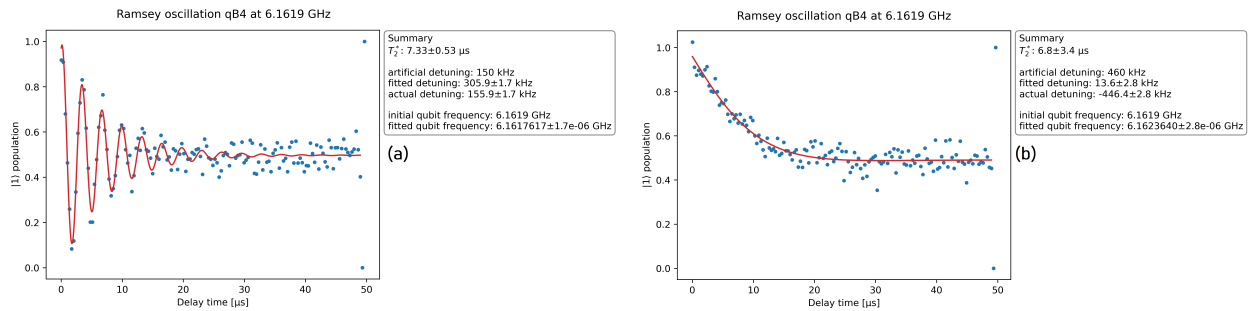


Figure 55: Qubit B4 Ramsey Interferometry: in (a) and (b) T_2^* off-resonance and on-resonance measurement protocols, respectively.

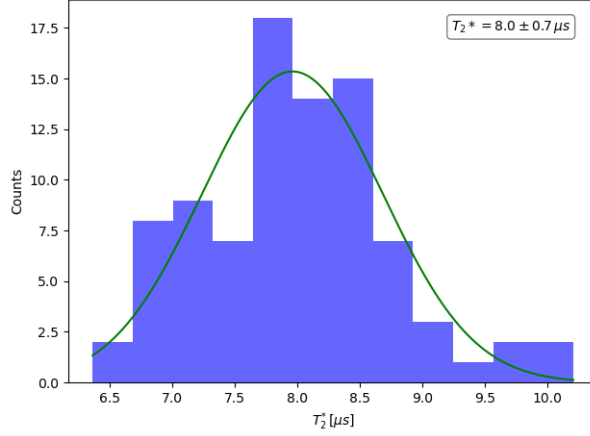


Figure 56: T_2^* statistical analysis.

Lastly, for a better estimation of T_2 , it was also performed the T_2 Echo protocol, in which a refocusing π -pulse is applied between the two $\frac{\pi}{2}$ -pulses mitigating the quasi-static, low frequencies fluctuations that cause inhomogeneous broadening during the Ramsey protocol (Sec. 3.8). As shown in Fig. 57a, the resulting time was $T_{2E} = (27.2 \pm 7.3) \mu s$. Again, for a better T_{2E} estimation, a statistical analysis was performed collecting counts in a binning of 12 (Fig. 57b), and resulting in $T_{2E} = (21.5 \pm 3.0) \mu s$, a larger value if compared with T_2^* , as expected. The coherence times we found for the qubit B4 are comparable with the state-of-art values [7].

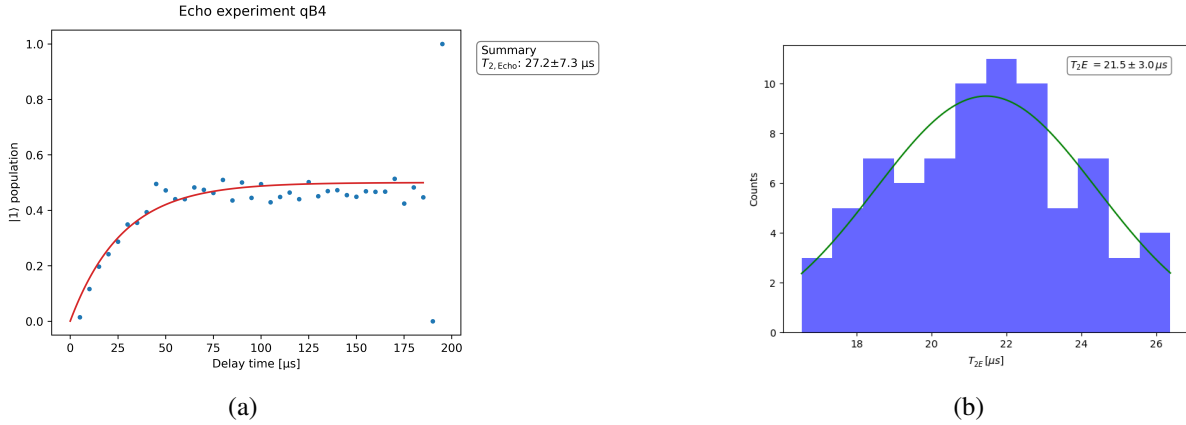


Figure 57: Qubit B4 Echo protocol: in (a) T_{2E} measurement protocol; in (b) T_{2E} statistical analysis.

Noise impact on coherence times and qubit frequency

As we reported in Sec. 2.1, there are several noise sources that affect the qubit coherence properties. For this reason we evaluated the noise impact on the qubit B4.

First we report the coherence times trend over a period of about two hours as a function of the Mixing Chamber temperature fluctuations. As illustrated in Sec. 3.2, the sample stage has approximately the same temperature of the MXC, allowing us to study the impact of thermal noise on the qubit.

As shown in the Fig. 58, the coherence times haven't been affected by temperature fluctuations, featuring no remarkable correlation between the measured data and the temperature rise and fall, at least in this time period and for this temperature range.

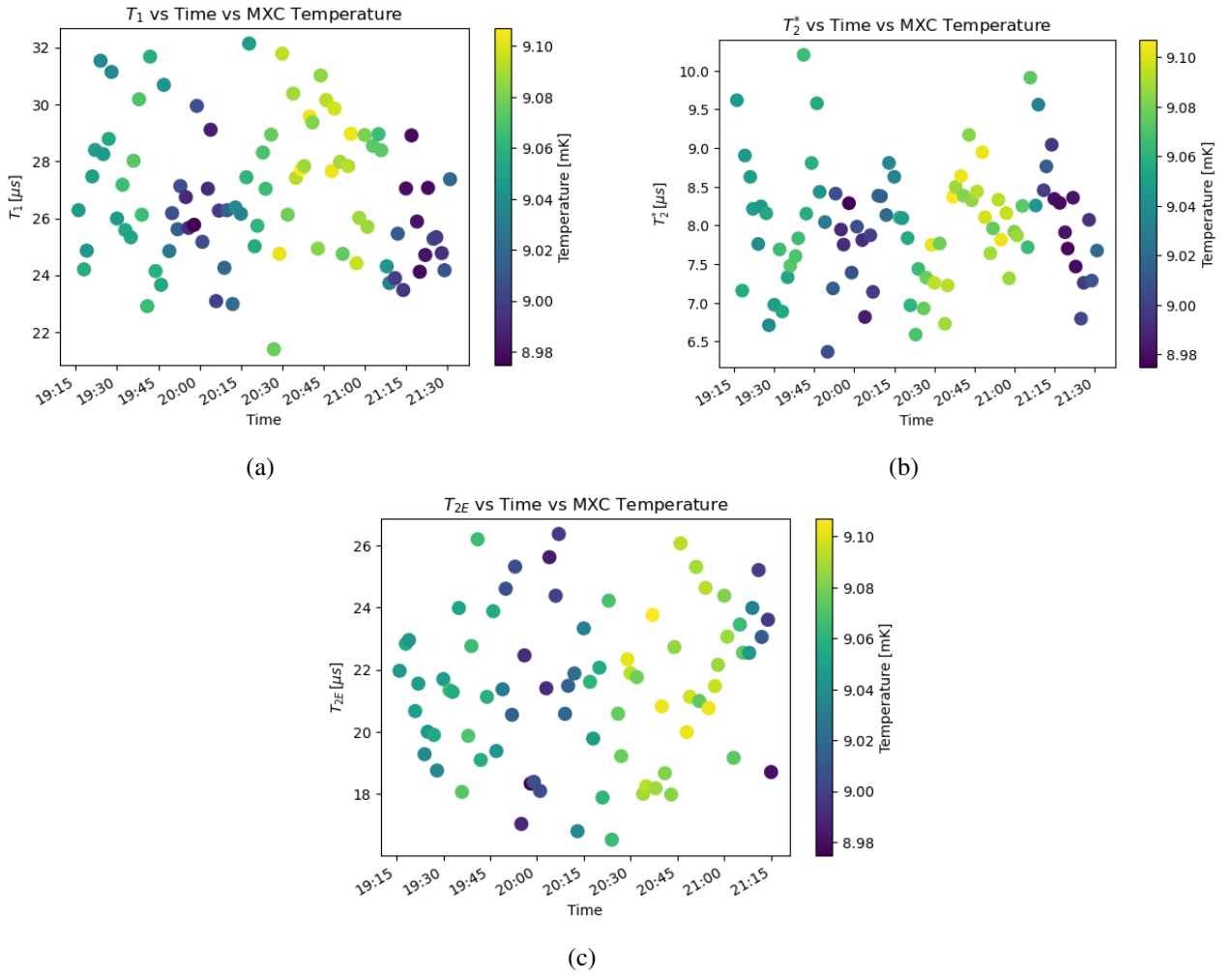


Figure 58: Qubit B4 coherence times as a function of Mixing Chamber temperature over a period of about 2 hours: T_1 in (a), T_2^* in (b) and T_{2E} in (c).

Further proof of the fact that thermal noise doesn't affect qubit properties, in this range of temperature and time, is the same analysis done for the qubit frequency. As shown in Fig. 59, the qubit frequency, calculated from the Ramsey oscillations fitting, exhibits an oscillation trend in the order of tens of kHz that doesn't depend on temperature fluctuations.

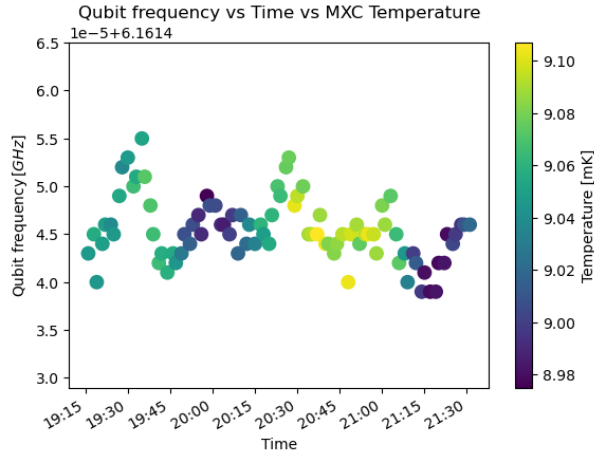


Figure 59: Qubit B4 resonance frequency as a function of Time period of around 2 hours and MXC temperature.

Another noise source that can influence coherence times of a transmon qubit is the flux noise due to the flux threading the SQUID's loop in the tuning operation (Sec. 1.4.1). Therefore, we measured the relaxation time T_1 and the dephasing time T_{2E} of qubit B4 as a function of flux by changing the bias current through the flux line (Fig. 60a and 60b).

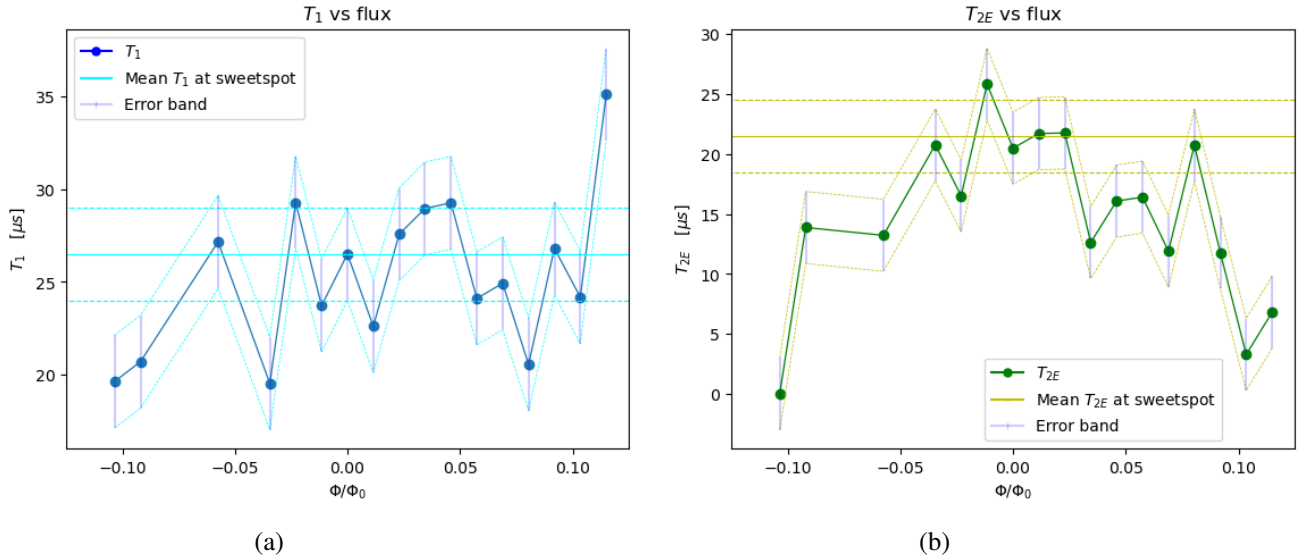


Figure 60: Qubit B4 coherence times as a function of normalized flux Φ/Φ_0 : in **(a)** T_1 sampled data in blue with their error bands and the mean T_1 value with his error band highlighted in cyan; in **(b)** T_{2E} sampled data in green with their error bands and the mean T_{2E} value with his error band highlighted in yellow.

As expected, the relaxation time T_1 was not strongly affected by the flux noise (Sec. 2.1.1). Conversely, the dephasing time was strongly affected by the flux noise, featuring the $1/f$ noise trend which is characteristic of the SQUID [62].

In order to give a better view of this characteristic trend, we plotted the T_φ values, obtained from T_1 and T_2 (Eq. (33)), as a function of normalized flux Φ/Φ_0 . We compared our data with a simulated trend by using the *scqubits* package on Python, which allows for qubit features simulations from its characteristic parameters [63]. As shown in Fig. 61, the experimental data spread following the simulated trend. The only exception is on the zero-point flux where the simulation features a divergence due to the identity $T_2 = 2T_1$ which actually never happen both for an instrumental limit issue and for the effect of other noise sources on coherence times [64].

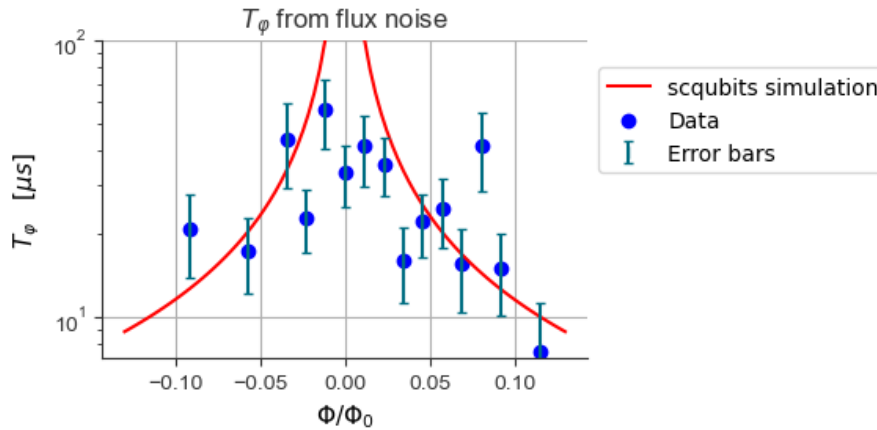


Figure 61: Pure dephasing time T_φ as a function of normalized flux Φ/Φ_0 : in blue the experimental data with their own error bars, in red the *scqubits* simulated trend.

4.2 Qubits parameters

In this section, we report the main parameters we obtained by performing the experimental procedures on most of Contralto-D QPU qubits, as previously shown for B4. At the time of measurement the drive and flux lines of feedline A were not connected, for these reasons we managed to perform only the preliminary spectroscopy measurements. One of the future goal will be the characterization of this feedline with the same protocols exploited for the other feedlines. Moreover qubits D1 and C5 were found to be not working, while the drive line of qubit B3 was shorted to the ground, thus no control operation could be performed.

	$f_{01} \pm 10^{-3}GHz$	$f_{readout} \pm 10^{-3}GHz$	$I_{sweetspot} \pm 10^{-1}mA$	$E_C \pm 10^{-1}MHz$	$E_J \pm 10^{-2}GHz$
A1	4.746	7.126	X	X	X
A2	5.464	7.402	X	X	X
A3	5.583	7.504	X	X	X
A4	4.948	7.654	X	X	X
A5	5.405	7.757	X	X	X
B1	4.731	7.132	6.2	195.5	15.52
B2	5.240	7.376	0.8	302.8	12.68
B4	6.169	7.579	-8.0	204.8	24.00
B5	5.459	7.619	-12.4	246.7	16.50
C1	4.550	7.080	8.2	244.0	12.69
C2	5.412	7.353	4.7	251.6	15.88
C3	5.422	7.478	0.7	294.0	13.16
C4	4.685	7.299	-7.9	379.0	8.44
D2	5.349	7.393	-5.0	372.0	11.00
D3	5.387	7.498	6.2	251.0	15.80
D4	6.189	7.718	9.2	247.3	20.98
D5	5.239	7.651	6.5	259.2	12.56

Table 3: Contralto-D QPU qubits and resonators parameters: in green low frequency band qubits, in blue mid frequency band qubits and in red high frequency band qubits.

In Tab.3, we collect all the qubit parameters measured until the time of writing. From a first analysis we can confirm that all qubits feature a resonance frequency f_{01} within the range requested to QuantWare for the QPU design (Tab. 1). Moreover, the resonators readout frequency $f_{readout}$ in each distinct feedline are sufficiently far apart so that it is possible to address to a qubit in a univocal way, allowing for a multiplexing readout in the future measurements. About the charge energies E_C , and so the anharmonicity of the transmons, all the values are comparable with the standard ones [7], and the predicted $200MHz$ value designed by the producer. Lastly, given the measured Josephson energies E_J , $\frac{E_J}{E_C}$ ratios for each qubit are comparable with those expected for the transmon working regime [7].

In the Tab.4 we report the qubit drive parameters for each measured qubit, namely the π_{pulse} amplitude and the pulse duration τ . The error on τ was established considering the QBLOX clock time grid of $4 ns$ on which operations are performed (Sec. 3.4).

	$\pi - pulse \pm 2 mV$	$\tau \pm 4 ns$
B1	858	176
B2	420	20
B4	521	20
B5	434	20
C1	383	20
C2	779	20
C3	670	20
C4	403	20
D2	464	20
D3	578	20
D4	527	20
D5	455	20

Table 4: Contralto-D QPU qubits drive parameters: in green low frequency band qubits, in blue mid frequency band qubits and in red high frequency band qubits.

All π -pulse values are in the range of hundreds of mV , as well as the pulse duration are all the same with the exception of B1 which features an unusual longer τ . The reason why the drive pulse for qB1 requires a longer time at same range of amplitudes could be a possible mismatch between the drive line and the transmon qubit that might be due to fabrication issues. The more plausible cause for the mismatch in the drive power required to excite qB1 can be related to a lower capacitive coupling between the qubit and its dedicated drive line. Another reason may be related to the fact that a fraction of power sent through the drive line actually flows towards the ground of the chip instead of being fully coupled to the qubit. In our processor the ground uniformity is guaranteed through the integration of air bridges around each line of the device [65]. Due to the intrinsic fragile nature of the air bridges, they may collapse in some points, thus shorting to ground the line on which they are suspended. Room-temperature measurements of the resistance to ground of drive lines should always identify an open circuit. However, for qB1 we have indeed measured a finite resistance, who may be possibly caused by a sub-optimal air bridges configuration, that has shortened to ground this drive line specifically.

4.3 Coherence times

In the following we report a summary of the coherence times of the Contralto-D qubits. For all the qubits, these have been obtained at the flux sweetspot, setting the neighboring qubits to their minimum in frequency, i.e. at the half flux quantum $\frac{\Phi_0}{2}$. This is done in order to work in the single-qubit regime, and avoid intentional interaction between the investigated qubits.

Moreover, we report the same data in the form of a color mapping, taking into account the geometry and the connectivity of the device (Fig. 62).

From Fig. 62a we found that the qubit on QPU feature comparable relaxation times T_1 , with the highest value for qB1 and lowest values for qD5 and qC1. From Fig. 62b we found that Ramsey times T_2^* are almost the same throughout the QPU, featuring highest coherence time along feedline D, and with the lowest value on qC3. Lastly, from Fig. 62c we found that Echo times values T_{2E} seem higher along feedline D, while lower along feedline C.

Further analysis of feedline A will be necessary in order to have a complete knowledge of the QPU.

	$T_1 \mu s$	$\Delta T_1 \mu s$	$T_2^* \mu s$	$\Delta T_2^* \mu s$	$T_{2E} \mu s$	$\Delta T_{2E} \mu s$
B1	33.0	6.0	17.0	5.0	16.0	7.0
B2	25.0	4.0	20.9	1.7	21.0	5.0
B4	26.5	2.5	8.0	0.7	21.5	3.0
B5	25.0	4.0	18.0	3.0	19.0	5.0
C1	15.0	2.0	17.0	5.0	16.0	4.0
C2	26.0	2.0	17.0	5.0	24.0	5.0
C3	25.0	3.0	2.7	0.6	15.0	2.0
C4	23.0	4.0	15.0	5.3	15.0	4.0
D2	29.0	2.0	27.0	1.0	27.0	4.0
D3	23.0	2.0	28.0	2.0	36.0	6.0
D4	26.0	1.0	21.0	1.0	27.3*	3.8*
D5	17.0	3.0	17.0	14.0	22.0	5.0

Table 5: Contralto-D QPU qubits coherence times: in green low frequency band qubits, in blue mid frequency band qubits and in red high frequency band qubits. For each qubit we have performed statistical analysis. *For qD4 the number of T_{2E} values wasn't enough for a statistical analysis, then we show the mean value and the maximum error.

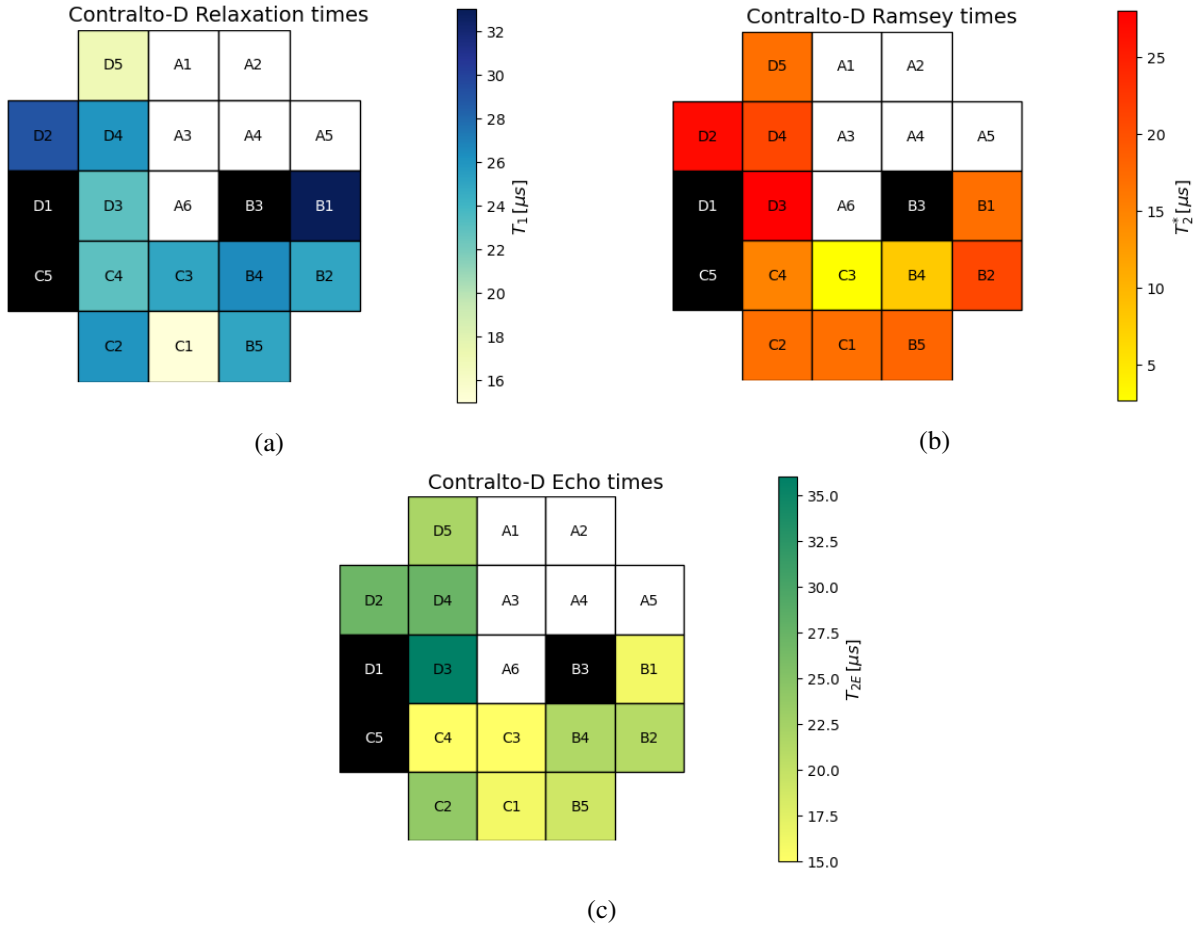


Figure 62: Contralto-D coherence times diagrams: relaxation times T_1 in (a); dephasing times T_2^* and T_{2E} in (b) and (c), respectively. Feedline A wasn't connected at the time of measurements. In black the inoperative qubits.

4.4 Single-qubit Gate Fidelity

In the following we report the single-qubit average gate fidelity measured with the Randomized Benchmarking with 200 seeds.

From a first analysis of values in the table shown in Fig. 63, we can confirm that all the analyzed qubits feature an high average gate fidelity around 0.999 and 0.998 comparable with the today's standard values [61], only exception for qubits C2 and B1: the lower fidelity of B1 may be due the unusual longer pulse duration τ (Tab. 4), which reduce the average gate fidelity (Eq. 49).

	$F_{avg.gate}$	$\Delta F_{avg.gate}$
B1	0.9958	$1*10^{-4}$
B2	0.99915	$6*10^{-5}$
B4	0.99939	$3*10^{-5}$
B5	0.99907	$7*10^{-5}$
C1	0.99871	$6*10^{-5}$
C2	0.9969	$2*10^{-4}$
C3	0.9989	$1*10^{-4}$
C4	0.9988	$1*10^{-4}$
D2	0.9988	$1*10^{-4}$
D3	0.99836	$9*10^{-5}$
D4	X	X
D5	0.99871	$5*10^{-5}$

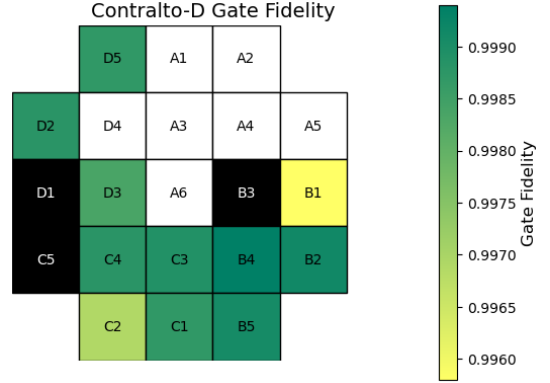


Figure 63: Contralto-D QPU single-qubit average gate fidelity: in green low frequency band qubits, in blue mid frequency band qubits and in red high frequency band qubits (on the left). QPU Gate Fidelity diagram on the right.

Then, in order to compare the experimental results with the coherence-fidelity dependence model (Eq. (49)), we performed a rough estimation of the Clifford gates duration τ_{Cl} from the gate fidelity F_{Cl} , obtained from the experimental survival probability p , and coherence times T_1 and T_2 , by combining Eq. (49) with Eq. (58) in the single qubit approximation $N = 1$:

$$\tau_{Cl} = (1 - F_{Cl}) \frac{3}{\Gamma_1 + \Gamma_\varphi}. \quad (60)$$

From these values the theoretical Clifford gate fidelity was estimated and compared with the experimental values (Tab. 6).

Therefore, the discrepancy between the experimental and theoretical values $\Delta = \frac{|F_{Cl} - F_{model}|}{\sigma_{Cl}}$, with $\sigma_{Cl} = 0.00112$ the error on F_{Cl} , was plotted as function of coherence times T_1 and T_2 in order to check the compatibility within 3σ (Fig. 64). All the fidelity values fall under the compatibility threshold with the exception of qB1 and qC2 fidelity. The strong assumption of isolated qubits might be a plausible reason for the incompatibility of those fidelity values with the model: as a matter of the fact, the survival probabilities of qB1 and qC2, as well as their Clifford fidelity values, are lower than the other ones suggesting a less effective gate implementation that could be related to depolarizing channels (Eq. (48)). Moreover, the reduction of gate fidelity is proportional to the time required to perform the gates τ_{Cl} , then the compatibility threshold could lay between 200 ns (qD3 falls within the 3σ region) and 300 ns. Lastly, more precise comparison with the model must be done with fidelity values from statistical analysis.

	p	F_{Cl}	$\tau_{Cl} ns$	F_{model}
B1	0.98433	0.99217	300	0.999992
B2	0.99682	0.99841	70	0.999998
B4	0.99783	0.99892	50	0.999998
B5	0.99462	0.99731	100	0.999997
C1	0.99515	0.99758	80	0.999997
C2	0.98884	0.99421	300	0.999994
C3	0.99571	0.99786	70	0.999997
C4	0.99545	0.99773	80	0.999997
D2	0.99540	0.99770	100	0.999997
D3	0.99384	0.99692	200	0.999996
D4	X	X	X	X
D5	0.99517	0.99758	100	0.999997

Table 6: Contralto-D QPU single-qubit RB survival probability p , Clifford gate Fidelity F_{Cl} , Clifford gate duration estimation τ_{Cl} and theoretical Clifford gate Fidelity F_{model} . In green low frequency band qubits, in blue mid frequency band qubits and in red high frequency band qubits.

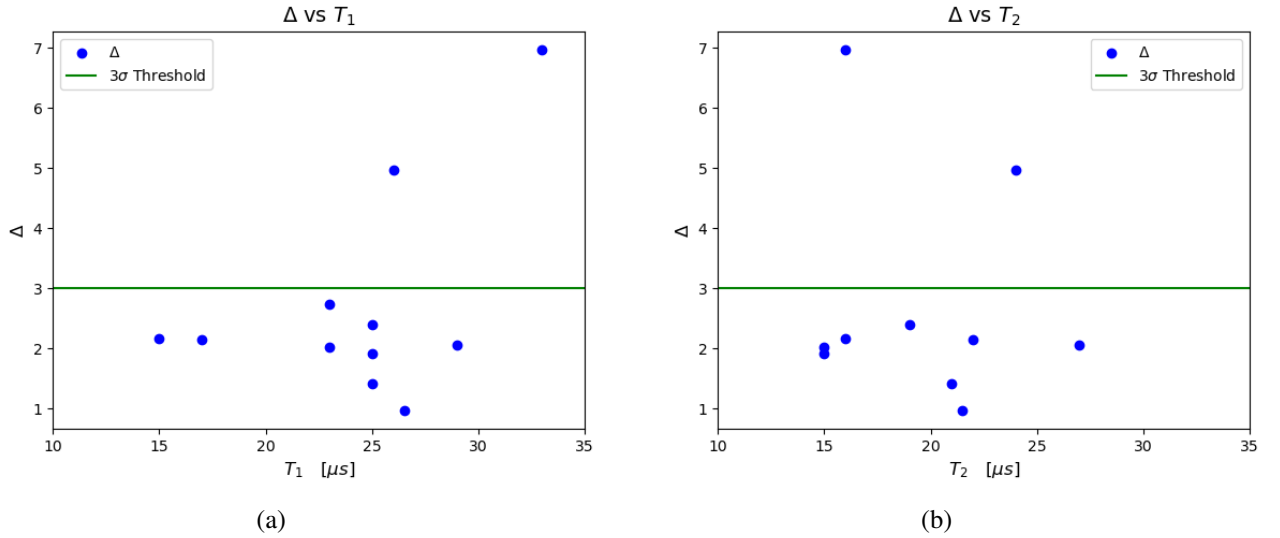


Figure 64: Clifford gate fidelity discrepancies Δ between experimental and theoretical values, as a function of relaxation time T_1 in (a) and dephasing time T_2 in (b). In green the 3σ threshold under which the values are compatible.

4.5 Towards two-qubits characterization

The implementation of two-qubit gates, like the *i*SWAP gate (Sec. 2.2.2), requires a coherent energy exchange between coupled qubits while they are on resonance. Therefore, it is demanded the characterization of their interaction in terms of coupling strength J (Eq. (28)), which can be estimated through avoided level crossing measurements (Sec. 1.5).

As example purposes, in Fig. 65 we show the avoided level crossing measurements between the qubit B4 and the neighbors qubits B2, B5 and C3 (qubit B3 was inoperative). Since the qubit B4 operates at higher frequency band, for each possible pair, the measurement consisted in performing a spectroscopy of the lower frequency band qubit, set in its sweetspot, while tuning B4 through external flux until it resonates with each coupled qubit. When the two qubits are on resonance, a gap in the energy spectrum opens, from which it's possible to estimate the coupling strength J .

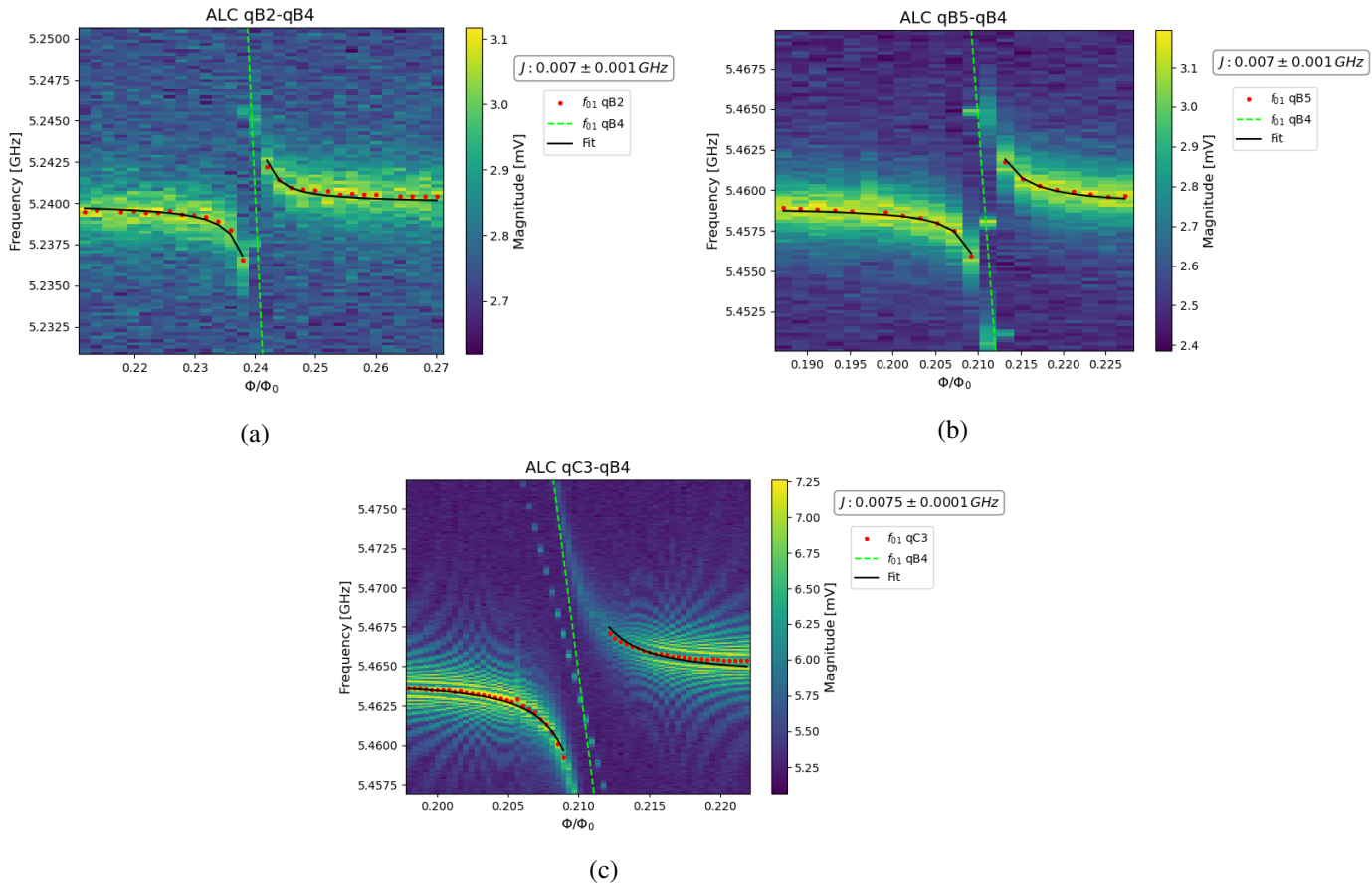


Figure 65: Avoided level crossing of qubit B4 with its neighbors qubits B2 in **(a)**, B5 in **(b)** and C3 in **(c)**. From each power spectroscopy the mean value of the coupling strength J was estimated by fitting it from the higher and lower branches.

According to Ref. [66], it is possible to fit J from the upper and lower branch of the avoided crossing by the function:

$$f\left(\omega; \omega_{ge}^{(2)}, J\right) = \left(\left(\omega + \omega_{ge}^{(2)} \right) \pm \sqrt{\left(\omega + \omega_{ge}^{(2)} \right)^2 + 4J^2} \right) / 2, \quad (61)$$

where the ω is the tuned frequency of the higher frequency qubit (Eq. (12)) and $\omega_{ge}^{(2)}$ is the fixed qubit resonance frequency. Once fitted the J values from the two branches, the mean value and the maximum error was estimated (Tab. 7).

	$J \text{ GHz}$	$\Delta J \text{ GHz}$	$t \text{ ns}$
B2-B4	0.007	0.001	224.399
B5-B4	0.007	0.001	224.399
C3-B4	0.0075	0.0001	224.3995

Table 7: Coupling strength J fitted from the avoided level crossing of qubit B4 with qubits B2, B5 and C3.

From the coupling strength J it is possible to estimate the time required to perform an i SWAP gate, i.e. the time after which an excitation is coherently swapped from one qubit to another when on resonance (Eq. (37)). These times resulted to be much smaller than the qubits coherence times, meaning that they are suitable for performing fast two-qubit operations (Tab. 7). The same analysis will be performed on all QPU qubits in the next future.

Conclusions

In this thesis a 25-transmon qubit quantum processor has been characterized. Being the first prototype of its kind in Italy, and among the very few ones in Europe, and in view of its deployment for running quantum algorithms, a detailed comparative analysis of the circuital parameters and performances has been carried out. The focus of this thesis work was the coherence and control fidelity evaluation, key parameters for the computing performances. For each transmon qubit the following parameters have been characterized:

- The readout resonator frequency, its “low photon” shift and flux modulation. The readout resonator resonance frequencies resulted to be comparable with the builder’s values, spreading in the range of $(7.080 \div 7.759) \pm 10^{-3} GHz$. Therefore, since they are univocally addressable through a single multi-tone signal, they result suitable for the future implementation of multiplexing readout for algorithms outputs. The characterization of “low photon” regime, i.e. when the photons population inside the readout resonator is poor, allowed us to find the proper condition to perform non-demolition measurements of the qubit quantum state. Finally, the study of flux modulation aimed at finding the current sweetspot value at which the qubit is less sensitive to the flux noise and then able to provide better performances.
- The qubit resonance frequency, its transition frequency from the ground to the excited state, its flux arc modulation, from which the sweetspot was identified, and the Josephson and Charge energies. The qubit resonance frequencies resulted to be comparable with the builder’s values, falling in the three different frequency bands ($4 \div 5$, $5 \div 6$ and $6 \div 7 GHz$) with values in the range $(4.746 \div 6.189) \pm 10^{-3} GHz$. This configuration allows to implement two-qubits gates by tuning the frequency of higher bands qubits until they are on resonance with the lower bands ones. Moreover, this particular geometry allows for future surface code detection and correction implementation in order to mitigate errors arising from decoherence phenomena. The Josephson energies resulted to be in the range $(8.44 \div 24.00) \pm 10^{-2} GHz$, then comparable with the state-of-art values around tens of GHz . Also the Charge energies, with values in the range $(195.5 \div 302.0) \pm 10^{-1} MHz$ resulted to be comparable with the state-of-art values around hundreds of MHz . Therefore, the E_J/E_C ratios were all compatible with the transmon working regime, then making the qubits less sensitive to the charge noise.

After the spectroscopy measurements, the qubit control drive calibration and optimization have been performed. For each qubit the calibrated parameters have been:

- The π -pulse amplitude and duration measured through the Rabi protocol. The first one resulted to be in the range of $(383 \div 858) \pm 2 mV$, while the last one resulted to be $(20 \pm 4) ns$ for every qubit, with the exception of qB1 of $(176 \pm 4) ns$. This higher value might be caused by a bad coupling between the drive line and the qubit. The π -pulse estimation, i.e. the pulse required to lead the $|0\rangle \rightarrow |1\rangle$ energy transition or, in general, a 180° rotation of the unitary qubit state vector within the Bloch sphere, allows for an accurate control of the qubit system.
- The drive signal frequency through Ramsey Interferometry protocol which allows for adjusting its detuning with the qubit resonance frequency. This calibration is necessary in order to avoid the qubit state vector to precess uncontrollably when an operation is performed.

Finally, for each qubit the $AIXY$ protocol has been performed in order to eventually identify syndrome errors related to detuning, power or DRAG parameters, respectively corrected through Ramsey Fringes Interferometry, Flipping and Motzoi protocols.

This optimization process not only highlighted the efficiency of our experimental setup, which results to be capable of interfacing properly with tens of qubits, as quantum systems, and of performing gates, but most importantly allowed us to:

- i) understand the best optimization procedure to follow before any quantum algorithms implementation, being it effective in improving the single-qubit gate fidelities towards state-of-the-art values;
- ii) highlight fundamental relations between the hardware performances and the coherence.

In fact, once the qubits parameters have been identified, and the control parameters optimized, the performance evaluations have been carried out by measuring the qubits coherence times and gate fidelity. For each qubit T_1 , T_2^* and T_{2E} times have been measured several times in order to make a statistical analysis. The T_1 times fall between $(15.0 \pm 2.0) \mu s$ and $(33.0 \pm 6.0) \mu s$, T_2^* between $(8.0 \pm 0.7) \mu s$ and $(28.0 \pm 2.0) \mu s$, while T_{2E} between $(15.0 \pm 2.0) \mu s$ and $(36 \pm 6.0) \mu s$: these values are comparable with the state-of-art values, being also a benchmark of the efficiency of our experimental setup in mitigating environmental noise.

Therefore, the impact noise sources on coherence times, T_1 and T_2 , and qubit frequency have been analyzed: as a result of around 2 hours measurements, we noticed that the coherence times have not been affected by thermal noise in that range of temperature, as well as the qubit frequency features only stochastic oscillations in the order of kHz . This is a result of primary importance for allowing researchers to run their algorithms in the long term, since it demonstrates that the performances of the device are not limited by our experimental setup, and that we have efficiently thermalized the most important cryogenic components and the processor. Therefore, this work has been fundamental to assess the capabilities of the infrastructure, which promises performances comparable to those of state-of-the-art superconducting quantum computing centers worldwide. Secondly, we have checked the negligible impact of flux noise on the relaxation time T_1 , contrary to the visible dependence of the transverse relaxation time T_2 which featured a typical $1/f$ trend. These results provide knowledge on the dissipative channels influence on qubits performance and on the reliability of our experimental setup of mitigate their effects while operating at the flux sweetspot, where negligible $1/f$ noise has been detected.

About the QPU control performances, for each qubit the average gate fidelity has been measured through Randomized Benchmarking protocol, resulting in values around $0.998 \div 0.999$ (with the exception of qB1 and qC2 with values around 0.996), reaching the state-of-art values and the so called “golden three nines”. Moreover, the coherence-fidelity dependence model has been validated. This indicates that average single-qubit gate fidelities are only limited by the coherence times of the device, and the optimization procedures that we have chosen to exploit have been successful. Checking on error syndromes occurring in the QPU by performing the *AIIXY* protocol to understand which parameters need to be adjusted, has limited the number of optimization iterations down to few cycles, while at the same time providing excellent results and knowledge about complex correction techniques. Therefore, this work has provided fundamental feedback on the selection of the most important protocols to run in the hardware calibration phase before the quantum algorithms implementation. We are currently working in integrating them into automatized tune-up routines, which promises to lower the required calibration time even further.

As final step, a preview of two-qubit characterization was given by analyzing the coupling strength of qubit B4 with its neighbors qubits, key parameter for efficient two-qubit gates, related to the energy gap that opens when two qubits are on resonance.

Downstream of this comparative analysis, we can affirm that the QPU coherence and control fidelity performances make it suitable for performing algorithms in the near future. Then this work can be seen as the first step in the perspective of an open source quantum computing node for the academic community, where researchers can develop and implement their own algorithms. Further analysis on feedline A qubits, two-qubits characterization and readout fidelity evaluations will be done shortly to get a comprehensive knowledge on QPU potentialities for an efficient deployment.

Appendix A

Derivation of Fidelity-Coherence dependence

The average gate fidelity \bar{F} of a trace-preserving quantum operator \mathcal{E} acting on an N -qubit system, is defined as [36]:

$$\bar{F} = \int d\psi \langle \psi | U_g^\dagger \mathcal{E}(\psi) U_g | \psi \rangle, \quad (62)$$

where the integral is over all pure initial states and U_g is the unitary operator corresponding to the ideal gate operation. Note that $\bar{F} = 1$ only if \mathcal{E} implements U_g perfectly, while lower values indicate a noisy or imperfect implementation. The gate operation in Eq. (62) can be generated by a time-dependent Hamiltonian $H(t)$ applied for a time τ , such that $U_g = U(0, \tau)$, where we have introduced the time-evolution operator for the ideal gate operation $U(t_1, t_2) = \mathcal{T} \exp \left[-\frac{i}{\hbar} \int_{t_1}^{t_2} H(t) dt \right]$ and \mathcal{T} is the time-ordering operator. The effect of decoherence can be described using the standard Lindblad superoperator

$$\mathcal{D}[\hat{L}]\rho = \hat{L}\rho\hat{L}^\dagger - \frac{1}{2}\{\hat{L}^\dagger\hat{L}, \rho\}, \quad (63)$$

acting on the system density matrix ρ . The time evolution of the system with N_L dissipative processes is then given by the master equation

$$\dot{\rho}(t) = -\frac{i}{\hbar} [H(T), \rho(t)] + \sum_{k=1}^{N_L} \Gamma_k \mathcal{D}[\hat{L}_k] \rho(t), \quad (64)$$

where each process has its corresponding rate Γ_k and Lindblad jump operator \hat{L}_k . Jump operators describe the dissipative part of dynamics and their shape define the environmental action on the system. Since in experimental state-of-art incoherent errors are on percent level or less, it is possible to expand the solution of the master equation in the small parameter $\Gamma_k \tau \ll 1$ for a pure initial state $|\psi\rangle$. The unperturbed solution is $\rho_\psi^{(0)} = |\psi(t)\rangle\langle\psi(t)|$, where $|\psi(t)\rangle = U(0, t)|\psi\rangle$. The first-order correction due to the k_{th} decoherence process is

$$\rho_{\psi,k}^{(1)}(t) = \Gamma_k \int_0^t dt' U(t', t) \left[\mathcal{D}[\hat{L}_k] \rho_\psi^{(0)}(t') \right] U^\dagger(t', t), \quad (65)$$

which corresponds to applying the dissipator $\mathcal{D}[\hat{L}_k]$ to the ideal pure state $|\psi(t')\rangle$ once, at any time $t' < t$. Then, considering this correction, it is possible to show that each dissipative process contributes independently to first order, bringing to an average gate fidelity

$$\bar{F} = 1 + \sum_{k=1}^{N_L} \int d\psi \langle \psi | U^\dagger(0, \tau) \rho_{\psi,k}^{(1)}(\tau) U(0, \tau) | \psi \rangle. \quad (66)$$

Inserting Eq. (65) and performing the integral we find

$$\int d\psi \left[\langle \psi | \hat{L} | \psi \rangle \langle \psi | \hat{L}^\dagger | \psi \rangle - \langle \psi | \hat{L}^\dagger \hat{L} | \psi \rangle \right] \equiv \delta F(\hat{L}). \quad (67)$$

Since the integrand appears to be time-independent, the Eq. (66) leads to

$$\bar{F} = 1 + \tau \sum_{k=1}^{N_L} \Gamma_k \delta F(\hat{L}_k) + \mathcal{O}(\tau^2 \Gamma_k^2). \quad (68)$$

The reduction of gate fidelity is thus independent of which unitary gate U_g is performed and proportional to the time τ it takes to perform the gate. Each dissipative channel contributes independently, proportional to its rate Γ_k and the factor $\delta F(\hat{L}_k)$.

Individual qubit energy relaxation acts one qubit with jump operator $\hat{L} = \sigma_-$ and rate Γ_1 , while the additional pure dephasing with jump operator $\hat{L} = \sigma_z$ and rate Γ_φ . For uncorrelated dissipation, the N -qubit jump operators are tensor products with identity matrices acting on all other qubits, then

$$\delta F_N(\sigma_z^1 \otimes \sigma_0^2 \dots \sigma_0^N) = -\frac{d}{2(d+1)}, \quad (69)$$

with $d = 2^N$. Finally, remembering that different dissipators add independently to the gate fidelity, the first-order reduction due to uncorrelated energy relaxation and pure dephasing on all N qubits is:

$$\bar{F}_N^{uc} = 1 - \frac{d}{2(d+1)} \tau \sum_{k=1}^N (\Gamma_1^k + \Gamma_\varphi^k). \quad (70)$$

Appendix B

Derivation of fitting function in Randomized Benchmarking protocol

The Randomized Benchmarking protocol consists of the following steps [67], repeated for several values of m number of gate operation in a sequence:

Step 1 Generate a sequence of $m + 1$ quantum operations with the first m chosen uniformly at random from the Clifford group and the final operation chosen so that the net sequence is the Identity operation. The $m + 1$ th correction gate will also be a Clifford element. In practice each operation \mathcal{C}_{i_j} will have some associated error and the entire sequence can be modeled by

$\mathcal{S}_{i_m} = \bigcirc_{j=1}^{m+1} (\Lambda_{i_j,j} \circ \mathcal{C}_{i_j})$ where i_m is the m -tuple $(i_1; \dots; i_m)$ and i_{m+1} is uniquely determined by i_m . Here, $\Lambda_{i_j,j}$ represents the error associated with the operation \mathcal{C}_{i_j} , which doesn't depend on the time-step j . In this noise model, the only assumption is that correlations in the noise are negligible on time scales longer than the time of the operation \mathcal{C}_{i_j} (so that $\Lambda_{i_j,j}$ does not depend on earlier operations). This assumption becomes very well motivated as n increase.

Step 2 For each sequence measure the survival probability $Tr [E_\psi \mathcal{S}_{i_m}(\rho_\psi)]$. Here ρ_ψ is the the initial state taking into account preparation errors and E_ψ is the POVM [69] element that takes into account measurement errors. In the ideal noise-free case $\rho_\psi = E_\psi = |\psi\rangle\langle\psi|$.

Step 3 Average over random realizations of the sequence to find the averaged sequence fidelity

$$F_{seq}(m, \psi) = Tr [E_\psi \mathcal{S}_m(\rho_\psi)], \quad (71)$$

where \mathcal{S}_m is the average sequence operation

$$\mathcal{S}_m = \frac{1}{|\{i_m\}|} \sum_{i_m}^{|i_m\}|} \mathcal{S}_{i_m}. \quad (72)$$

Step 4 Fit the results for averaged sequence fidelity to the model

$$F_{seq}^{(1)}(m, \psi) = A_1 p^m + B_1 + C_1(m-1)(q-p^2)p^{m-2}. \quad (73)$$

Here A_1 , B_1 and C_1 absorb SPAM errors as well as the error on the final gate. Moreover the term $(q-p^2)$ is related to the presence of *weak gate dependence*. The average error rate $r = 1 - p - \frac{1-p}{d}$ with $d = 2^n$.

In the particular case of gate-independent errors, the fitting results simplify to

$$F_{seq}^{(0)}(m, \psi) = A_0 p^m + B_0, \quad (74)$$

where A_0 and B_0 still absorb SPAM errors as well as the error on the final gate.

In order to define the parameters r and p , let's start to define

$$\Lambda \equiv \frac{1}{|\{(i_j, j)\}|} \sum_{(i_j, j)}^{|(i_j, j)\}|} \Lambda_{i_j, j} \quad (75)$$

as the average error for the set of error operators $\{\Lambda_{i_j, j}\}$. The standard experimental figure of merit for a noise model Λ is the average gate fidelity $F_{avg} = \int d\psi \langle \psi | \Lambda (|\psi\rangle\langle\psi|) | \psi \rangle$, which is the survival probability averaged over all pure input state (as in Sec. 2.3). Then the average error rate is defined as $r \equiv 1 - F_{avg}$.

To define p , Λ is "twirled" over the Clifford group [15], giving

$$\frac{1}{K} \sum_l C_l^\dagger \circ \Lambda \circ C_l = \Lambda_{dep}, \quad (76)$$

where $\Lambda_{dep}(\rho) = p\rho + (1-p)\frac{\mathbb{I}}{d}$ is the unique depolarizing channel with the same average fidelity as Λ , and K is the number of operation in the Clifford set.

Hence, $F_{avg} = p + \frac{(1-p)}{d}$ which relates the fidelity decay parameter p to the average error rate r as given above:

$$F_{avg} = 1 - \frac{d-1}{d}(1-p). \quad (77)$$

Lastly, further derivation leads to:

$$A_0 = Tr \left[E_\psi \Lambda \left(\rho_\psi - \frac{\mathbb{I}}{d} \right) \right], \quad (78)$$

$$B_0 = Tr \left[E_\psi \Lambda \left(\frac{\mathbb{I}}{d} \right) \right]. \quad (79)$$

References

- [1] A. Montanaro. *Quantum Information* (2016) 2, 15023.
- [2] F. Arute et al.. Quantum supremacy using a programmable superconducting processor. *Nature* volume 574, pages505–510 (2019).
- [3] J. Preskill. Quantum Computing in the NISQ era and beyond. *Quantum* 2, 79 (2018).
- [4] Mst Shapna Akter. *Quantum Cryptography for Enhanced Network Security: A Comprehensive Survey of Research, Developments, and Future Directions* (2023).
- [5] Benedikt Fauseweh. Quantum many-body simulations on digital quantum computers: State-of-the-art and future challenges. *Nature Communications* 15, 2123 (2024).
- [6] Dmitry A Fedorov et al. “Ab initio molecular dynamics on quantum computers”. In: *The Journal of Chemical Physics* 154.16 (2021).
- [7] P. Krantz ; M. Kjaergaard ORCID; F. Yan; T. P. Orlando; S. Gustavsson; W. D. Oliver. *A Quantum Engineer’s Guide to Superconducting Qubits. Applied Physics, Reviews* 6, 021318 (2019).
- [8] F. Tafuri. *Fundamentals and frontiers of the Josephson effect*, volume 286. Springer Nature (2019).
- [9] Jens Koch et al. Charge-insensitive qubit design derived from the Cooper pair box. *Physical Review A* 76.4 (2007).
- [10] Elizabeth Gibney. Google publishes landmark quantum supremacy claim. *Nature*, Vol 574, 2019.
- [11] Davide Castelvecchi. IBM releases first-ever 1,000-qubit quantum chip. *Nature*, Vol 624, (2023).
- [12] Jeremu HSU. Rigetti Launches Full-Stack Quantum Computing Service and Quantum IC Fab. *IEEE Spectrum*, (2017).
- [13] J. Preskill. Quantum Computing in the NISQ era and Beyond. *Quantum*. arXiv:1801.00862v3. (2018).
- [14] R. Barends et al.. Logic gates at the surface code threshold: Superconducting qubits poised for fault-tolerant quantum computing. *Nature*, Volume 508, Issue 7497, pp. 500-503 (2014).
- [15] A. M. Meier. *Randomized Benchmarking of Clifford Operators*. Ph.D. Thesis. (2018).
- [16] J.M. Chow et al. “Randomized benchmarking and process tomography for gate errors in a solid-state qubit”. In: *Physical review letters* 102.9 (2009).
- [17] Y. Nakamura, Y. A. Pashkin, and J. S. Tsai, Coherent control of macroscopic quantum states in a single-Cooper-pair box. *Nature (London)* 398, 786 (1999).
- [18] A. Somoroff, Q. Ficheux, R. A. Mencia, H. Xiong, R. V. Kuzmin, V. E. Manucharyan. Millisecond coherence in a superconducting qubit. (2021). arXiv:2103.08578.
- [19] N. T. Bronn et al. Fast, high-fidelity readout of multiple qubits. *J. Phys.: Conf. Ser.* 834 012003. (2017).
- [20] D. P. Di Vincenzo. *The Physical Implementation of Quantum Computation*. (2008).
- [21] R. Hott, R. Kleiner, T. Wolf, G. Zwicknagl. Review on Superconducting Materials. arXiv:1306.0429 [cond-mat.supr-con]. 2016.
- [22] M. Tinkham. *Introduction to Superconductivity*. (Second Edition), McGraw-Hill (1996).

- [23] J. Bardeen, L. N. Cooper, J. R. Schrieffer. Microscopic Theory of Superconductivity. (1951)
- [24] J. Bardeen, L. N. Cooper, J. R. Schrieffer. Microscopic Theory of Superconductivity. Physical Review, Volume 108, Number 5, (1957).
- [25] K.K. Likharev, Dynamics of Josephson Junctions and Circuits (Gordon and Breach, New York, 1986).
- [26] M. H. Devoret, J. M. Martinis, A. Wallraff. Superconducting Qubits: A Short Review. (2008).
- [27] A. Barone, G. Paterno. Physics and applications of the Josephson effect. Vol. 1. Wiley Online Library (1982).
- [28] A. Blais, A. L. Grimsmo, S. M. Girvin, A. Walraff. Circuit Quantum Electrodynamics. (2020).
- [29] J. Majer, J. M. Chow, J. M. Gambetta, J. Koch, B. R. Johnson, J. A. Schreier, L. Frunzio, D. I. Schuster, A. A. Houck, A. Wallraff, A. Blais, M. H. Devoret, S. M. Girvin, R. J. Schoelkopf. Coupling superconducting qubits via a cavity bus. Nature, vol 449. (2007)
- [30] S. Filipp et al. Multi-mode mediated exchange coupling in cavity QED. (2010).
- [31] E. M. Purcell, H. C. Torrey, R. V. Pound. Resonance Absorption by Nuclear Magnetic Moments in a Solid. Letters to the editor. (1945).
- [32] G. Catelani, R. J. Schoelkopf, M. H. Devoret, L. I. Glazman. Relaxation and frequency shifts induced by quasiparticles in superconducting qubits. Physical Review B. (2011).
- [33] C. Hughes, J. Isaacson, A. Perry, R. F. Sun, J. Turner. Quantum Computing for the Quantum Curious (2021).
- [34] J. Kelly et al. Optimal quantum control using randomized benchmarking. Phys. Rev. Lett. 112, 240504. (2014).
- [35] K. Boone. Concepts and methods for benchmarking quantum computers. Ph.D. Thesis. (2021).
- [36] T. Abad, J. Fernandez-Pendas, A. F. Kockum, G. Johansson. Universal fidelity reduction of quantum operations from weak dissipation. Phys. Rev. Lett. 129, 150504 (2022).
- [37] J. Gambetta, W. A. Braff, A. Wallraff, S. M. Girvin, R. J. Schoelkopf. Protocols for optimal readout of qubits using a continuous quantum nondemolition measurement. Phys. Rev. A 76, 012325 (2007).
- [38] J. Gambetta, A. Blais, M. Boissonneault, A. A. Houck, D. I. Schuster, S. M. Girvin. Quantum trajectory approach to circuit QED: Quantum jumps and the Zeno effect. Phys. Rev. A 77, 012112 (2008).
- [39] T. E. Walter. Rapid, High Fidelity, Single-Shot Readout. Master Thesis. (2014).
- [40] QuantWare website: <https://www.quantware.eu>
- [41] A. G. Fowler, M. Mariantoni, J. M. Martinis, A. N. Cleland. Surface codes: Towards practical large-scale quantum computation. Physical Review A 86, 032324. (2012).
- [42] H. London, G. R. Clarke. Osmotic Pressure of He^3 in Liquid He^4 , with Proposals for a Refrigerator to Work below $1K$. Physical Review, Volume 128, Number 5, (1962).
- [43] User Manual. XLD System. Bluefors. (2024).
- [44] M. Esposito, A. Ranadive, L. Planat, N. Rocha. Appl. Phys. Lett. 119, 120501 (2021).

- [45] S. Krinner, S. Storz, P. Kurpiers, P. Magnard, J. Heinsoo, R. Keller, J. Lütolf, C. Eichler, A. Wallraff. Engineering cryogenic setups for 100-qubit scale superconducting circuit systems. 2018.
- [46] QBLOX website: https://qblox-qblox-instruments.readthedocs-hosted.com/en/main/getting_started/index.html
- [47] QBLOX website: <https://qblox-qblox-instruments.readthedocs-hosted.com/en/main/cluster/index.html>
- [48] Quantify website: <https://quantify-os.org>
- [49] OrangeQS website: <https://orangeqs.com/products/quantum-diagnostics-libraries>
- [50] S. Ashhab et al. Rabi oscillations in a qubit coupled to a quantum two-level system. *New J. Phys.* 8 103. (2006).
- [51] H. G. Ahmad. *Physics of the Josephson Effect in Junctions with Ferromagnetic Barriers towards Quantum Circuits and RF Applications* (2021).
- [52] Mahdi Naghiloo. “Introduction to experimental quantum measurement with superconducting qubits”. In: arXiv preprint arXiv:1904.09291 (2019).
- [53] H. G. Ahmad et al. Investigating the Individual Performances of Coupled Superconducting Transmon Qubits. *Condens. Matter* 2023, 8, 29. (2023).
- [54] A. Antony et al. Miniaturizing transmon qubits using van der Waals materials. *Nano letters* 21.23, pp. 10122–10126 (2021).
- [55] F. Motzoi, F. K. Wilhelm. Improving frequency selection of driven pulses using derivative-based transition suppression. *Phys. Rev. A* 88, 062318 (2013).
- [56] Z. Chen et al. Measuring and Suppressing Quantum State Leakage in a Superconducting Qubit. *Phys. Rev. Lett.* 116, 020501 (2016).
- [57] M. D. Reed. *Entanglement and Quantum Error Correction with Superconducting Qubits.* (2013).
- [58] S. Bravyi and A. Kitaev. Universal quantum computation with ideal clifford gates and noisy ancillas. *Phys. Rev. A* 71, 022316 (2005).
- [59] J. M. Chow, L. DiCarlo, J. M. Gambetta, F. Motzoi, L. Frunzio, S. M. Girvin, R. J. Schoelkopf. Optimized driving of superconducting artificial atoms for improved single-qubit gates. *Phys. Rev. A* 82, 040305 (2010).
- [60] F. Motzoi, J. M. Gambetta, P. Rebentrost, F. K. Wilhelm. Simple pulses for elimination of leakage in weakly nonlinear qubits. *Phys. Rev. Lett.* 103, 110501 (2009).
- [61] R. Barends, J. Kelly et al. Superconducting quantum circuits at the surface code threshold for fault tolerance. *Nature* 508, 500–503. (2014).
- [62] R. H. Koch et al. Flicker ($1/f$) Noise in Tunnel Junction DC Squids. *Journal of Low Temperature Physics*, Vol 51, Nos. 1/2. (1983).
- [63] P. Groszkowski, J. Koch. Scqubits: a Python package for superconducting qubits. *Quantum* 5, 583. (2021).
- [64] M. Mergenthaler et al. Effects of surface treatments on flux tunable transmon qubits. *npj Quantum Information* volume 7, Article number: 157. (2021).

- [65] N. Janzen, M. Kononenko, S. Ren, A. Lupascu. Aluminum air bridges for superconducting quantum devices realized using a single step electron-beam lithography process. arXiv:2206.09489v2 [quant-ph]. (2022).
- [66] S. Filipp, M. Goppl, J.M. Fink, M. Baur, R. Bianchetti, L. Steffen, A. Wallraff. Multimode mediated qubit-qubit coupling and dark-state symmetries in circuit quantum electrodynamics. *Physical Review* 83,063827. (2011).
- [67] E. Magesan, J. M. Gambetta, J. Emerson. Scalable and Robust Randomized Benchmarking of Quantum Processes. *Phys. Rev. Lett.* 106.180504. (2011).
- [68] S. Asaad, C. Dickel, N. K. Langford, S. Poletto, A. Bruno, M. A. Rol, D. Deurloo, L. DiCarlo. Independent, extensible control of same-frequency superconducting qubits by selective broadcasting. *npj Quantum Information* 2, 16029. (2016).
- [69] R. Yuan. A Brief Introduction to POVM Measurement in Quantum Communications.